POLITECNICO
MILANO 1863

SCUOLA DI INGEGNERIA INDUSTRIALE
E DELL'INFORMAZIONE

Towards the modelling of abrasive slurry jet processes through a synergistic numerical-experimental approach

Tesi di Laurea Magistrale in
Mathematical Engineering - Ingegneria Matematica

Author: **Leonardo Ricchitelli**

Student ID: 952277
Advisor: Prof. Gianandrea Vittorio Messa
Academic Year: 2021-22

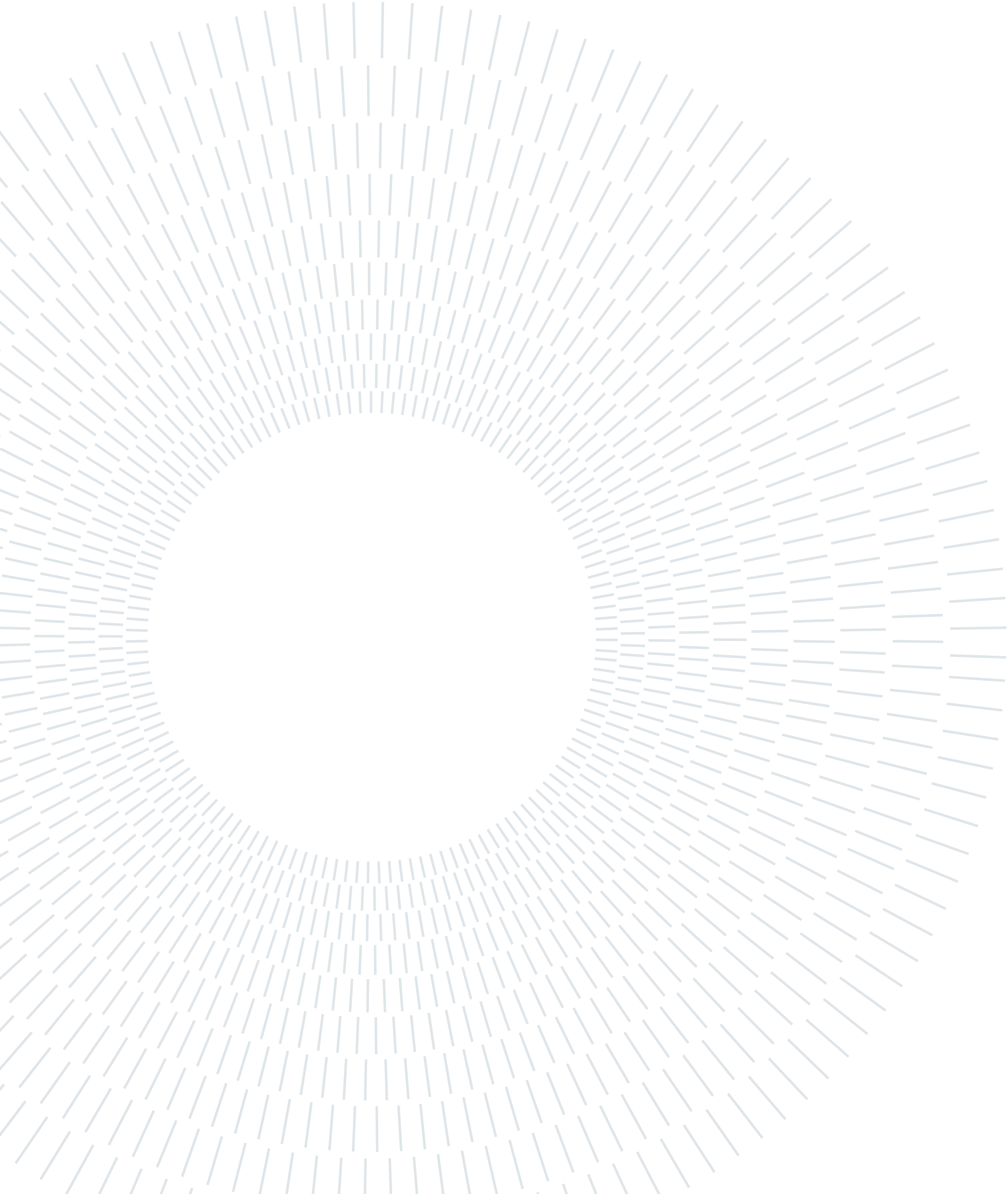

Abstract

Abrasive Slurry Jet Machining (ASJM) is a manufacturing technique which exploits the erosive action of a particle-laden water jet to cut materials. ASJM allows to overcome the drawbacks of traditional cutting methods, representing a less expensive, faster alternative, with lower forces involved and very limited tool heating and wear issues.

The computer simulation has great potential for the optimization of ASJM processes, as it avoids the need for complex equipment and reduces the waste of time and material. However, an engineering-effective simulation tool requires disposing of methods to predict erosive wear with sufficient accuracy and acceptable computational burden. Many empirical and phenomenological mathematical relations have been proposed by researchers to model erosion, but their predictive capacity is generally poor, owing to the high number of difficult-to-decide coefficients and the lack of information about their limits of validity. Additionally, they are mainly intended for dry particle-laden flows, which is not the case of ASJM. The present thesis focuses on an innovative, numerical-experimental method for the development of erosion models applicable to slurry jets. The method, initially proposed by researchers from the University of Tulsa and further investigated by the supervisor of this thesis and his collaborators, allows calibrating an erosion model by fitting a selected mathematical model to the measured erosion profile, using information on the fluid dynamic characteristics of the slurry flow obtained through a numerical simulation. In this work, the calibration procedure was firstly tested by repeating a previous application case. Afterwards, improvements to the methodology were proposed, which allowed for a better characterization of the effect of the particle impact velocity. The improved methodology was successfully applied to two different test cases, revealing a better predictive capacity outside the calibration range compared to the previous formulation. It is worth noting that, for the second test case, data obtained from an ASJM apparatus were considered, which confirmed the potential of the findings for this specific manufacturing process.

Keywords: ASJM, solid particle erosion, erosion model, Computational Fluid Dynamics, particle-laden flows.

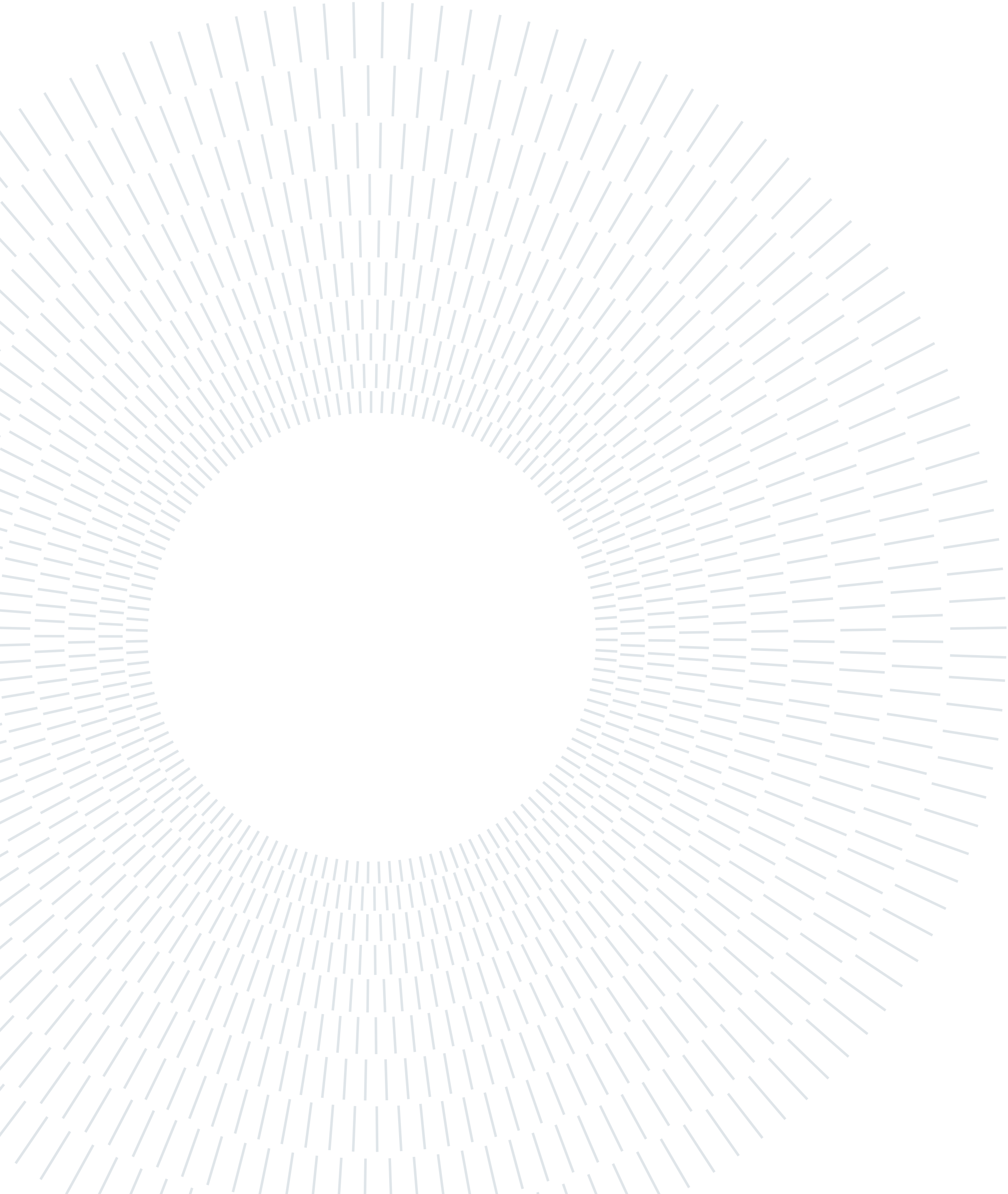

Abstract in lingua italiana

La lavorazione con getti a slurry abrasivo (ASJM) è una tecnica molto utilizzata nell'industria manifatturiera, che utilizza la capacità erosiva di flussi liquidi con particelle solide per tagliare i materiali lavorati. Questo metodo offre un'alternativa più economica e rapida alle tecniche tradizionali, quali tornitura, fresatura e foratura, riducendo le forze scambiate e il surriscaldamento degli strumenti. La simulazione numerica ricompre un ruolo rilevante nell'ottimizzazione dell'ASJM, in quanto permette di evitare di condurre esperimenti in laboratorio, che richiedono tempo ed elevati costi. Una simulazione efficace necessita di accurati modelli predittivi per il fenomeno dell'erosione. Molti modelli empirici e fenomenologici sono stati proposti da vari studiosi, la cui capacità predittiva è spesso limitata, data la presenza di coefficienti difficili da stimare e la poca chiarezza sui loro intervalli di applicabilità. Inoltre, tali modelli sono solitamente sviluppati per getti di particelle solide ad aria, quindi non per il caso dell'ASJM.

Lo studio qui presentato discute un innovativo metodo numerico-sperimentale per la calibrazione di un modello di erosione per ASJM. Tale metodo, inizialmente formulato da ricercatori dell'Univeristà di Tulsa, in Oklahoma, è stato poi approfondito dal relatore di questa tesi e da suoi collaboratori e permette di ottimizzare i coefficienti di un modello di erosione combinando dati sperimentali sui profili di erosione con le caratteristiche del flusso e della dinamica delle particelle solide, ottenute da una simulazione numerica.

In questo lavoro viene presentata l'applicazione di questo metodo a due casi test. Il primo è la riproduzione di uno studio precedentemente condotto, che ha permesso di calibrare un modello di erosione e valutarne l'accuratezza. Successivamente, vengono descritte alcune modifiche alla formulazione originale del metodo, mirate a migliorarne le prestazioni, in termini di capacità predittiva, con risultati molto positivi. In seconda analisi, viene studiato un profilo di erosione ottenuto da un test ASJM ad alta pressione. I buoni risultati ottenuti confermano che la procedura possa essere applicata a varie condizioni operative e scale geometriche.

Parole chiave: ASJM, erosione da impatto, modelli di erosione, Fluidodinamica Computazionale, flussi liquido-solidi.

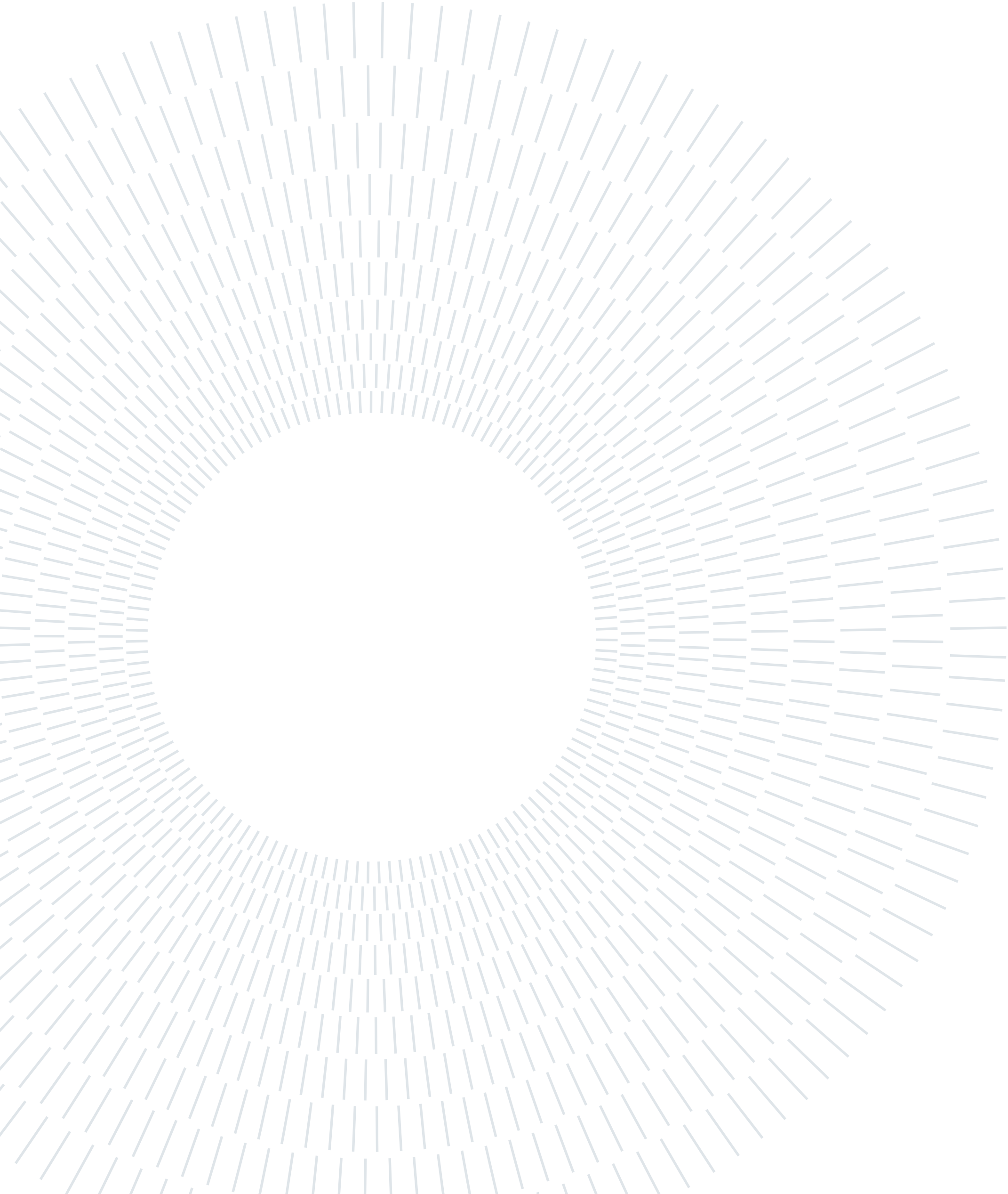

Contents

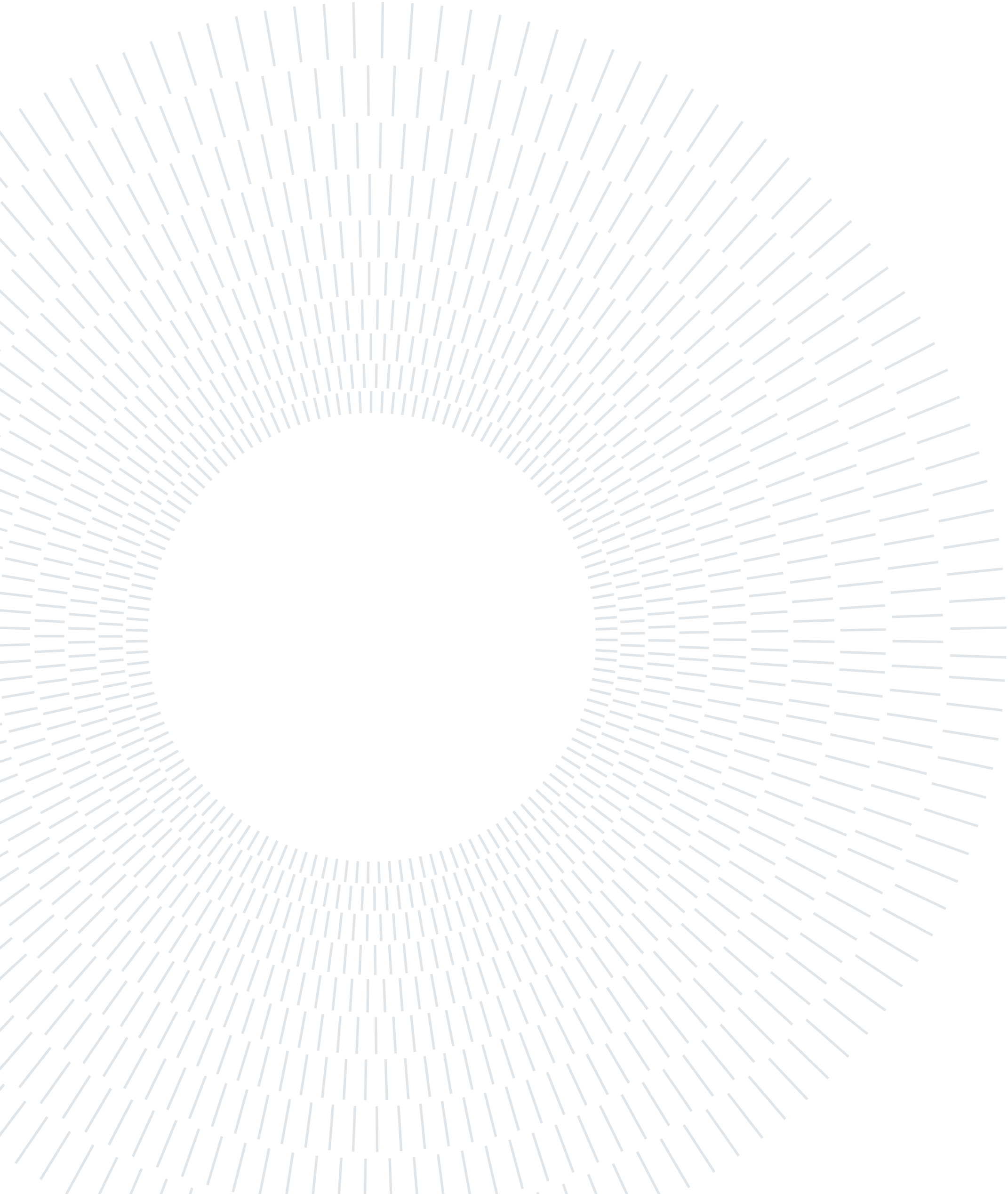

1 | Introduction

In this initial chapter, an overview of the Abrasive Slurry Jet Machining (ASJM) process is given. The present work revolves around this widely used engineering technique, focusing on one of the its main challenges, namely how to accurately model it numerically, which, as it will be explained, also requires disposing of high-quality experimental data.
Section 1.1 is aimed at illustrating the basic principles and functioning of ASJM in various industrial contexts, while Section 1.2 is an introduction to particle-laden flows. Then, in Section 1.3, the available approaches to the characterization of the solid particle erosion processes at the basis of the ASJM are listed, highlighting their strengths and weaknesses. Section 1.4 is dedicated to discussing the potential of Computational Fluid Dynamics (CFD) for a better understanding of the ASJM process, as a necessary step for its improvement and optimization. An overview of the numerical-experimental approach analysed and improved in this thesis is given in Section 2.4. Finally, once all relevant aspects of the engineering problem have been summarized, Section 1.6 delves into the thesis structure and main goals.

1.1. The engineering problem

Cutting is one of the fundamental processes in the mechanical industry. Milling, turning and drilling machines are at the core of traditional cutting techniques, that allow to create custom parts in many industrial applications, machining the desired shape and size with high precision [2], [3],[4], [5].
Although widely applied, these methods are usually time-consuming, and they also suffer from other limitations. For instance, the equipment may be expensive, and the setup quite demanding. In addition, since they rotate at very high speeds, cutting tools might be subjected to serious wear, that significantly affects their performance and lifetime. Therefore, frequent maintenance is required for these kind of machines. Finally, since the material removal is attained by exploiting friction, heating is not negligible. This could influence the durability of the equipment and alter the mechanical properties of its parts.
The previous considerations should help to understand the increasingly growing demand

of innovative cutting techniques, such as Abrasive Water Jet Machining (AWJM). This is a modern technology that combines the cutting ability of water jets with the abrasive action of a dispersed phase, namely solid particles. AWJM has developed rapidly in the mechanical industry, since it opens up the possibility of manufacturing materials that the traditional techniques are not able to handle due to mechanical or thermal constraints. AWJM can be applied to cut both brittle and ductile materials, which makes it a really versatile method. For instance, this technique is widely used in the machining of metals, such as steel or aluminium, but also glass, plastics and composites. Fig. 1.2 shows a close-up of the water-jet cutting process, while Fig. 1.3 reports the results of AWJM on different materials. In the micro-mechanical applications, AWJM is used for cutting sandwiched materials and fragile parts, as it involves small forces on the workpiece, thus minimizing the risk of fracture ([6]). Finally, it also eliminates the problem of machining dust, which is a danger for the workers' health and for the environment.

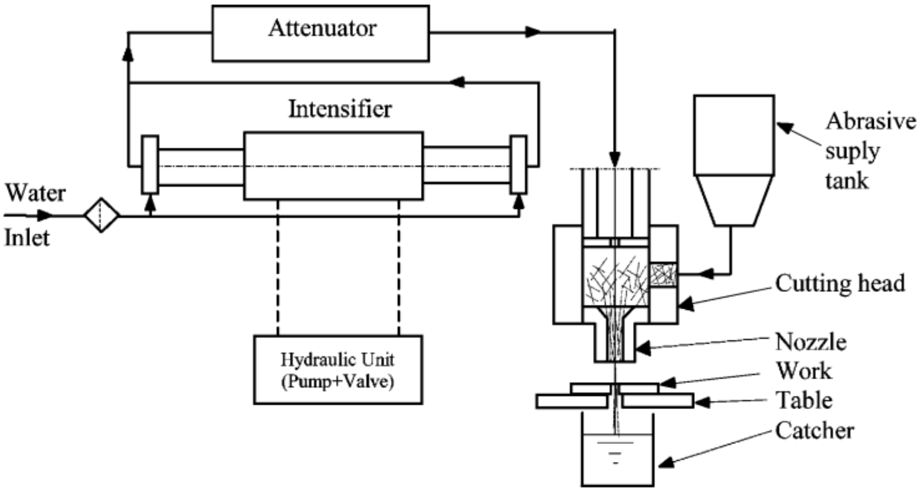

Figure 1.1: The typical layout of an AWJM cutting system (picture from [6]).

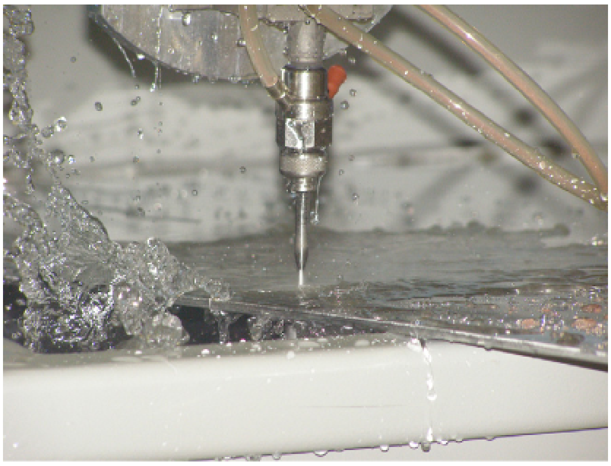

Figure 1.2: A close-up on a AWJM head (picture from [7]).

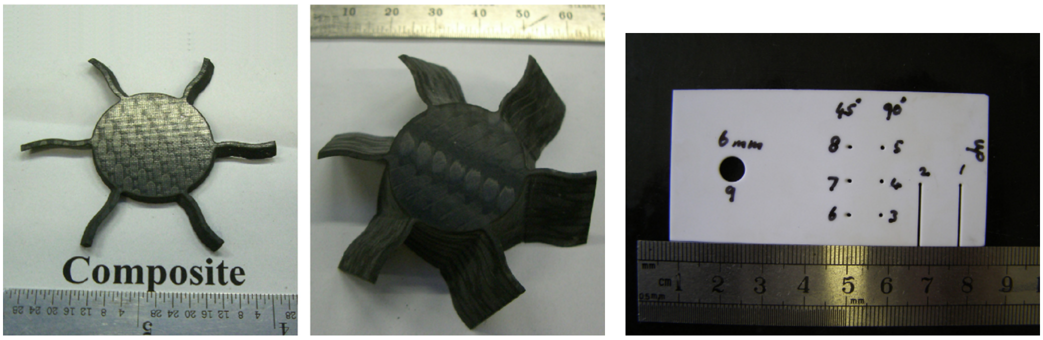

(a) AWJM on a composite material.

(b) AWJM on a ceramic material.

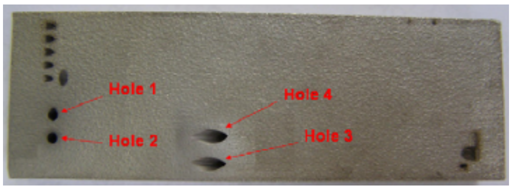

(c) AWJM on nickel.

Figure 1.3: Examples of abrasive water jet machining of a composite material (a), ceramics (b) and nickel (c) (Pictures from Folkes et al. [7]).

Figure 1.1 shows the typical layout of an AWJM cutting system. An intensifier pump is used to provide high-pressure water flow. The abrasive supply tank directs the abrasive medium to the cutting head, moved via a computer controlled manipulator, where it mixes with the water flow, so that a proper cutting jet is produced. The abrasive jet will, subsequently, impact the workpiece and then discharges into a catcher, that dissipates the remaining kinetic energy.

In spite of the strengths discussed here above, abrasive water jet machining presents some

drawbacks. In particular, producing the high pressure flow is energy-consuming, thus requiring a great effort by the pump, and it is also difficult to control, which may result in a low precision cutting. In addition, since the solids are added to the water in motion, the slurry is not well mixed, and this might create dishomogeneity and accentuate the nozzle wear [8].
In order to meet these challenges, a variant of the technique has been developed, in which the water flow and the dispersed phase are pre-mixed to obtain a more homogeneous slurry. This is called Abrasive Slurry Jet Machining (ASJM). The operating pressure will be lower than that of AWJM (up to two orders of magnitude), yielding a better controllability of the flow, but without affecting the cutting ability.

Compared to AWJM, ASJM is particularly successful in micro-manufacturing. Indeed, also Abrasive Air Jet Macihning (AAJM) has been widely applied to the fabrication of micro-components, as in micro-electro-mechanical systems (MEMS) [9] or in the micro-fluidic industry [10], but some disadvantages of this third technique have been pointed out. In fact, due to the low density of air, the particles tend to diverge quickly after exiting the nozzle, yielding a less accurate cutting [11]. Moreover, Wensink et al. [12] have noted that the surface quality of AAJM workpieces was very low. The use of erosion resistant masks has been proposed, that should be shaped according to the desired pattern and increase the resolution of the cutting process.

The drawbacks of AAJM machining, as well as those of AWJM, are overcome, or at least minimized, by ASJM, a very promising technique for industrial cutting. In order to optimize the ASJM, both a better understanding of the process of material removal, i.e. erosion, and an appropriate characterization of the particle-laden flow are required.

Accurately modelling particle-laden flows is crucial, when investigating an erosion phenomenon. The particles' motion is strongly connected to the evolution of the flow surrounding them, therefore a complete understanding of the dynamics of particle-wall collisions must be based on a suitable physical description of the fluid-dynamic problem.

Solid particle erosion is at the basis of ASJM, and it is a very complex phenomenon. It involves different physical scales and a variety of micro-processes (plastic deformation, indenting, cutting, repeated deformation). Erosion modelling state-of-the-art methods are analysed in Section 1.3.

1.2. Particle-laden flows

A particle-laden flow is a two-phase flow made of a carrier fluid, either a liquid or a gas, mixed with solid particles. More precisely, a particle-laden flow is a special case of a dispersed two-phase flow, where the dispersed phase consists of solid particles. A phase is said to be dispersed when its particles are not in direct contact with each other.

The solid phase is characterized by particles' size distribution and particles' shape. The former is experimentally determined by examining a granular sample in a sieve analysis, that groups the particles by their size. The latter is usually described by the particle spherical coefficient, $\phi = A_{sphere}/A_p$, that is defined as the ratio between the surface area of a sphere having the same volume of the particle A_{sphere} and the particle's surface area A_p. The particle spherical coefficient is often included in the modelling equations, as particles' shape affects the way they are transported by the flow, but it is difficult to quantify for a mixture of natural solids. Its influence on CFD simulation results has been discussed in [1].

The behaviour of the solid phase in the fluid flow can be assessed through the particle response time τ_p, that is the time it takes for a particle to react to changes in the fluid velocity, and the particle Stokes number St_p, defined as the ratio between the particle response time τ_p and the characteristic time scale of the fluid flow τ_f (Eq.1.1).

$$St_p = \frac{\tau_p}{\tau_f} \tag{1.1}$$

Particles with low values of St_p are carried by the fluid, while particles with high values of St_p are not influenced by the flow, so their motion is dominated by inertia.

Another key aspect of the dynamics particle-laden flow, which has a strong impact on the numerical simulation, is the type of coupling between the two phases. The most general type of interaction between the two phases is the four-way coupling regime, in which the influence of the flow on the particles, the disturbances induced by the particles on the flow and the collisions between particles are all important. Simpler coupling regimes are often considered in the numerical simulations to reduce the computational effort. In the one-way coupling regime, only the influence of the flow on the particles is considered, while in two-way coupling the effect of the dispersed phase on the flow in introduced, still neglecting interaction between particles. In the three-way coupling regime, the interaction between particles is accounted for in an indirect sense: particles influence the flow, that, in turn, affects other particles' motion.

When dealing with turbulent gas-solid flows, the distinction among these regimes is well represented by Elgobashi's map ([13]), which identify the coupling regime as a function of the volume fraction of the particle phase, namely the ratio of the volumetric flow rate of the solid phase to the global flow rate $\alpha_p = \frac{\dot{W}_p}{\dot{W}}$, and the particle Stokes number, defined with respect to the integral time scale of the turbulent fluid flow. In slurry erosion simulations, a practical criterion for the validity of the one-way coupling regime is that the volume fraction of the solid phase is lower than about $\alpha_p = 1\%$ [14]. However, Lester et al. [15] applied a one-way coupling model to a slurry flow with 7% of abrasive volumetric concentration, which may be questionable from a physical point of view, but still represents a simplified way to approach the problem.

Industrial applications of particle-laden flows are numerous. For instance, slurry pipelines are employed in mining engineering to transport mineral concentrate from the extraction site to the processing plant. Particle presence is often an unavoidable side-effect, like in oil and gas production or hydro-power plants, whose influence on the flow and the transportation system needs to be considered. Solid particle erosion affects both the flow dynamics and the mechanical durability of the system.

1.3. Solid particle erosion

Erosion is the physical phenomenon of material removal, usually due to friction, direct impact with another medium, high-pressure wave propagation (cavitation) or chemical reaction. In the case of AWJM and ASJM, a fluid flow drives solid particles of an abrasive material up to the workpiece causing its progressive deterioration. This is called solid particle erosion, often referred to as slurry erosion in the case of ASJM.

In manufacturing, erosion is exploited as a tool to cut and shape materials. Differently, in applications like turbomachinery or oil and gas production, erosion is a threat, as it deteriorates the working system (turbine blades, pipelines etc.), reducing the life expectation of the operating device and negatively affecting its performance (Fig.1.4). Therefore, studying and understanding this process to a deeper level could be relevant from the industrial point of view, to design more resistant systems and predict and prevent the wear process.

Figure 1.4: Effect of sand erosion in a gas transport pipeline (from [16]).

A basic way to study erosive effects on a system is to carry out on-field testing and inspection. This means analysing the structural integrity and performance of a device working in an actual erosive environment and looking for a correlation between the observable wear and the performance decay in time. As simple as it is, this approach hardly yields quantitative information, but rather a generic indication on how serious the erosion phenomenon is in a certain application and if it should be accounted for in the design process. Many easy-to-use, case-specific formulas have been proposed through the years to assess erosion relevance ([17],[18],[19],[20]), but with no predictive ability on its location and intensity.

In order to gain a better quantitative prediction, laboratory experiences should be performed. As they involve a controlled environment, it is possible to study the effect of single physically relevant parameters on erosion. Nevertheless, this approach requires a real workpiece to undergo a rather destructive testing process, thus making the whole analysis quite costly, or, alternatively, a scaled model, requiring an up-scaling of the obtained results, that is often a non-trivial task.

A third, more promising, way is the use of Computational Fluid Dynamics (CFD). Numerical analysis allows to get an insight on the particle-laden flow behaviour and impact dynamics, drastically reducing the need for laboratory testing or field measures. As the computational power increases, CFD becomes more and more affordable and efficient in this kind of research. The role of CFD in erosion modelling is explored in Section 1.4.

1.3.1. Basic erosion mechanisms

The most widely accepted intuition on solid particle erosion is to correlate the observable deterioration of the sample material to the particles' impacts. A solid particle, transported by the surrounding flow, impinges on a target surface, causing material removal (Fig.1.5).

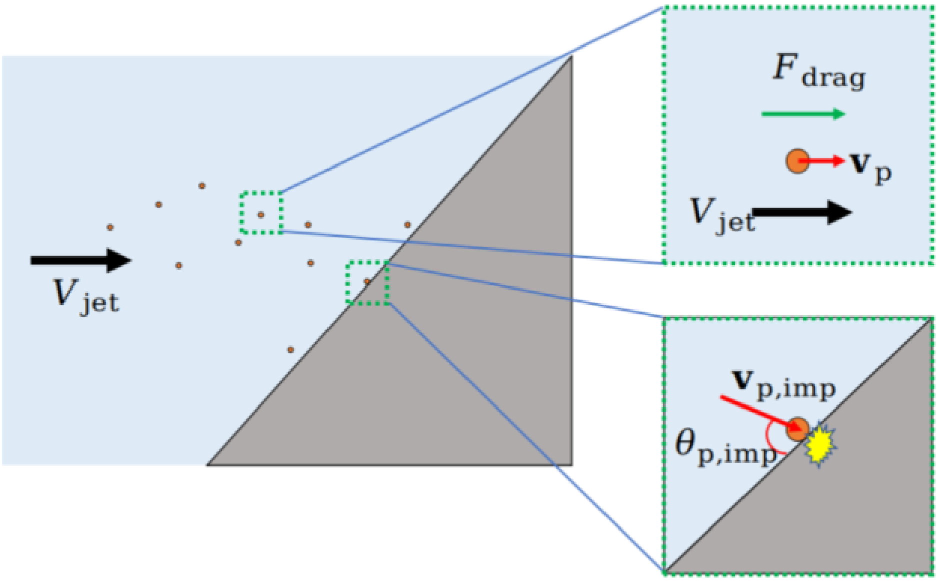

Figure 1.5: A sketch of particles impinging on a wall (from [1]).

One of the pioneering studies on erosion was due to Finnie et al. ([21]), in which the two main erosion mechanisms were identified, namely, cutting and deformation. Those terms are still a well established terminology for the characterization of erosion, as pointed out in the review paper by Javaheri et al. [22].

The cutting mechanism is associated with particles impacting the target surface at an oblique angle with enough kinetic energy to cause a fragment to detach, whereas the deformation mechanism is associated with particles impacting at normal impact angle with enough kinetic energy to induce plastic deformation or subsurface crack formation in the target material and, finally, failure. Note that, as discussed in the review paper by Javaheri et al. [22], not only the impact angle, but also the impact velocity can affect the relative weight of the two erosion mechanisms.

Both mechanisms could occur in ductile and brittle materials, and the dominant one depends on the ductility of the target material. For this reason, another common classification is the one between ductile erosion and brittle erosion. As sketched in Fig. 1.6, ductile erosion with low impact angle ("oblique impact" in the sketch) involves material removed by cutting, whereas ductile erosion under high impact angle ("normal impact" in the sketch) involves ductile fracture. Conversely, the leading features of brittle erosion are fractures and cracks, consequences of particle impingements.

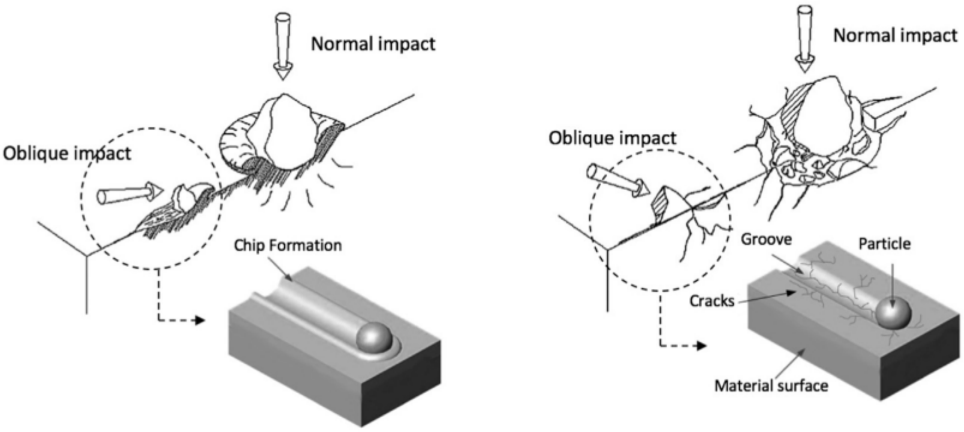

(a) Ductile erosion.

(b) Brittle erosion.

Figure 1.6: A sketch of the ductile (a) and brittle (b) erosion mechanisms (Pictures from Javaheri et al. [22]).

In this work, experimental data on ductile materials, namely aluminium and stainless steel SS304, are examined. Due to the importance of ductile materials, such as steel, in civil, hydraulic and industrial applications, the process of ductile erosion has been thoroughly investigated. Many different ways of modelling have been proposed in the literature and good results have been achieved in terms of erosion prediction. The simplified model proposed by Finnie et al. ([21]) in the 70's, which will be presented later in Section 1.3.4, turned to be accurate at low impact angles. Tilly et al. ([23]) have proposed a two-stage mechanism, namely a first stage where particle impacts create indentation and extrusion of structurally weak hillocks, and a second one where the actual removal takes place. Hutchings et al ([24]) saw the erosion process as three-fold, including particles plowing on the target surface and two types of cutting, depending on the particle impact velocity.

In order to develop appropriate modelling methods, the key parameters affecting erosion must be identified, as explained in the next section.

1.3.2. Key erosion parameters

Completely grasping the physical process and model it physically is a quite complicated task. Erosion is an intrinsically multiphase phenomenon, as it involves a macroscale, the fluid flow that drives the dispersed solid phase and its dynamics, and a microscale, namely the single, localized particle impact and its mechanical consequences.

In order to shed light on the complex phenomenon, it is necessary to identify the relevant physical parameters. Numerous physical parameters influence erosion. Primarily, fluid-related properties, such as flow velocity, fluid viscosity and temperature are relevant. Flow velocity clearly affects the particles' motion, thus influencing the trajectory and kinetic energy at the stage of impact. Fluid viscosity plays a more subtle, and in a way still unclear, role. It affects erosion indirectly, by changing the flow dynamics, hence modifying particles' motion. Mansouri et al. [25] have investigated the erosion of stainless steel caused by liquid-sand flows, using three different viscosities, finding that the erosion ratio seemed uninfluenced, but the maximum erosion depth increased with viscosity. A different result was obtained by Kowsari et al. [26], who analysed the effect of polyethylene oxide (PEO), a non-Newtonian fluid, on micro-machined channels in borosilicate glass. In this study, a decrease in maximum depth, while increasing the fluid viscosity, was observed.

Mechanical properties related to the abrasive medium and target material also affect the erosion phenomenon. Particles' size has a two-fold effect, as it influences both the particle's motion and the impact kinetic energy of the particle. Bigger, heavier particles impinge less frequently, but with higher kinetic energy. Nevertheless, the erosion damage dependence on kinetic energy has been found to be non-linear [27] and so the actual effect on erosion depth remains unclear, as opposing results are observed ([28], [29], [30], [31]). Moreover, particles' size affects their trajectories, influencing the erosion mechanism and location. A shift towards the specimen center was observed, when particles' size was increased [32].

The effect of particle shape is more subtle and difficult to physically quantify. Beyond the particle sphericity coefficient ϕ, proposed by Wadell [33], different parameters have been defined [34], [35] and no full agreement has yet been reached on which best captures the physical relation with erosion. As for experimental observations, comparative studies have been carried out on erosion resulting from rounded and angular particles impingements. An increase in erosion from four to five times was detected when using angular particles [36], [37].

Levy et al. [36] also investigated the role of particles' hardness. It was found that erosion increased with particles' hardness up to a critical value, then plateaued. The ratio between particles' hardness and target material hardness is known as relative hardness. A more refined approach would require to study the influence of this parameter on erosion. It was found by Wada et al. [38] that erosion decreases drastically when the relative hardness in less than one, on brittle materials.

Clearly, target material properties play a key role in particle erosion. Ductility is believed to make it more resistant to erosion [39], [40], [41]. Hardness has a similar effect, as proven in [42] and [43]. However, it should be noted that the influence of a single mechanical property is difficult to isolate, in light of their strong interconnection. For instance, hardening techniques are often employed to increase material hardness, but they also reduce its ductility, thus doubly influencing the erosion result, as previously mentioned.

Many other physical factors affect the erosion process. Particle deterioration leads to a different particle size, usually without altering the particle shape; flow temperature may affect the mechanical properties of the target material, other than the viscosity of the fluid itself. The change of geometry of the target, when exposed to particle erosion for a long time, will influence the flow dynamics. The abrasive concentration, if high enough, may hinder erosion, as the particles filling the channel, or hole, provoke a screening effect, that slows down and deflects the incoming flow, as observed by Nouraei et al. [11]. The role of self-induced geometry changes has been further investigated in Messa et al. [44] and Parsi et al. [45].

Finally, the influence of impact properties has to be mentioned. Erosion dependence on particle impact velocity, as an indicator of its kinetic energy, is usually regarded as a power law [46], even if some issues stemming from this physical intuition have been pointed out and an alternatives discussed, by Lester et al. [15].

Particle impact angle affects the way a particle impacts on the target wall, thus changing the main erosive mechanism, as cutting is usually seen as more relevant at small angles, while plastic deformation seems to be dominant at high impingement angles [21], [46].

1.3.3. Benchmark laboratory tests

As previously mentioned, on-field testing for erosion analysis is a direct, yet limited, source of information. It is impossible to ascertain the actual, precise, operating conditions of the observed system (particle concentration, flow velocity etc.). Moreover, this approach has a limited applicability, since it is based on real deteriorated systems. The main goal of erosion analysis is to understand it and prevent it, when needed. Therefore, laboratory tests have been used to have a better control over the operating conditions and investigate the erosion phenomenon and its dependence on relevant parameters. A series of benchmark cases has been developed to have a standard for the comparison of different materials and conditions.

In this section, the two main benchmark tests are listed and discussed, namely the Dry Direct Impact tests (D-DIT) and the Wet Direct Impact tests (W-DIT).

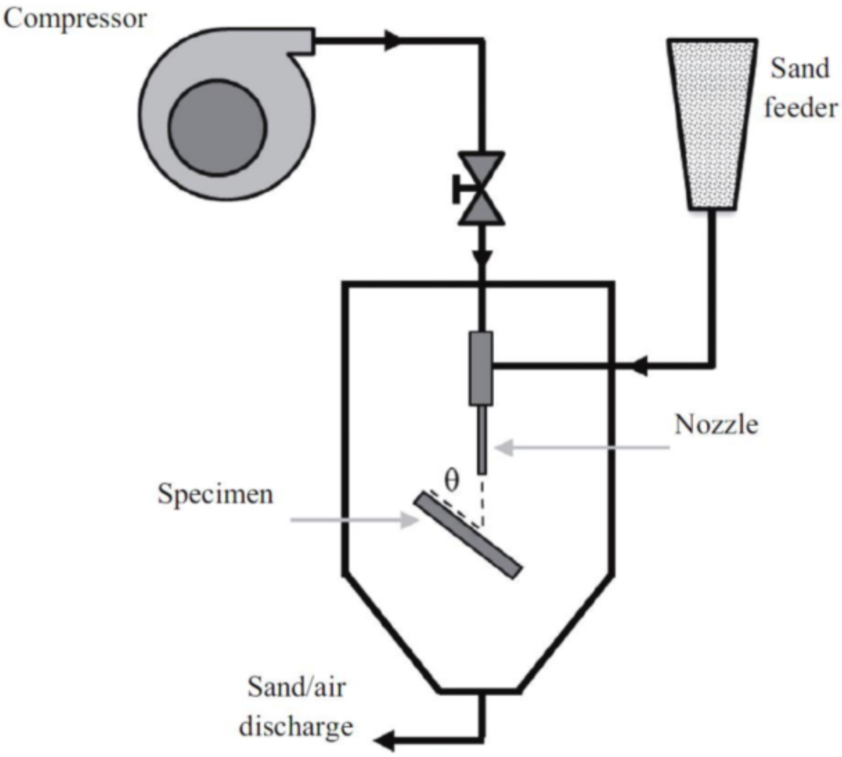

Figure 1.7: Diagram of a D-DIT for air-sand flow (from [47]).

Fig. 1.7 show a schematic representation of a D-DIT. A compressor accelerates the air flow, that is driven to the specimen through a pipeline system. A particle-feeder is required to channel the abrasive medium to a mixing area, where it will get dispersed in the air flow. The mixture will, then, exit through the nozzle, impact the specimen and be collected in a discharge zone.

The specimen holder can be tilted, in order to measure the effect of particle impingements at different angles. This kind of test allows to fix the impact angle, thus highlighting the effect of impact velocity on erosion. This is possible because of the very nature of a D-DIT, as the motion of particle is mainly driven by inertia, given the low density of the carrier fluid (air). Therefore, the particles' impact angle may be approximated with the geometric angle between the nozzle direction and the specimen surface.

Conversely, the particles' impact velocity cannot be assumed to be close to that of the air flow, since the low density of air allows for slip between the abrasives and the surrounding air. This implies that a velocimeter should be used. Some suggestions may be found in the literature regarding this aspect. One of the most popular ways to measure particle impact velocity is the two-disk method, proposed by Ruff et al. [48], while a more recent technology allows for the use of a Laser Doppler Velocimetry system (LDV) [49].

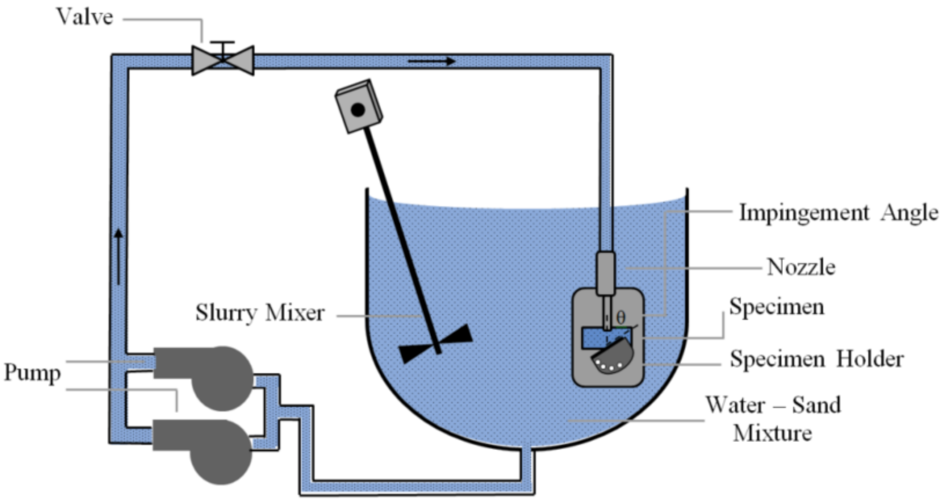

Figure 1.8: Diagram of a W-DIT (from [47]).

In Fig. 1.8, another widely used kind of test is sketched, namely the Wet Direct Impact test (W-DIT), specifically, a submerged W-DIT. The W-DIT is conceptually similar to the D-DIT, but it involves a liquid as a carrier fluid (usually water) that impacts the specimen in a submerged environment. The use of a liquid flow implies that a closed-loop system is required.

There are two main ways to design a W-DIT, as represented in Fig. 1.9. Zu et al. ([50]) have proposed a test rig where the abrasive particles were sucked from a container, mixed with the water flow before impacting the specimen, then collected and filtered out of the fluid. A conceptually different design has been proposed by Turenne et al. ([51]), that mixed the abrasive medium with the fluid flow to create a homogeneous slurry and used a more expensive pump to circulate the slurry directly. Both approaches have pros and cons. The first requires a less expensive pump, that needs to operate solely on water. Plus, filtering out abrasive particles means that only a limited part of the pipeline system will be affected by erosion, thus simplifying maintenance. The main disadvantage is that this process of mixing and filtering does not yield a uniform concentration of abrasive particles, so the experiments repeatability will be affected and confidence in the results will be lower. The second design allows to maintain a uniform concentration, but presents more severe erosion damages to the circulating system and requires a much more powerful pump.

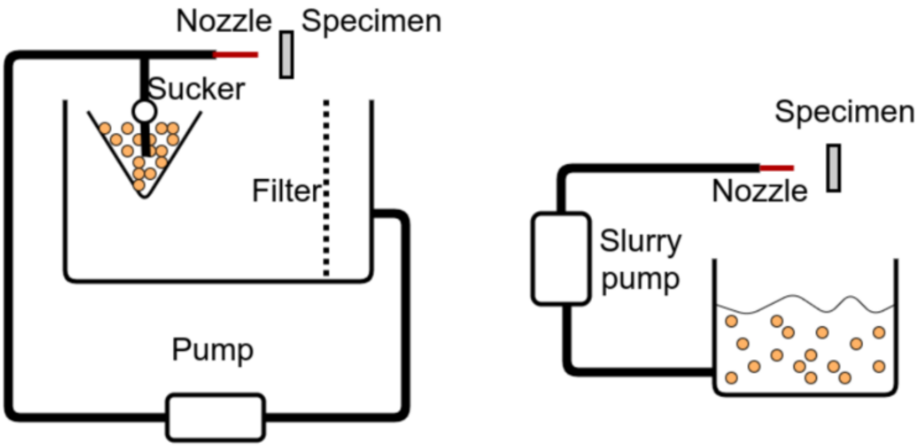

Figure 1.9: A sketch of the two ways a W-DIT can be performed (from [1]).

A W-DIT is a more sophisticated system than a D-DIT. It requires a more structured setup and does not allow to approximate neither the particles' impact angle nor the particles' impact velocity (magnitude and direction) with the flow angle and velocity, but its experimental conditions are closer to most hydraulic application, that involve a liquid as a carrier fluid. The main drawback of direct impact tests is that they hardly recreate impacts at very low angles (less than 10°), thus making the resulting study on a model equation limited to the impact angle range actually attained by the particles at the moment of impact.

Other test designs are worth to be mentioned, like Slurry Pot Erosion tests ([52]), where the slurry is continuously mixed in a containing pot and the test specimen are attached to the same rotating shaft that keeps the slurry in motion. In Coriolis tests ([53]), Coriolis force is exploited to drive the slurry up to the specimens. In Pipe Loop tests ([54]), a pump is used to circulate the slurry in a closed-loop pipe, where the specimen is a cavity or a small protrusion installed in the loop.

1.3.4. Phenomenological erosion models

Several mathematical formulations have been proposed by researchers through the years, to improve erosion prediction.

One of the earliest relations, still widely used, has been reported in Finnie et al. ([21]). It states a linear dependence of the mass erosion rate $\dot{E}_p$ caused by a single particle stream on the local particle impact rate $\dot{m}_p$ $[kg\, m^{-2}\, s^{-1}]$ multiplied by a power law for impacts speed v_{imp} with exponent n, originally suggested to be equal to 2, and an impact angle function $f(theta)$ (Eqs. 1.2-1.3). This model has been proven to be pretty accurate for low impact angle erosion, but lower performances have been observed for high values. The reason could reside in the absence of a plastic deformation term in the equation, which only accounts for the cutting action, that is the most relevant erosion mechanism at low impact angles.

$$\dot{E}_p = \dot{m}_p \, v^n \, f(\theta) \tag{1.2}$$

$$f(\theta) = f_0 \begin{cases} \frac{1}{3}\, cos(\theta)^2 \,\textbf{if}\, tg(\theta) > \frac{1}{3} \\ sin(2\theta) - 3\, sin(\theta) \,\textbf{if}\, tg(\theta) \leq \frac{1}{3} \end{cases} \tag{1.3}$$

Bitter [55] tried to modify the previous equation by accounting for plastic deformations. He proposed a two-fold correlation for cutting, depending on a critical value of the impinging angle and resulted in a quite complicated model, that was later simplified by Neilson and Gilchrist [56]. A phenomenological model was set up by Huang et al. ([57]), that accounted for the role of impingement velocity and angle, other than particle size and target material properties. The two-fold action, namely cutting and plastic deformation, was included.

1.3.5. Fully empirical erosion models

Many empirical models have been proposed, in addition to the phenomenological ones. Most of them are structured as Finnie's equation, showing an impact angle function $f(\theta)$ (that should include both cutting and plastic behaviour) multiplied by a velocity function, that is typically assumed to be a power law. All other contributions are accounted for in a multiplicative coefficient K (Eq. 1.4).

$$\dot{E}_p = K \, \dot{m}_p \, v^n \, f(\theta) \tag{1.4}$$

These models are empirical, meaning they carry the same functional dependencies of a phenomenological models, but are characterized by relations and coefficients derived from the fitting of experimental data.
Zhang et al. ([58]) proposed an equation in the form of Finnie's, working on a series of tests with Inconel 718 (Eq.1.5).

$$\dot{E}_p = C \, (BH)^{-0.59} \, F_s \, \mathbf{v}_p^n \, f(\theta) \tag{1.5}$$

where BH is the Brinnel hardness, F_s is an empirical particle shape factor which accounts for the effect of particle shape, v_p and θ are the particle impact speed and angle. The velocity exponent n is suggested to be equal to 2.41 and the empirical constant C is equal to $2.17 \cdot 10^{-7}$.

Oka et al.([46]) widened the scope of the study, working with many different materials and combination of erodent/target material, to find out Eqs. 1.6-1.7.

$$\dot{E}_p = \rho_t \, \dot{E}_{90} \, f(\theta) \tag{1.6}$$

$$f(\theta) = (sin(\theta))^{n_1} \, (1 - H_v \, (1 - sin(\theta)))^{n_2} \tag{1.7}$$

This model states that it is possible to find out the erosion rate at any angle θ, just by knowing the erosion rate at normal impact $\dot{E}_90$ and the target material density ρ_t. The coefficients n_1, n_2 and the erosion rate $\dot{E}_90$ can be expressed as a function of the Vicker's hardness H_v, particle impact velocity and diameter (see [46]).

1.4. CFD role in erosion prediction

Erosion modelling, in the last several years, has been based on empirical relations, or, alternatively, on theoretical models, that attempted to capture its complexity from both a microscopic perspective and a macroscopic one.

All of the found correlations identify impact speed and impact angle as the most relevant parameters in the erosion process. Other influencing variables are connected to the flow characteristics and the mechanical properties of the target material and of the abrasive medium (flow conditions, fluid viscosity, particle and target material density, specimen hardness, particle size and shape etc.).

D-DIT-based models provide a good insight on erosion, but they are quantitatively inaccurate when used out of their range of calibration, for instance in liquid-particle flows. In these cases, W-DIT-based models are more suitable, but they carry some challenges, like how to accurately measure the particle impact characteristics. A promising approach requires to involve Computational Fluid Dynamics in the process of erosion prediction.

CFD provides a much less expensive way than laboratory measurements to investigate the flow evolution and the interaction between the phases. The particle-laden flow could be modelled using an Eulerian-Eulerian approach, in which both phases are interpenetrating continua. However, in slurry erosion simulations, the most straightforward choice is to employ an Eulerian-Lagrangian approach, in which the fluid flow is modeled in the

Eulerian, cell-based framework, and the Lagrangian trajectories of computational particles are calculated. In this case, as the solid concentration in slurry erosion applications is generally small, the one-way coupling regime assumption is often made, which allows computing particle's trajectories after the flow has been solved. The one-way coupled Eulerian-Lagrangian models used in this thesis are detailed in Chapter 2.

CFD can be regarded, consequently, as a powerful tool to be integrated in the erosion analysis and improve the accuracy of the used models. Nevertheless, it carries some sources of uncertainty and numerical issues. Fluid flows in transport and manufacturing applications are most likely to be turbulent, therefore, a suitable simulation framework requires to appropriately choose a turbulence model, together with the near-wall treatment method. In addition, the computational burden required to track each particle could become unbearable, so simplifying assumptions on the particles' shape, distribution and behaviour must be made. Particles' behaviour is one of the most critical parts of CFD modelling of particle-laden flows. A two-phase flow simulation requires to account not only for the interaction between the two phases but also between particles. This is paramount in an Eulerian-Lagrangian simulation, as it could increase the computational effort drastically. In the experiments relevant to this thesis, the solid phase concentration is always low enough for the one-way coupling regime to be a suitable approximation.

In addition to the challenges posed by numerical modelling, some of the previously mentioned difficulties of erosion prediction still need to be handled. For instance, the choice of the right erosion correlation constitutes for sure an open problem.

To end this section, some of the most relevant attempts at involving CFD in erosion studies are listed.

Benchaita et al. ([59]) were among the first researchers to use a CFD simulation in this kind of analysis. They performed a two-dimensional, steady, potential flow simulation, neglecting the turbulent fluctuations, to solve a fluid flow in an impinging jet test. They tracked the particles by solving their equation of motion singularly. A potential flow simulation does not account for the boundary layer, so it is not surprising that they found an accurate prediction of the erosion peak, but a quantitative overestimation of the scar depth.

More recently, Zhang et al. ([37]) applied CFD to study air-sand and water-sand flows, finding out that the results were less accurate for the fluid case. It seems evident that erosion prediction in slurry flows is a tricky problem. Okita et al.([60]) showed that fluid viscosity is relevant, by finding out that the erosion prediction becomes less accurate as fluid viscosity increases.

As for the interaction between abrasive particles, Nguyen et al. ([61]) observed that increasing the abrasive concentration leads to a decrease in erosion depth. This is in agreement with experimental measurements and may be a consequence of the interaction between solid particles, that slow each other down and reduce impact frequency.

1.5. The SAER approach for the calibration of erosion models

The present work is based on a previous PhD research study, conducted by Yongbo Wang at the Politecnico di Milano in 2021 [1], in which an innovative approach to erosion modelling is proposed, extending an earlier work by Amir Mansouri from the University of Tulsa [47].
The core idea of this research is to combine in-situ measurements of erosion profiles with numerical simulations. Computational fluid dynamics (CFD) can provide information on the velocity vector of each particle colliding with the sample; then, by reverse-engineering, it is possible to find a suitable model to correlate particles' impact statistics with the actual scar depth.

Developing a mathematical expression to predict and quantify solid particle erosion rate is a complicated task. Many parameters have to be considered, like particle impact speed, particle impact angle, mechanical properties of both the abrasive medium and the target surface (hardness, density, particle size and shape), fluid flow conditions and characteristics. As previously discussed, the vast majority of models typically applied rely on a phenomenological description of the wear phenomenon, or on a fully empirical treatment. The main criticism of phenomenological models resides in the high number of difficult-to-decide parameters, coefficients and sub-models. Conversely, empirical models are easy to use and generally perform well within the calibration range [62], but they suffer of poor predictive capacity outside the calibration conditions, which are often unknown to users.

In continuation with a study conducted by Sugiyama et al. [63], in 2015, Mansouri et al. [64] proposed a combined numerical-experimental methodology aimed at providing a case-specific calibration of an empirical erosion model. This was expected to produce advantages especially for the estimation of slurry erosion. As a matter of fact, empirical models are often derived from Dry Direct Impact Test (Section 1.3.3), where the impact velocities are much higher than the typical values encountered in slurry erosion processes.

The basic idea of this approach, called SAER (Surface profile Aided ERosion Prediction) in the PhD thesis of Yongbo Wang [1], is to execute a Wet Direct Impact Test in the laboratory and measure the erosion depth profile. Then, reproduce numerically the slurry flow in the same test obtaining the fluid dynamic characteristics of the particles at the impact stage. The two information are then combined to calibrate the coefficients of an erosion model, after selecting its mathematical form. This idea is sketched graphically in Fig. 1.10.

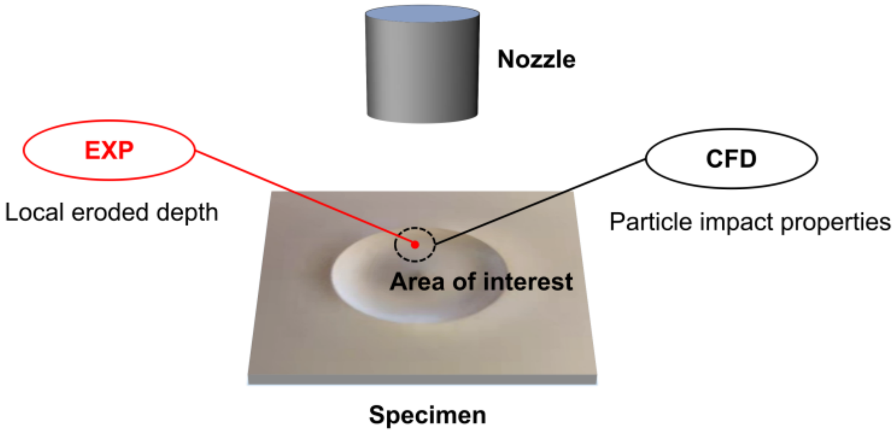

Figure 1.10: Combining CFD results with experimental measurements on erosion depth (from Wang [1]).

The SAER approach is the core of the present thesis. The mathematical details of the SAER formulation initially employed, which will be further improved during the work, will be given in Section 2.4.

1.6. Thesis structure and purpose

This thesis is divided in four chapters. The first has introduced the ASJM problem, the existing modelling techniques, the relevance of this procedure for industrial purposes and the limitations of the main state-of-the-art ways to study it.

In Chapter 2, the mathematical models for erosion prediction employed in this thesis are presented. A detailed discussion of the one-way coupled Eulerian-Lagrangian models used for the simulation of the test cases is first made. Then, the Surface Aided Erosion prediction (SAER) for producing an empirical erosion model through the combination of laboratory data and CFD results is presented in the formulation of the Phd thesis of Wang [1], which stands at the very basis of the following chapters.

In chapter 3, the application of this approach to calibrate the impact angle function in a given erosion model is reported. The found equation is, then, applied to test-cases to assess its performance outside the range of calibration.

Chapter 4 revolves around possible ways to improve the proposed fitting procedure. Some modifications are suggested and tested. Finally, Chapter 5 describes the application of the procedure to a different test case, involving a significantly smaller geometry and a free slurry jet, to recreate the testing conditions typical of ASJM.

2 | Mathematical models

Since erosion models require as input the fluid dynamic characteristics of the particles at the stage of their impingement against the target walls, the most straightforward choice to simulate a particle-laden flow is to use an Eulerian-Lagrangian model. As already mentioned in Sec. 1.4, in the Eulerian-Lagrangian approach the fluid flow is solved in the Eulerian, cell-based framework, whereas the motion of the solid phase is represented by calculating the trajectories of a certain number of computational particles. In this thesis, owing to the low solid concentration of the two considered test cases (around 1% in the first and 2.7% in the second), the one-way coupling regime assumption is made, which means that the fluid flow fields is calculated first and, afterwards, the particle trajectories are determined sequentially without changing the fluid flow field anymore. The CFD simulations presented in this thesis have been performed using Ansys Fluent 2022.

In this chapter

2.1. Calculation of the submerged water jet

In light of the one-way coupling regime assumption, the fluid dynamic model used for the simulation of the submerged water jet case described in Chapters 3-4 is a standard, single-phase one. The starting point in the modelling of the water flow are the Navier-Stokes equations which, in the incompressible case, read as follows,

$$\nabla \cdot \mathbf{u}_f = 0 \tag{2.1}$$

$$\rho_f \frac{\partial \mathbf{u}_f}{\partial t} + \rho_f \left(\mathbf{u}_f \cdot \nabla\right) \mathbf{u}_f = \rho_f \mathbf{g} - \nabla p + \mu \nabla^2 \mathbf{u}_f \tag{2.2}$$

where $\mathbf{u}_f$ is the flow instantaneous velocity, p_f the instantaneous pressure, ρ_f the fluid density and μ its dynamic viscosity.

Since the jet flow is turbulent, direct solution of the Navier-Stokes equation would require excessive computational cost. Therefore, their Reynolds-Average formulation is solved.

The core idea of this approach is to only solve for the average velocity and pressure fields. This is attained by applying an averaging operator (Eq. 2.3) to the two equations, the Reynolds-average operator, so that each property $\phi(\mathbf{x}, t)$, function of space and time, will be expressed as the sum of its time-average over a very long time window, $\hat{\phi}$, and a turbulent fluctuation term ϕ' ($\phi(\mathbf{x}, t) = \hat{\phi}(\mathbf{x}) + \phi'(\mathbf{x}, t)$).

$$\hat{\phi}(\mathbf{x}) = \lim_{T \to \infty} \frac{1}{T} \int_0^T \phi(\mathbf{x}, t) dt \tag{2.3}$$

After applying the Reynolds-average operator, the Navier-Stokes equations become

$$\nabla \cdot \mathbf{U}_f = 0 \tag{2.4}$$

$$\rho_f \left(\mathbf{U}_f \cdot \nabla \right) \mathbf{U}_f = \rho_f \mathbf{g} - \nabla P + \mu \nabla^2 \mathbf{U}_f + \nabla \cdot \tau_{Re} \tag{2.5}$$

where $\mathbf{U}_f = \hat{\mathbf{U}}_f$ and $P_f = \hat{p}_f$ are the mean velocity and pressure. The term $\tau_{Re} = -\rho \widehat{\mathbf{u}'\mathbf{u}'}$ can be interpreted as the additional stresses that the velocity fluctuations exert on the mean flow field, and it is called Reynolds stresses tensor. Its presence makes the system of equations 2.4 - 2.5 not closed, demanding for additional closure equations, which are called turbulence model. In the present work, the $k - \epsilon$ Realizable model is used, together with the Scalable Wall Function approach for the modelling of turbulence in the near-wall region, in continuity with the study detailed in [1].

Eq. 2.4 - 2.5 are known as the Reynolds-Averaged Navier-Stokes equations (RANS). These equations are inherently steady, and they apply to statistically steady turbulent flows.

2.2. Calculation of the free water jet

In the case study described in Chapter 5, the slurry jet is free, in the sense that it discharges from the nozzle in an open air environment. This required employing an Eulerian-based two-phase model capable to simulate the flow field of the water jet (without particles) and the surrounding air. Owing to the one-way coupling regime assumption, the particles trajectories are calculated afterwards.

The solution of the two-phase flow was computed using the Volume of Fluid (VOF) method, embedded in Ansys Fluent 2022. Section 2.2.1 describes the model.

2.2.1. The Volume of Fluid Method

The Volume of Fluid (VOF) model allows to model two or more immiscible fluids by solving a single set of momentum equations and tracking the volume fraction of each of the fluids throughout the domain. It is typically applied to unsteady problems, like the prediction of jet breakup, the motion of large bubbles in a liquid, the motion of liquid after a dam break, but it can also be used when dealing with a steady problem, like tracking liquid-gas interface (e.g. when modelling the flow of water in a channel with a region of air on top and a separate air inlet). A steady-state VOF calculation is reasonable only when the solution is independent of the initial conditions and there are distinct inflow boundaries for the individual phases. A RANS-based VOF simulation was performed in Chapter 5 to solve the two-phase flow in a steady-state framework.

The VOF method requires to solve the conservation equations introducing a new variable, the volumetric concentration, for each added phase. When modelling, for instance, gas-bubbles in a water flow, the unsteady Reynolds-averaged mass conservation equation for water is written as in Eq.2.6

$$\frac{\partial \alpha_w}{\partial t} + \nabla \cdot (\alpha_w \mathbf{U}_f) = 0 \tag{2.6}$$

where $\mathbf{U}_f$ is the average flow velocity and α_w is the volumetric concentration of water. A similar equation can be written for the air volume fraction α_a, Eq. 2.7. A single momentum equation is solved (Eq.2.8)

$$\frac{\partial \alpha_a}{\partial t} + \nabla \cdot (\alpha_a \mathbf{U}_f) = 0 \tag{2.7}$$

$$\frac{\partial \rho \mathbf{U}_f}{\partial t} + \nabla \cdot (\rho \mathbf{U}_f \mathbf{U}_f) = -\nabla P + \nabla \cdot \left[\mu \left(\nabla \mathbf{U}_f + \nabla \mathbf{U}_f^T\right)\right] + \nabla \tau_{Re} + \rho \mathbf{g} + \mathbf{F}_{st} \tag{2.8}$$

where $\rho = \alpha_w \, \rho_w + \alpha_a \, \rho_a$ and $\mathbf{F}_{st}$ is the surface tension, given by

$$\mathbf{F}_{st} = \nabla \cdot \left[\sigma \left(|\nabla \sigma| I - \frac{\nabla \sigma \otimes \nabla \sigma}{|\nabla \sigma|}\right)\right]. \tag{2.9}$$

Therefore, the found properties, like the velocity and pressure field, are shared by the two phases in the control volume.

The whole system of equations is then closed by accounting for the relationship between the volume fractions (Eq.2.10), whose sum must be equal to 1.

$$\alpha_w + \alpha_a = 1. \tag{2.10}$$

2.3. Calculation of the particles' trajectories

The utility embedded in Ansys Fluent for the Lagrangian tracking of the particle trajectories over an Eulerian flow field is the Discrete Phase Model (DPM). One of its main assumptions is that the particles are treated as material points (point-particle approximation) and, therefore, that they are much smaller compared to size of the computational cells. In the RANS framework, on the mean fluid flow is calculated. Thus, the forces acting on the particles cannot be obtained by the pressure and shear stresses distributions over their surface. Use is then made of force model, which estimates the action on the particle from the RANS solution.

The Lagrangian equation of motion is

$$m_p \frac{d\mathbf{v}_p}{dt} = \mathbf{F}_m + \mathbf{F}_{fp} + \mathbf{F}_{pp} \tag{2.11}$$

where $\mathbf{v}_p = \frac{d\mathbf{x}_p}{dt}$ is the instantaneous particle velocity, being $\mathbf{x}_p$ the particle's position, m_p is the particle mass, $\mathbf{F}_m$ is the sum of the mass forces, $\mathbf{F}_{fp}$ represents the action of the fluid on the particle and $\mathbf{F}_{pp}$ accounts for the interaction with the other particles, which is ignored in the one-way coupling regime.

The only relevant mass force in typical applications is the gravitational force, Eq. 2.12, while the action of the fluid on the particle can be rewritten as Eq. 2.13

$$\mathbf{F}_m = m_p \, \mathbf{g} \tag{2.12}$$

$$\mathbf{F}_{fp} = \mathbf{F}_{drag} + \mathbf{F}_{buoyancy} + \mathbf{F}_{pressure} + \mathbf{F}_{virtual\,mass} + \mathbf{F}_{lift} \tag{2.13}$$

with buoyancy force as in Eq.2.14. The pressure force is given by the gradient of the part of pressure which is not balanced by gravity, computed at the particle location, (Eq.2.15) and the virtual mass force accounts for the acceleration of the fluid surrounding the particle (Eq.2.16).

$$\mathbf{F}_{buoyancy} = -\rho_f \frac{m_p}{\rho_p} \mathbf{g} \tag{2.14}$$

$$\mathbf{F}_{pressure} = -\frac{m_p}{\rho_p} \nabla p \tag{2.15}$$

$$\mathbf{F}_{virtual\,mass} = C_{vm} \rho_f \frac{m_p}{\rho_p} \left(\frac{d\mathbf{v}_p}{dt} - \frac{d\mathbf{u}_{@p}}{dt} \right) \tag{2.16}$$

where ρ_f ρ_p is the fluid and particle density. C_{vm} is a constant coefficient, the virtual mass coefficient, usually assumed to be equal to 0.5. The unhindered fluid velocity $\mathbf{u}_{@p}$ is the fluid velocity extrapolated to the particle center, neglecting disturbances caused by the particle itself. The fluid velocity considered in the DPM corresponds to the water velocity in the submerged wet test reported in Ch. 3, while it is equal to either the air or water velocity in the two-phase framework discussed in Ch. 5, according to which fluid is present in each computational cell.

Once the average fluid velocity has been computed, the instantaneous value can be estimated via a suitable turbulence model, like the Discrete Random Walk (DRW) model, that stochastically adds a turbulent disturbance to the mean field dependent on the local value of turbulent kinetic energy.

The lift force, for the scope of this thesis, will be modelled according to Mei et al. [65], Eq. 2.17.

$$\mathbf{F}_{lift} = 3.0844\; J\; \frac{m_p}{\rho_p\, d_p} \sqrt{\frac{\nu}{|\Omega_{@p}|}}\; \left[\Omega_{@p}\; \times (\mathbf{u}_{f@p} - \mathbf{v}_p)\right] \tag{2.17}$$

where ν is the kinematic viscosity of the fluid, $\Omega_{@p}$ is the fluid vorticity computed at the particle position, $\mathbf{u}_{u@p}$ is the fluid velocity computed at the particle position and J is a dimensionless parameter, whose expression can be found in [65]. The lift expression proposed by Mei is considered to be a suitable adaptation of the Saffman lift force [66] for finite Reynolds regimes and it was adopted in this thesis, in accordance with what had been done in [1].

The drag force (Eq. 2.18) is expressed as a function of the relative velocity of the particle with respect to the undisturbed fluid flow.

$$\mathbf{F}_{drag} = \frac{1}{2} \rho_f C_d \left(\pi \frac{d_p^2}{4} \right) |\mathbf{u}_{@p} - \mathbf{v}| \left(\mathbf{u}_{@p} - \mathbf{v} \right) \tag{2.18}$$

where the drag coefficient $C_d = C_d(Re_p)$ is a function of the particle's Reynolds number $Re_p = d_p|\mathbf{u}_{@p} - \mathbf{v}|\rho_f/\mu_f$. The correlation proposed by Haider and Levenspiel [67] will be used in this thesis, Eq. 2.19, in continuity with [1].

$$C_d = \frac{24}{Re_p}\left(1 + b_1 Re_p^{b_2} + \frac{b_3 Re_p}{b_4 + Re_p}\right) \tag{2.19}$$

Coefficients b_1, b_2, b_3 and b_4 only depend on the particle's shape factor ϕ, suggested to be equal to 1 for perfectly spherical particles and less than 1 otherwise. The explicit expressions for the coefficients and more details on the selection of the value of ϕ can be found in [67].

Particle-wall collisions need to be accurately handled, as they play a fundamental role in the prediction of erosion. Two restitution coefficients $e_{\mathbf{t}} = \mathbf{v}_t^{after}/\mathbf{v}_t^{before}$ and $e_{\mathbf{n}} = \mathbf{v}_n^{after}/\mathbf{v}_n^{before}$, are introduced to relate the tangential and normal particle velocity components before and after an impact against a wall boundary. One of the most widely used models for the particle restitution coefficients has been proposed by Forder et al. [68], Eqs. 2.20-2.21, which has been used for the calculation reported in this thesis.

$$e_{\mathbf{n}} = 0.993 - 0.78\theta_{p,imp} + 0.19\theta_{p,imp}^2 - 0.024\theta_{p,imp}^3 + 0.027\theta_{p,imp}^4 \tag{2.20}$$

$$e_{\mathbf{t}} = 1 - 0.78\theta_{p,imp} + 0.84\theta_{p,imp}^2 - 0.21\theta_{p,imp}^3 + 0.028\theta_{p,imp}^4 - 0.022\theta_{p,imp}^5 \tag{2.21}$$

As a typical approach in the Lagrangian tracking of the particle trajectories, the parcel approach was used in this study. Tracking every single particle could lead to a cumbersome simulation, therefore groups of neighbouring particles are often modelled as one. This allows saving considerable computational time without significant loss in terms of accuracy. As a consequence, the number of particles used in the numerical simulations does not correspond to the number of particles actually present in the modelled experiment.

Particles tracking is, then, performed in a steady-state regime, meaning that the integration time used in the computation of particles' motion is a mathematical variable, unrelated to the actual physical time characterizing the modelled phenomenon. To link the parcels to the real solid phase flow rate, each parcel is associated a mass flow rate as in Eq. 2.22, that stays constant along the trajectory,

$$\dot{m}_p = \frac{\pi D^2 V_{jet}\hat{c}}{4N_p} \tag{2.22}$$

where V_{jet} is the flow jet velocity, $\hat{c}$ the particle concentration, D the nozzle diameter and N_p the number of particles injected.

2.4. Erosion model calibration through the SAER approach

As already introduced in Section 1.5, the SAER approach allows calibrating an erosion correlation by combining the experimental and numerical results of a Wet Direct Impact Test. This will allow producing a case-specific empirical erosion model, calibrated for the range of impact velocities typically encountered in slurry erosion. Here, the mathematical details of the SAER formulation which constitutes the starting point of this thesis are provided. The formulation is that reported in Messa et al. [69].

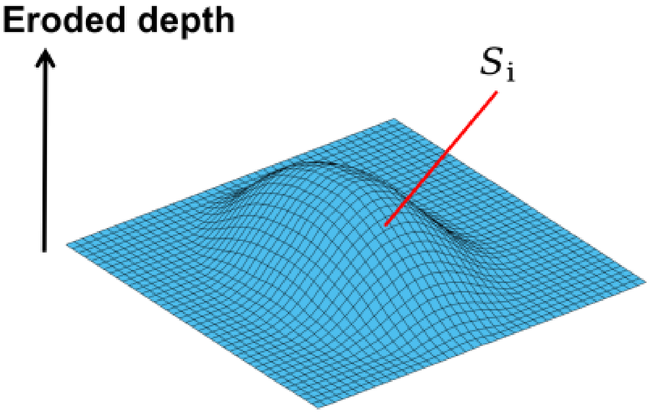

Figure 2.1: The sample surfaces divided in squared cells (from Wang [1]).

The core idea of the procedure is to divide the target surface into small squared cells (Fig. 2.1) and write, in each cell i, a functional relation for the erosion rate caused by the impingement $\dot{E}_p$ and the erosion ratio ER_i, defined as the ratio between the mass removed in the cell and the total mass of abrasive particles impinging on that cell.
$\dot{E}_p$ is usually modelled as in Eq. 2.23

$$\dot{E}_i = \dot{m}_p \, F(\bar{v}_{p,i}, \bar{\theta}_i, \text{other parameters}) \tag{2.23}$$

where $\bar{v}_{p,i}$ is the average particle impact velocity and $\bar{\theta}_i$ is the average impact angle, computed on cell i. Assuming that the non-dimensional function F can be written as the product of an impact velocity function (usually modelled as a power law with exponent n)

and an impact angle function $f(\theta)$, thus treating these two as independent, and that the influence of other physical parameters, such as geometrical and mechanical properties of the abrasive and target material can be grouped in a multiplicative coefficient K, Eq.2.23 becomes Eq. 2.24.

$$\dot{E}_i = \dot{m}_p \, K \, \bar{v}_{p,i}^n \, f(\bar{\theta}_i) \tag{2.24}$$

Thus, the erosion ratio of the cell can be rewritten as Eq. 2.25

$$ER_i = \frac{\sum_{j=1}^{N_{imp@i}} \dot{E}_{P,j}}{\dot{m}_p \, N_{imp@i}} \tag{2.25}$$

where $\dot{E}_{P,j}$ is the erosion rate of particle j, $N_{imp@i}$ is the total number of impingements in cell i and N_p is the number of particles impacting on cell i.
The predicted mass loss over cell i can be expressed as Eq. 2.26

$$m_{loss} = \dot{m}_p \, t \, N_{imp@i} \, ER_i \tag{2.26}$$

ans so the predicted eroded depth in cell i, h_i can be estimated as Eq. 2.27

$$h_i = \frac{t \, \sum_{j=1}^{N_{imp@i}} \dot{E}_{P,j}}{\rho_t \, S_i} \tag{2.27}$$

In Eqs. 2.26-2.27, S_i is the surface area of cell i, ρ_t is the target material density, $\dot{m}_p$ is the mass flow rate associated to the particle trajectories in steady-state tracking, see Sec. 2.3, (assumed equal for all trajectories).

Combining Eq. 2.24 with Eq. 2.27 one gets

$$K \, f(\bar{\theta}_i) = \frac{\rho_t \, S_i \, h_i}{N_p \, \dot{m}_p \, t \, \bar{v}_{p,i}^n} \tag{2.28}$$

The values of h_i, S_i, and ρ_t are obtained experimentally. Conversely, $\bar{v}_{p,i}$,$\dot{m}_p$, N_p, and $\bar{\theta}_i$ are outcome of the numerical simulation. By combining all this information, one can get the function $K \, f(\theta)$ using regression techniques. This requires, on the one hand, deciding the value of the velocity exponent n and, on the other hand, disposing of a suitable regression model for the impact angle function.

The velocity exponent n is typically in the range between 2 and 4. This is usually measured performing different D-DIT tests with different jet velocities and fixed jet angle ([70]). However, in the original formulation of Mansouri [64], as well as in the subsequent ones by Messa et al [69] and Wang [1], this coefficient was kept fixed and equal to 2.1.

The model for the impact angle function was chosen as in Eq. 2.29, an equation proposed by Mansouri in [64]. In Wang [1], both Eq. 2.29 and the Oka model, Eq. 1.7, were considered and compared.

$$F_s\ K\ f(\bar{\theta}_i) = f_1\ \left(sin(\hat{\theta}_{p,imp})\right)^{f_2}\ \left(1.5 - sin(\hat{\theta}_{p,imp})\right)^{f_3} \tag{2.29}$$

In case of an axisymmetric flow field impacting on a flat surface, Messa et al [69] proposed to divide the sample surface in concentric rings (annuli), as in Fig. 2.2, instead of referring to square cells as in Fig. 2.1 The averaged quantities will be then computed over each annulus i.

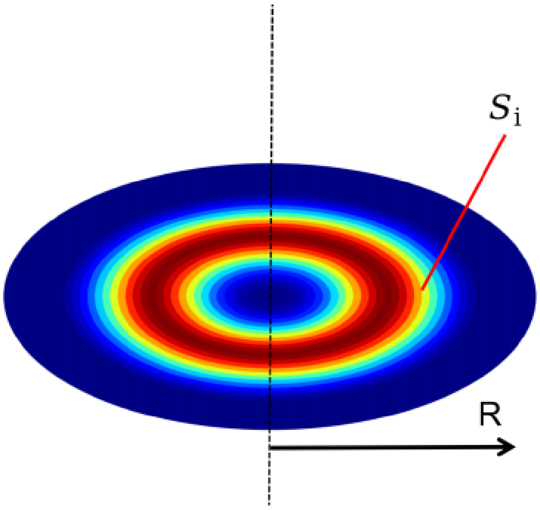

Figure 2.2: The sample surface divided in concentric rings (from Wang [1]).

In conclusion, it must be noted that the SAER formulation described so far is steady state, thus it ignores erosion-induced geometry changes. Accounting for these effects would drastically increase the computational effort, so it has been shelved for future research. This limits the applicability of the method to relatively shallow erosion depths.

2.4.1. Possible improvements to SAER

The method used so far is a quite simplified model of a complex phenomenon, since the point-particle approach stems from a blunt approximation.

To include the influence of particle's size in the model, Messa et al.[69] have computed impact statistics at a distance from the sample surface exactly equal to r_p, the particle's radius. This yields higher impact angles and velocities, since a particle is deflected and slowed down the most when it is closest to the physical wall.

In addition, the effect of particle's size can be included in the calibrated equation, as in the original Oka model [46]. This allows explicitly taking into account the different diameter when testing the model performance on different cases (like cases 5, 12 and 20 in the previous section). The mentioned improvements to the model have been developed in [69] and [1] .

3 | Application of SAER to an existing case

In this chapter, the SAER procedure is applied to a test case already analysed by Wang in [1]. Experimental data from a submerged direct impact test are exploited to calibrate the coefficients of an erosion model. Then, the predictive capacity of the found erosion equation is assessed, by applying it to different test cases and comparing the outcome to the experimental profiles. Sec. 3.1 summarises the main features of the laboratory tests, while more detailed reference on the experimental layout and settings can be found in [1]. Sec. 3.2 describes the numerical settings of the CFD simulation performed to solve the single-phase flow. Due to the low particle concentration used in the laboratory tests, particles' motion is computed after the fluid flow has been solved, in a one-way coupling regime. See Sec.3.3 for more details on how the trajectories have been found. The application of the SAER approach in a ring-based framework and the application of the erosion formula to predict the profiles resulting from different experiments are shown in Sec.3.4. Finally, Sec.3.5 lists the sensitivity studies conducted on relevant parameters of the numerical simulation.

3.1. Notes on the experimental tests performed by Dr. Wang [1]

To investigate the erosion phenomenon, numerous wet direct impact tests have been carried out ([1]) in the Direct Impact Tester (DIT) facility installed in the Hydraulic Laboratory "Gaudenzio Fantoli" at the Politecnico di Milano. Figure 3.1 shows a sketch of the slurry loop. Water and solid particles were premixed in Tank A, where a rotating shaft prevented an excessive accumulation of particles at the bottom. A KSB Etanorm water pump, whose flow rate could be controlled by regulating valve 2° circulated the slurry through the loop. In order for the nozzle and the specimen to stay submerged by the slurry in Tank B throughout the experimental sessions, valve 3∘ was used to set the discharging flow rate equal to the incoming one, as soon as the slurry level was high

enough. A Proline Prosonic Flow 91 ultrasonic flowmeter, from Endress+Hauser, was used to measure the flow rate, while a pressure transducer upstream of Tank B monitored the flow pressure. The nozzle had an 8 mm diameter and the stand-off distance, i.e. the distance between the nozzle and the specimen surface, was 12.7 mm. Figs. 3.2b-3.2a and Fig. 3.3c depict the installation of the nozzle-specimen system in the test cabin. More information on the experimental setup and post-processing details in Wang [1].
In this chapter, in particular, the application of the SAER approach to the case of a slurry made of water and glass beads impacting on a rectangular aluminium sample is detailed, Figs. 3.3a-3.3b.

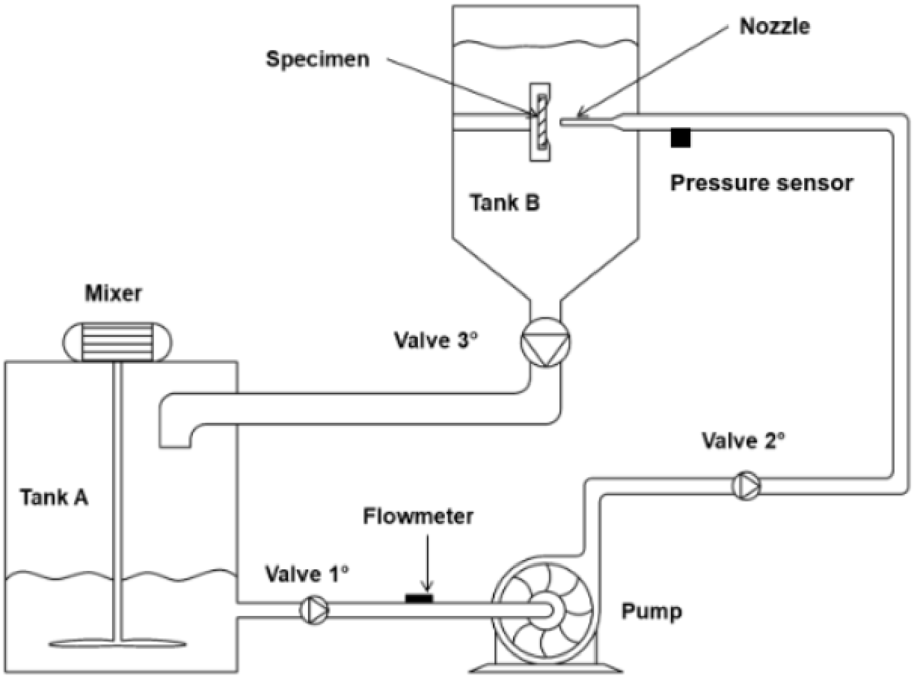

Figure 3.1: Sketch of the testing facility (from Wang [1]).

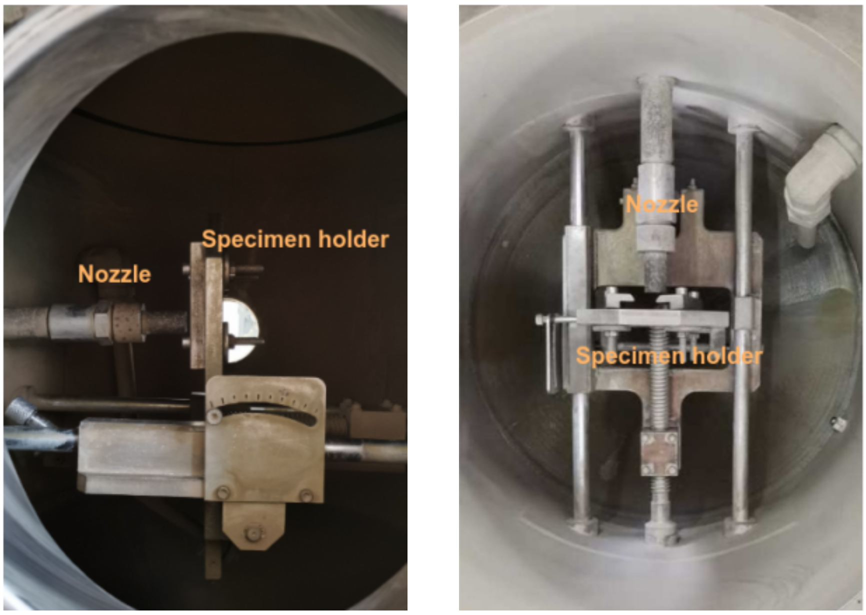

(a) Front view. (b) Top view.

Figure 3.2: Front and top view of the test section of the DIT (Pictures from Wang [1]).

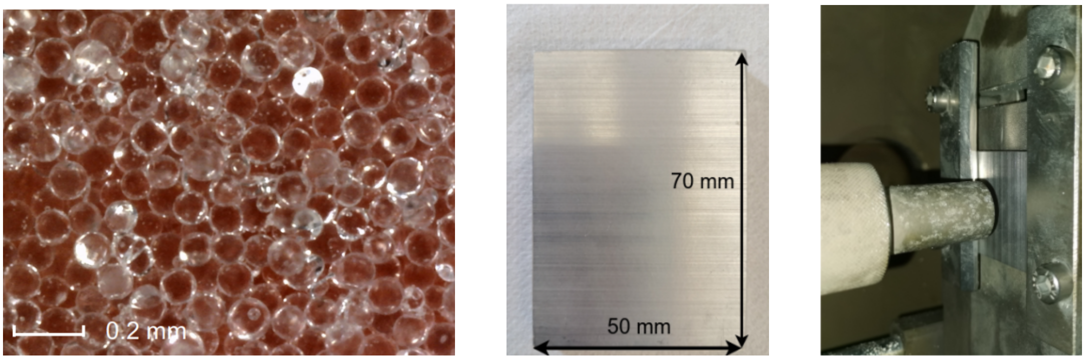

(a) Glass beads. (b) Aluminium sample. (c) DIT setup.

Figure 3.3: Glass beads (90 μm diameter) used for the experiments; aluminium sample and installation (Pictures from Wang [1]).

Since the presented modelling technique is based on a steadiness assumption, the modification to the sample surface due to erosion are implicitly neglected. Therefore, only shallow profiles can be accurately modeled, as deeper holes would require accounting for geometry changes, that directly affect the flow evolution.

Four of the experimental tests reported in the PhD thesis of Dr. Wang [1] are considered here. The main experimental settings of the referenced tests are shown in Table 3.1, where

d is the particle diameter, V_{jet} is the jet velocity, θ_{jet} the jet angle with respect to the sample and $\hat{c}$ the dispersed phase volumetric concentration. Following the nomenclature reported in [1], the SAER method was applied to fit an erosion formula on the experimental erosion depth profile of case 1, in which the mean diameter of the glass beads was 90 μm. In Fig. 3.3a, a picture of the glass beads used in case 1 is reported, while Fig. 3.3b show an aluminium sample. The calibrated erosion model was, then, used to predict erosion caused by bigger particles (as in cases 5, 12 and 20), in order to assess the accuracy of the approach outside its range of calibration. A picture of the erosion pattern in case 20 in Fig. 3.4

	d [μm]	exp. time [min]	$V_{jet}[m/s]$	θ_{jet}	$\hat{c}$
case 1	90	60	35.97	90°	0.93%
case 5	120	45	33.54	90°	1.26%
case 12	250	45	35.69	90°	1.31%
case 20	350	45	35.98	90°	1.24%

Table 3.1: Experimental settings for the reference tests.

Figure 3.4: Erosion pattern in case 20 (from Wang [1]).

3.2. CFD simulation setup

The CFD simulation has been performed using Ansys Fluent 2022. Henceforth, the numerical setup is described and the results detailed.

3.2.1. Geometry and discretization

The computational domain shown in Figure 3.5 has been created in SpaceClaim, the graphical tool integrated in Ansys Workbench 2022 R2. The problem is axisymmetric, as experimental observation confirms 3.4. Therefore, it is natural to sketch the sample surface as a 50 mm diameter circle. The nozzle, perpendicular to the sample, is 40 mm long, with a 4 mm radius. The stand-off distance is set to 12.7 mm.
Unstructured tetrahedral cells were used to mesh the domain, as shown in Figure 3.6. The near-wall elements were created through the use of an inflation layer consisting of 10 layers, with first layer thickness equal to 0.05 mm and 1.05 expansion ratio, applied to each wall boundary (nozzle surface and sample). The closest elements to the sample surface are the ones where particles' impact statistics will be computed. Here, the flow velocity will be deflected by the collision with the solid wall and reduced by the boundary layer, causing a sudden change in the drag force exerted on the solid particles. This is why a significant refinement of this part of the computational mesh is required, to accurately capture the flow evolution and, consequently, the particles' dynamics.

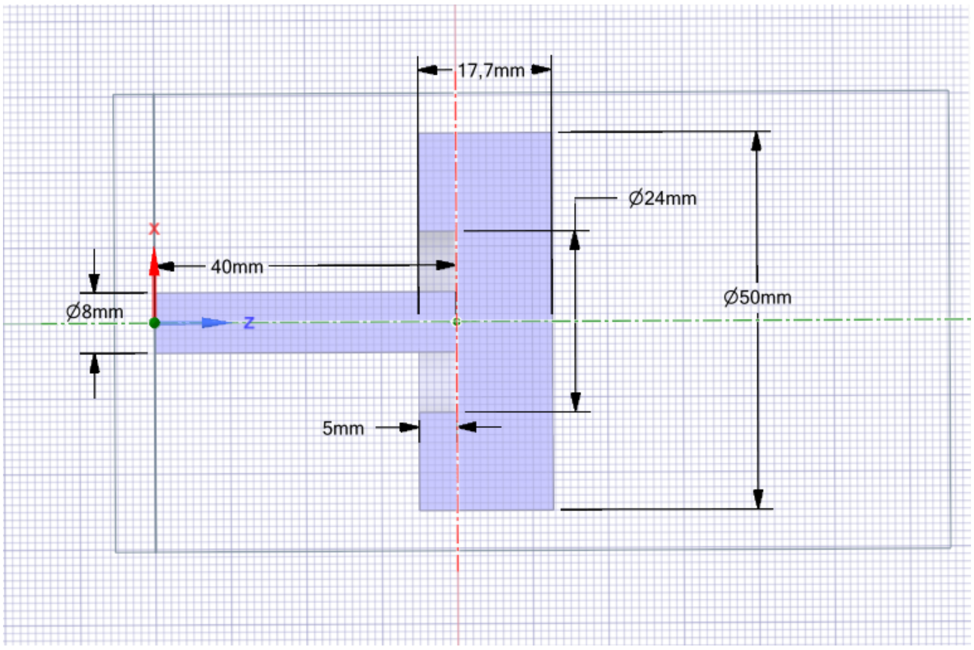

Figure 3.5: Transverse section of the computational domain.

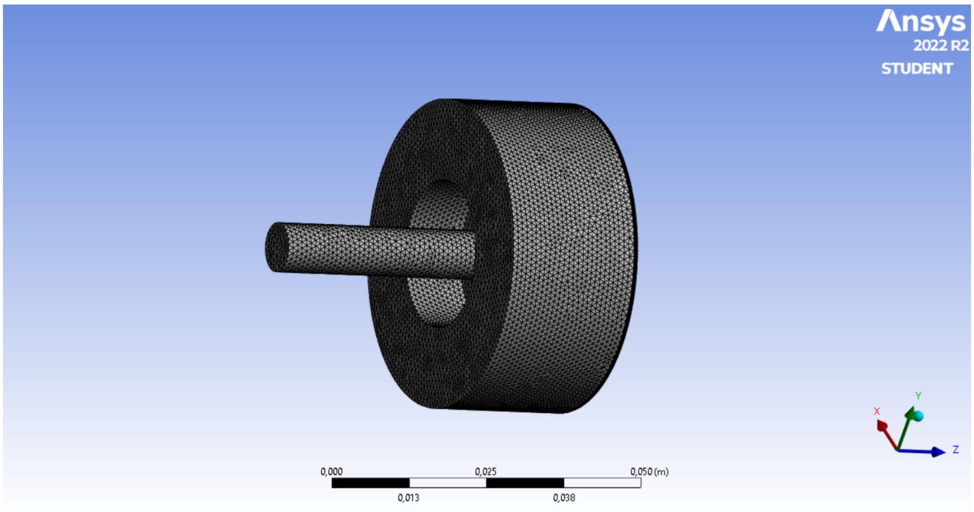

Figure 3.6: Computational mesh.

Ideally, the finer the mesh, the more accurate the expected result. However, refining the grid too much will drastically increase the computational burden. Therefore, a suitable compromise between the two needs to be found. This is done through a grid-independence study, where different meshes are tested and the effect of mesh refinement on some target parameters is assessed. See Section 3.2.4 for more details about the grid-independence study on the problem at hand.

3.2.2. Fluid-dynamics models and numerical settings

The key details of the numerical setup are summarized in Table 3.2.

Turbulence model	$k-\varepsilon$ realizable
Near-wall treatment	Scalable wall function
Solver	Pressure-based, steady
Pressure-velocity coupling	SIMPLE
Discretization accuracy	second order

Table 3.2: Main numerical settings of the CFD simulation.

Unless specified, all settings were kept as default. The $k-\varepsilon$ Realizable turbulence model was used, in continuity with the approach used in [47] and [1]. Moreover, a comparative study conducted in [47] and [14] asserts that the numerical predictions on erosion only show a mild dependence on the selected turbulence model. The Scalable Wall function model was selected for the near-wall treatment. The SIMPLE algorithm was selected to handle the pressure-velocity coupling and all discretization schemes were accurate at second order, as in [1].

The erodent concentration was set to 1%, according to the low values characterizing the reference experiments [1], thus allowing for the use of a one-way coupling approach in the Eulerian-Lagrangian framework. This means solving a one-phase simulation, computing the stationary flow field, then tracking the particles' trajectories. Clearly, this approach eases the computation and can only be used if the dispersed phase concentration is so low that its effect on the fluid flow is negligible.

3.2.3. Flow boundary conditions

The boundaries of a CFD domain are usually grouped in two categories. If a numerical boundary corresponds to a solid surface in the modelled physical experience, it is called a physical boundary. This is the case of the nozzle and sample surfaces. If not, it is called a virtual boundary, like the inlet and outlet boundaries.

Concerning the virtual boundaries, at the inlet, Fig. 3.7a, a fully developed turbulent channel flow for the velocity profile was set, using the 1/7 power law of Nikuradse for smooth pipes and assuming a mean axial velocity equal to 35.96 m/s. At the outlet, Fig. 3.7b, atmospheric pressure was imposed.

A no-slip, smooth-wall condition was applied to the physical walls, Figs. 3.8a-3.8b.

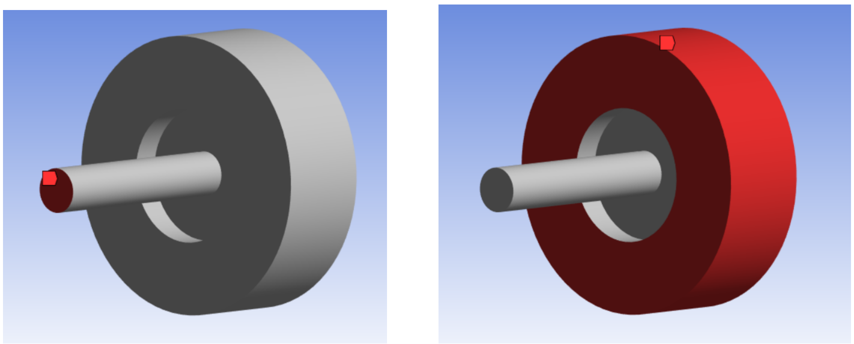

(a) Inlet. (b) Outlet.

Figure 3.7: Inlet and outlet boundaries of the computational domain.

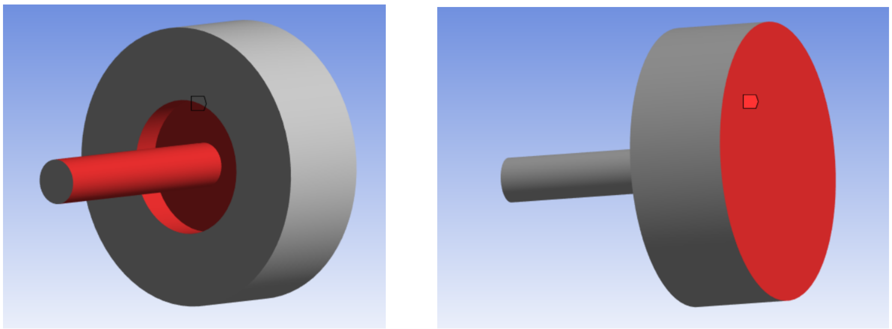

(a) Nozzle wall. (b) Sample wall.

Figure 3.8: Nozzle and sample wall of the computational domain.

3.2.4. Grid-sensitivity study

The first feature one should take care of, when running a CFD simulation, is that the results have to be independent of the mesh characteristics. This is called grid-sensitivity study and it has been performed repeating the flow simulation for different values of mesh element size, creating five meshes with progressively increasing refinement level. Five meshes were analysed, the corresponding number of elements is reported in Table 3.3. Once the one-phase flow solution has been proven to be grid-independent, one can be confident that it depicts the real flow with good accuracy.

	Number of elements [million]
mesh 1	0.43
mesh 2	1.2
mesh 3	2.0
mesh 4	3.0
mesh 5	3.9

Table 3.3: Tested meshes.

To assess convergence of the simulation, the normalized residual criterion was used, setting a 10^{-6} threshold. The area-averaged static pressure on a plane at a distance of 1 mm from the sample wall was monitored. The simulation results were assumed to be grid independent when the values of this parameters over two subsequent meshes varied within a 1% tolerance. The outcome of the grid sensitivity study is shown in Figure 3.9. Results stemming from meshes 3, 4 and 5 can be regarded as grid-independent, according to the selected criterion.

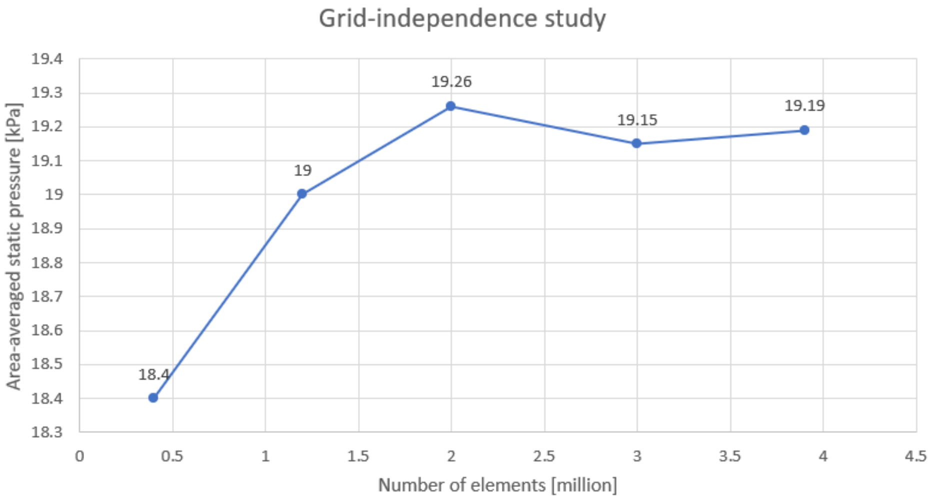

Figure 3.9: Grid-sensitivity study based on the area-averaged static pressure on a plane 1 mm from the sample.

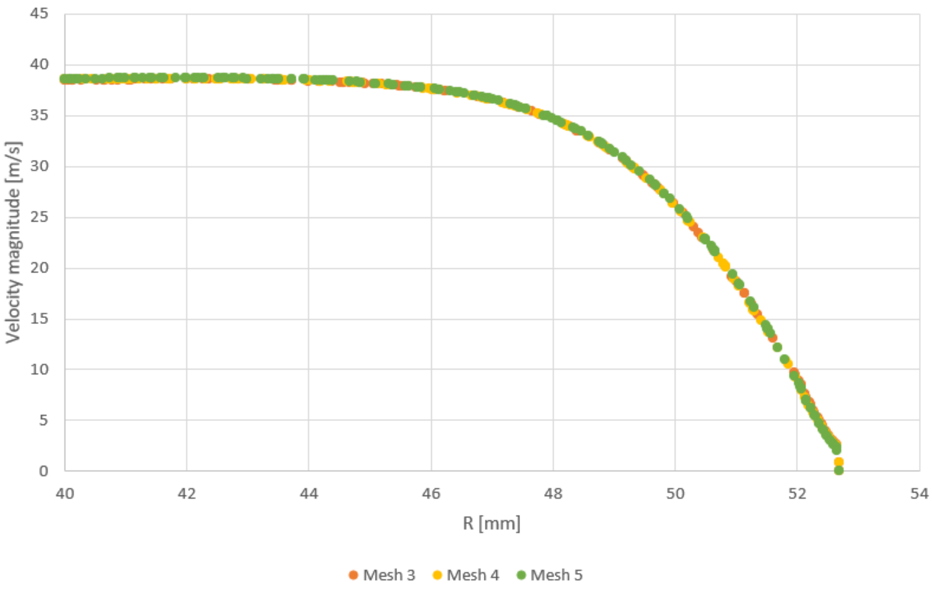

Figure 3.10: A comparison of the velocity magnitude profile along the domain symmetry axis, from nozzle outlet to sample surface.

In addition to the static pressure, also the velocity magnitude along the axis of symmetry, from the nozzle to the sample, was monitored and no significant differences were detected for the three finest meshes, as it can be seen from the plot in Figure 3.10. Consequently, mesh 4, having 3 million elements (see Table 3.3), was selected.

3.2.5. Simulation results

Computing the flow velocity and pressure fields is the first step towards the calibration of an erosion model, according to the SAER method. The results of the single-phase simulation are reported in Figures 3.11-3.12. The operating fluid was water at 25° at atmospheric pressure. Details on water heating during the laboratory experiments can be found in [1].

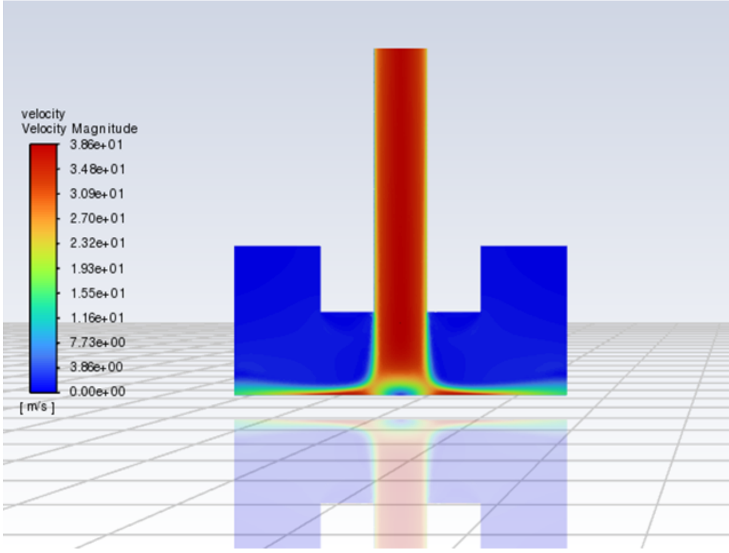

Figure 3.11: Velocity magnitude contour on the mid-plane.

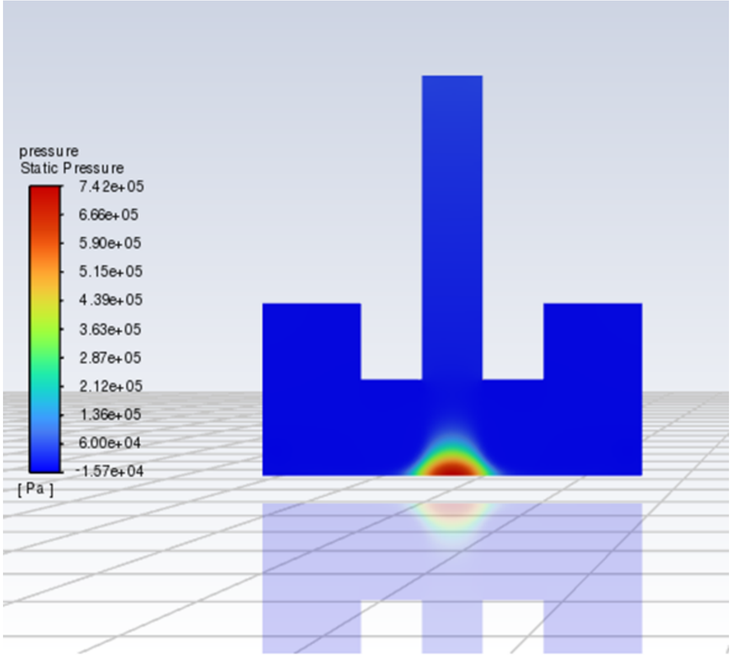

Figure 3.12: Static pressure contour on the mid-plane.

Fig. 3.11 clearly shows how the fluid flow is substantially undisturbed until it nears the sample wall, where a sudden shift in its dynamics occurs. In the central region, the flow velocity drops drastically, as the jet is deflected radially, away from the sample center. As depicted in Fig. 3.12, the static pressure is constant everywhere except for a region where it peaks, in front of the nozzle exit. This high-pressure, low-velocity area is usually called "stagnation zone". Here, the velocity is very low and so the erosion damage is expected to be less severe. Hence, the typical W-shaped profile observed in wet direct impact tests [47],[14].

3.3. Calculation of the trajectories of the abrasives

Once the single-phase flow simulation has been performed, one can proceed with the introduction of the dispersed phase. As previously mentioned, the one-way coupling regime requires to solve the flow first, then compute each parcel's trajectory. In this work, the parcel approach was used, meaning that a computational particle corresponds to a set of physical particles and so less trajectories have to be computed. As a consequence, the total computational cost is sensibly lower and affordable. In Ansys Fluent 2022, particle tracking can be performed via the Discrete Phase Model (DPM). This model requires the initial position and velocity of each parcel, in addition to the mass flow rate, and tracks them for a given number of computational steps. Glass beads particles having 90 μm diameter and 2500 kg/m^3 density were injected from the inlet boundary, extracting their position from a uniform probability distribution function. Their initial velocity was set to be equal to that of the inlet flow in the corresponding positions. The mass flow associated to each particle, $\dot{m}_p$, can be estimated through Eq. 2.22

$$\dot{m}_p = \frac{\pi D^2 V_{jet} \hat{c}}{4N_p} \tag{2.22}$$

where V_{jet} is the flow jet velocity, $\hat{c}$ the particle concentration and N_p the number of particles injected.

The DPM allows for the introduction of various forces acting on the particles. The virtual mass force (with a 0.5 coefficient for spherical particles, Eq. 2.16), the pressure gradient force, gravity and buoyancy were set directly in the model panel. Conversely, the lift force from Mei et al. [65], Eq.2.17, was introduced via a user-defined function (UDF). The drag was enabled in the injection panel, where the particle shape was set as spherical for glass beads and the discrete random walk model was switched on to take into account the effect of particle turbulent dispersion. The tracking scheme and the number of tracked steps were kept default. The default number of tracked steps in a steady setting is 50000, enough for each particle to escape the domain.

After impacting, particles should be reflected off the sample surface following a rebound law, as proposed by Forder et al. [68], Eqs. 2.20-2.21. This was easily achieved by imposing a polynomial law for particle reflection in the DPM panel for the sample surface, Fig. 3.8b. The boundary conditions on the nozzle walls, Fig. 3.8a, were kept as *reflect* with unitary coefficients, meaning that a complete reflection is achieved, while the *escape* condition was default on virtual boundaries, Fig. 3.7.

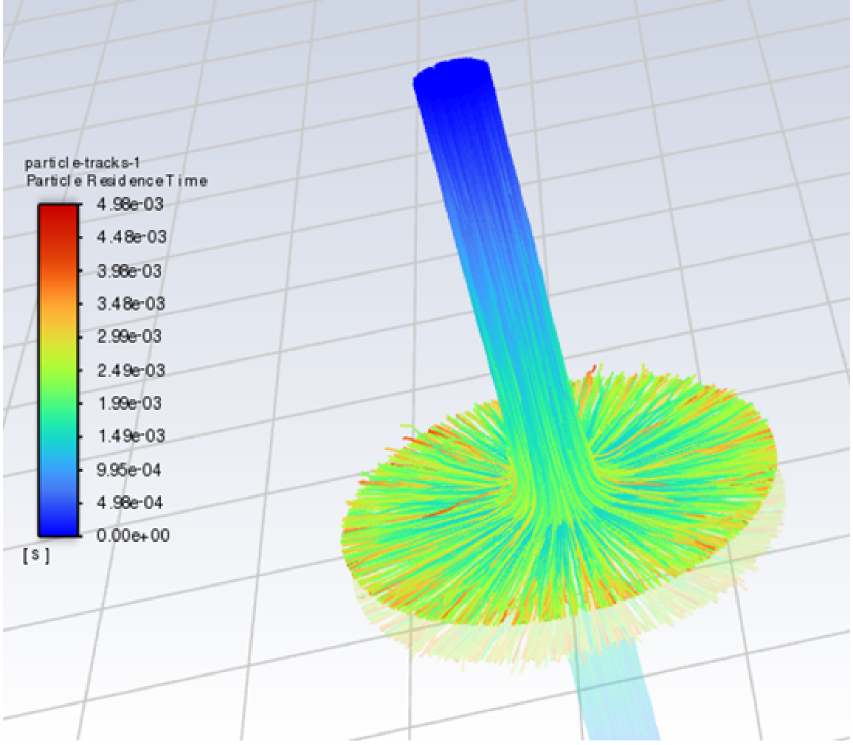

Figure 3.13: Particles trajectories coloured based on their residence time.

Figure 3.13 shows representative particle trajectories colored by the particle residence time, that quantifies how much time a particle spends in a certain region. The tracked particles quickly move away from the nozzle outlet and are progressively slowed down while reaching the specimen surface.

After tracking down each particle, its velocity components at the stage of impact on the sample surface were stored as output.

The number of parcels has to be chosen carefully by the user. This calls for a sensitivity study, which should prove that the particles impact statistics are substantially independent on their number. This is detailed in section 3.5.1. At the end of the study, the selected value was 50000 parcels.

3.4. Application of SAER in ring-based formulation

Once the CFD simulation has been carried out, the flow dynamics captured and the particles' motion tracked, the SAER approach requires to post-process the information on the particle-wall collisions. Sec. 3.4.1 is about the impact statistics determination, while Sec. 3.4.2 details how a selected erosion model can be calibrated on the numerical data. Finally, Sec. 3.4.3 revolves around the application of the newfound formula to erosion prediction in cases 5, 12 and 20.

3.4.1. Calculation of the particle-wall impact statistics

The impact velocity magnitude, $v_{p,imp}$, and impact angle, $\theta_{p,imp}$, of each particle-wall impingement were post-processed by applying the SAER ring-based method.

The circular sample was divided in concentric rings, with inner radius R_i and outer radius $R_{i+1} = R_i + dR$ with $(i = 1, ..., N_{rings} - 1)$, dR being the radius increment. The *variable* dR approach, proposed by Wang in [1] was followed. This implies that a fixed number of impacts happening in each annulus was selected and the value of dR was adjusted accordingly. This treatment was deemed more physically sound than the *constant* dR one, which considers rings of constant size. The number of rings was set to $N_{rings} = 20$. See Sections 3.5.2 and 3.5.3 for further discussion on this issue.

Figures 3.14-3.16 show the radial dependence of the impact statistics, since the very nature of the ring-based method allows for a one-dimensional analysis. Focusing on the impingement of each particle, it seems relevant to operate a distinction between primary and secondary impacts. A particle will be injected with a similar velocity to that of the flow around it at the inlet; then, it will follow the fluid flow towards the sample. Close to the sample surface, the boundary layer will slow down the flow velocity, while the particle, having a higher density, will be driven by inertia to collide with the specimen. After the first, primary, impact, it will rebound, according to the imposed restitution law, only to be dragged back to the sample by the incoming flow, generating secondary impacts. Arguably, primary impacts play a significant role in the erosion phenomenon, since they involve higher kinetic energy. However, also secondary impacts have to be taken into account for an accurate numerical simulation. Thus, the plotted data refer to primary and secondary impingements. In Figs. 3.14-3.15 the trend of the ring-averaged impact velocity and ring-averaged impact angle with respect to the distance from the sample center is reported. The ring-averaged impact velocity shows an increasing trend: it is smaller in the first, inner rings (stagnation zone), while reaching higher values in the periphery. The ring-averaged impact angle is a decreasing function of the radial coordinate. The slight

increase in the innermost region is likely to be caused by secondary impacts, which involve a broader range of angles, thus lowering the mean value for the first ring.
Conversely, Figure 3.16 shows the radial profile of the impact number density, i.e. number of impingements per unit area, which clearly shows that the majority of impacts happen within a 10 mm radius. This is why the R range has been limited to 10 mm in all the figures.

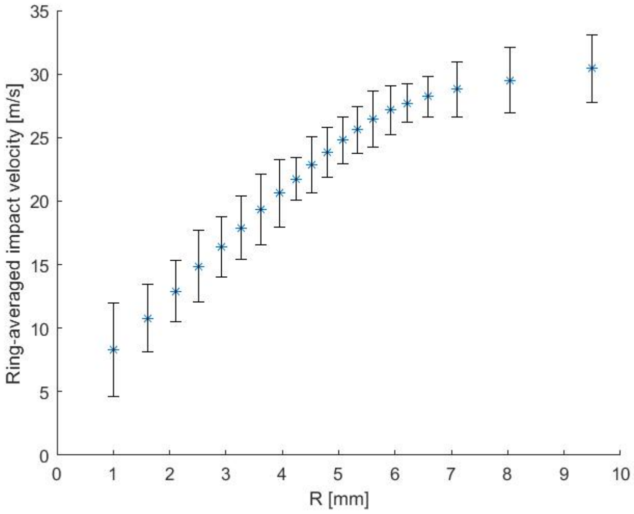

Figure 3.14: Ring-averaged impact velocity with standard deviation error bars.

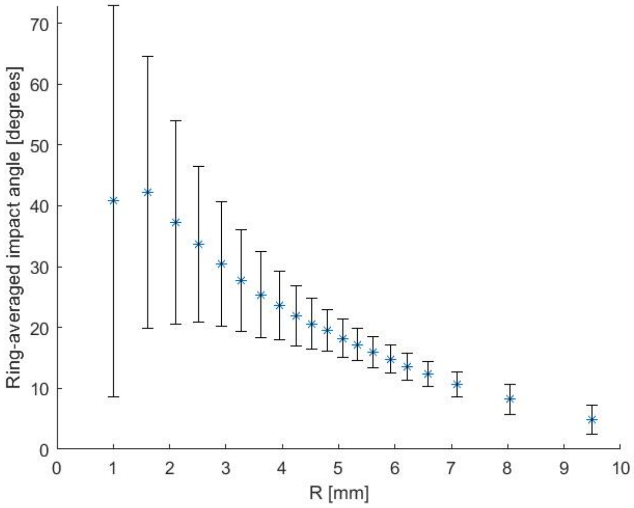

Figure 3.15: Ring-averaged impact angle with standard deviation error bars.

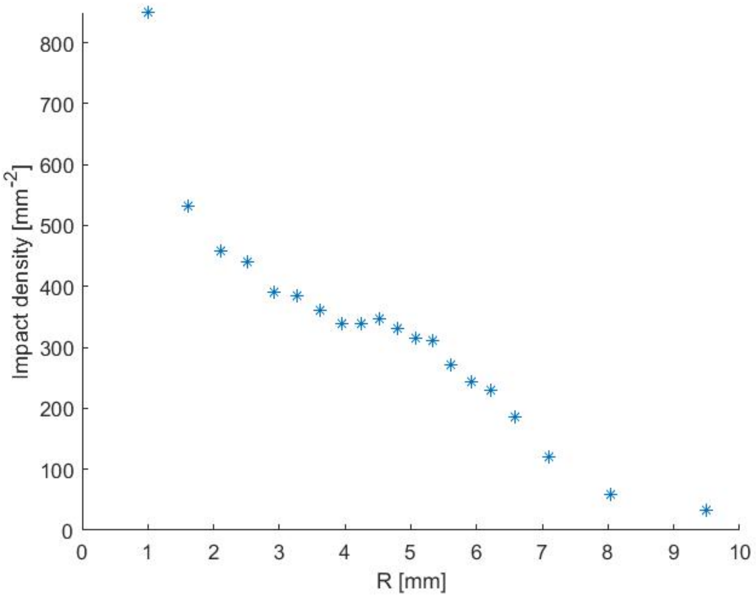

Figure 3.16: Impact density, i.e. number of impacts per unit area.

The fixed number of impacts per annulus was selected, accordingly, by dividing the total number of impingements within a 10 mm radius by N_{rings}.

Figure 3.17 shows the mean radius of each annulus and its corresponding erosion depth. Moreover, the SAER locations, namely the erosion depth values corresponding to the radius associated to each ring, are encircled. The erosion profile has a peak around $R = 5\,mm$.

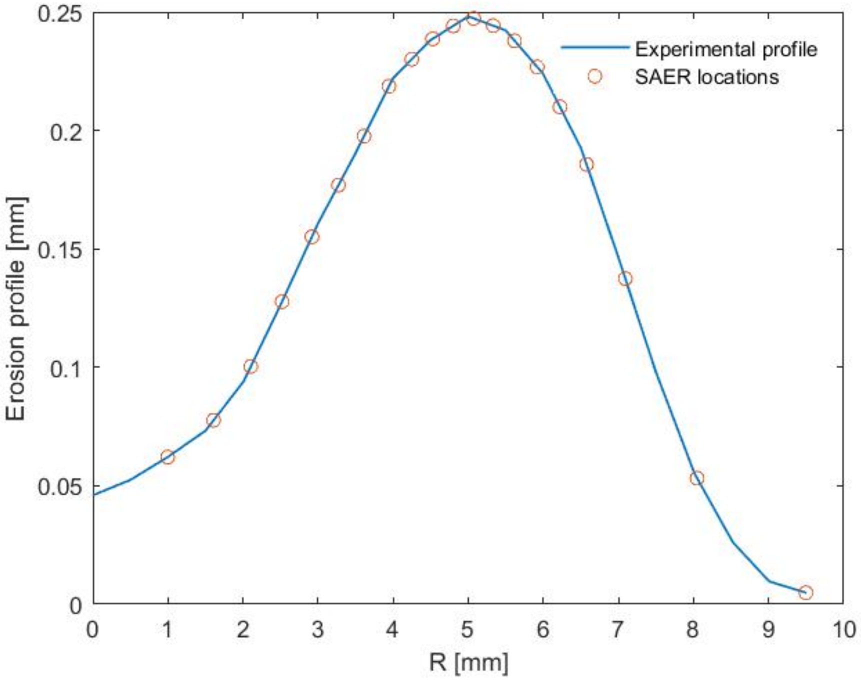

Figure 3.17: Experimental erosion profile of case 1 and SAER locations.

Once the impact statistics are known, the SAER procedure proposes a way to find the a suitable impact angle function. This is what the Section 3.4.2 is about.

3.4.2. Determination of the erosion model

As explained in Section 2.4, the eroded depth in the i-th ring, h_i, can be expressed as

$$h_i = \frac{\dot{m}_p\, t\, \sum_{j=1}^{N_{imp@i}} F(\mathbf{v}_{P,imp@i,j}, \theta_{P,imp@i,j}, etc.)}{\rho_t\, S_i} \tag{3.1}$$

The SAER approach requires to reverse-engineer the problem. In each ring, h_i can be interpolated on the experimental erosion profile, while the CFD simulation yields the velocity magnitude of each particle j impacting inside ring i, $v_{N_{imp@i,j}}$, the inclination of the impact, $\theta_{N_{imp@i,j}}$ and the ring area $S_i = \pi\,(R_{i+1}^2 - R_i^2)$. The total number of impingements happening inside the i-th ring, in the *variable dR* approach, is chosen by the user, i.e. $N_{imp@i} = N_{imp}\ \forall i$.

The only unknown in Eq. 3.1 is the function F, describing how the erosion produced by the individual particle-wall impacts is affected by the impact velocity, the impact angle, and possible other relevant parameters. The SAER approach is aimed at finding a suitable

model for this function and determine its coefficients.
First, to simplify the mathematical structure, the impact velocity and the impact angle are assumed to be two independent variables. This is grounded in experimental evidence from D-DITs [70]. Secondly, the dependence on other physical parameters is assumed to be of minor importance and accounted for in a multiplicative coefficient K.
Therefore, the function F takes the following form:

$$F(v_{P,imp}, \theta_{P,imp}, etc.) = K\ g(v_{P,imp})\ f(\theta_{P,imp}) \tag{3.2}$$

The function $g(v_{P,imp})$, that is the link between impact velocity and erosion, is often modelled as an exponential [64] (Eq 3.3)

$$g(v_{P,imp}) = v_{P,imp}^n \tag{3.3}$$

nevertheless, different models may be found more suitable (see [15] and Section 4.2).
In Oka et al. [70], the experimental evidence suggests that $n = 2.1$ should be a good choice for the velocity exponent in the case of glass beads impinging on an aluminium sample. This value will be used throughout this chapter, but its choice will be questioned in Section 4.1.
As for the impact angle function $f(\theta_{P,imp})$, describing the link between the impact angle and erosion, a variety of models have been proposed in the last years. Some of the most widely used are those by Oka et al. [46], Zhang et al. [58] and Finnie et al. [21]. In this work, the Oka model [46] reported in Eq. 3.4 has been selected.

$$K\ f(\theta_{P,imp}) = a\ (sin(\theta_{P,imp}))^b\ (1 + H_v\ (1 - sin(\theta_{P,imp})))^c \tag{3.4}$$

where H_v is the Vicker's hardness of the target material, and a, b, c are three coefficients characterizing the shape of the impact angle function. In Eq. 3.4, the cutting mechanism is described by the term $(sin(\theta_{P,imp}))^b$, while $(1+H_v\,(1-sin(\theta_{P,imp})))^c$ accounts for plastic behaviour. This interpretation of the erosion dynamics has been introduced in Section 1.3.1 and will be further discussed in Section 4.1.2, as it is crucial to assess the accordance of the calibrated equation with the physical modelling intuition.
The prediction on the product $K\ f(\theta_{P,imp})$ is given by Eq. 2.28

$$K\ f(\bar{\theta}_i) = \frac{\rho_t\ S_i\ h_i}{N_p\ \dot{m}_p\ t\ \bar{v}_{p,i}^n} \tag{2.28}$$

At this point, a, b and c have to be estimated. This is done by optimizing their value in a fitting session, comparing Eq. 2.28 to Eq. 3.4 The fitting session was performed in the Matlab Curve Fitting toolbox. The Non-linear Least Square (NLS) algorithm, in combination with a Trust-Region approach, and the Bisquare method for robustness, was utilized. The residual threshold and the minimal increment were set to 10^{-12}, the maximum number of iterations was set to 40000.

The accuracy of this procedure, with respect to applying more general models from the literature, has been thoroughly explored in [1]. SAER provides much better erosion predictions, even though it reduces the range of applicability of the found equation.

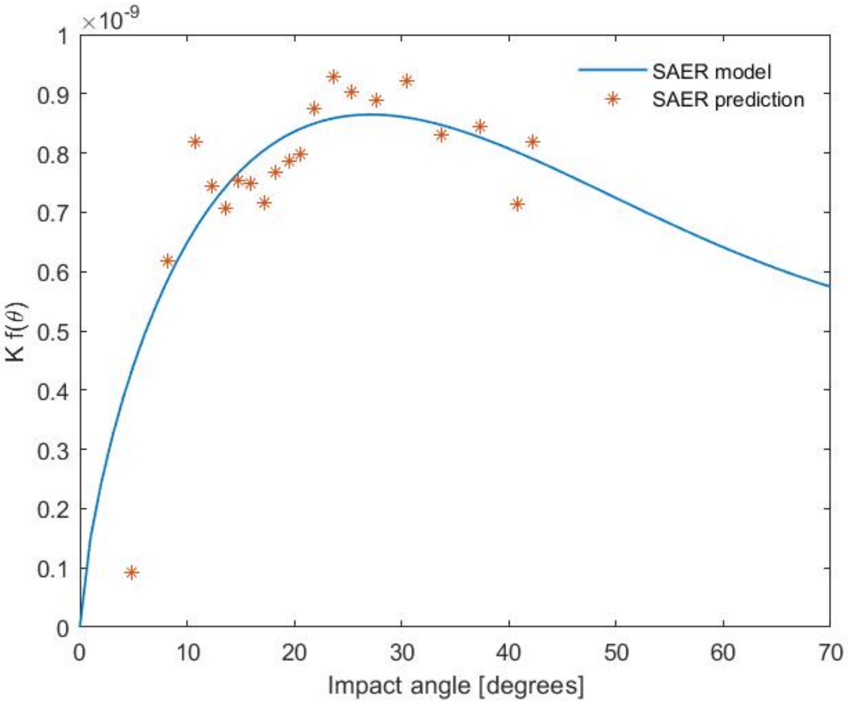

Figure 3.18: Impact angle function: data versus fitted model.

Here, the results for the fitting of the Oka model are presented (Table 3.4, Eq. 3.5).

a	b	c	R^2
$5.183 \cdot 10^{-10}$	0.7204	2.298	0.78

Table 3.4: Calibrated coefficients.

$$K\ f(\theta_{P,imp}) = 5.183\,10^{-10}\,(sin(\theta_{P,imp}))^{0.7204}\,(1 + H_v\,(1 - sin(\theta_{P,imp})))^{2.298} \tag{3.5}$$

Figure 3.18 shows the scattered data obtained by combining the CFD and the experimental results and the impact angle function obtained from the regression. The erosion is maximum at impact angles around $25 - 30°$, in accordance with the commonly used impact angle functions, such as Eqs. 1.3-1.7.

Figure 3.19 compares the experimental profile to the prediction of the calibrated equation. The coefficients have been optimized to reproduce the experimental data, therefore the similarity between the numerical and measured erosion profiles is not surprising. A more relevant and challenging study can be found in Sec. 3.4.3, where the predictive ability of the erosion formula is tested outside its range of calibration.

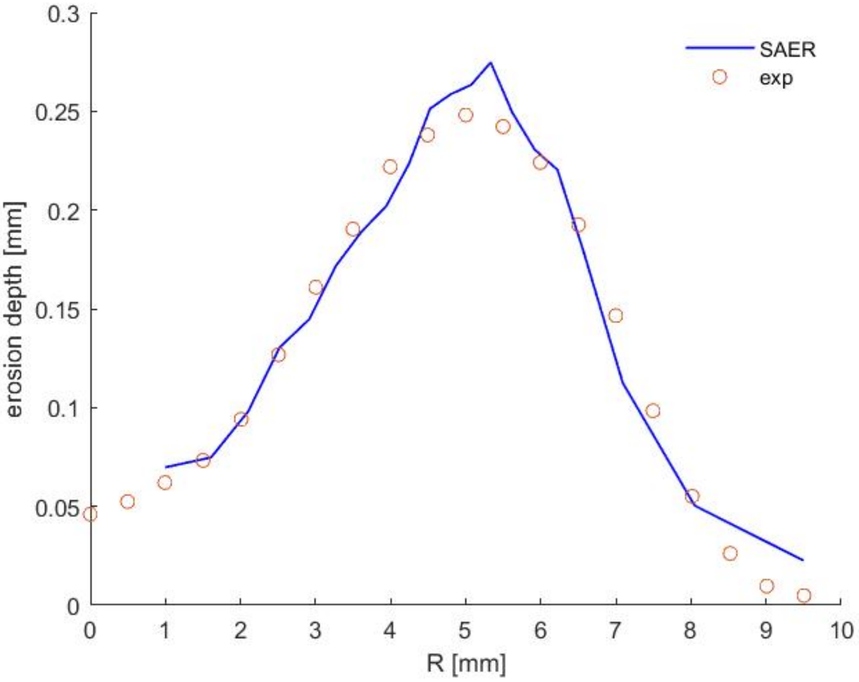

Figure 3.19: Erosion prediction and measured profile.

3.4.3. Verification of the calibrated formula

The experimental results of case 1 [1], involving glass beads with a $90\,\mu m$ diameter, have been exploited to calibrate the erosion formula (Eq. 3.5). As previously anticipated, cases 5, 12 and 20 from [1] have been used to test the goodness of the calibrated model outside of the calibration range, as the particles employed in these tests had a $120\,\mu m$, $250\,\mu m$ and $350\,\mu m$ diameter, respectively. The operating conditions of the four tests are summarized in Table 3.1.

A different particle diameter clearly leads to different impact statistics, since doubling the diameter brings about an eight-fold increase of mass. The ring-based approach was used for each of the described test cases and the erosion profile predicted by the SAER procedure are reported in the following Figures 3.20, 3.21, 3.22, comparing them with the in-situ measured profile.

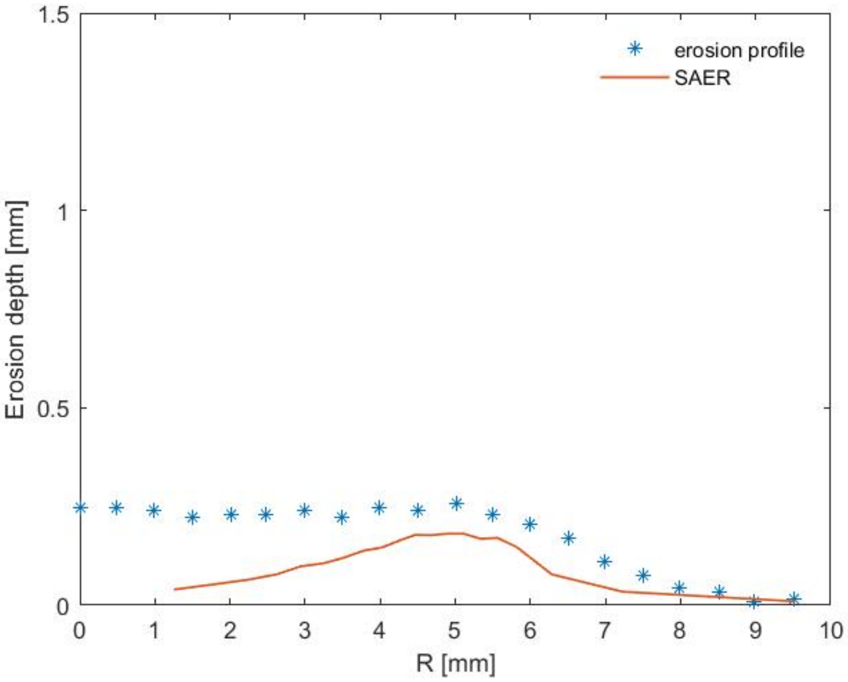

Figure 3.20: SAER performance in case 5 ($d = 120\mu m$).

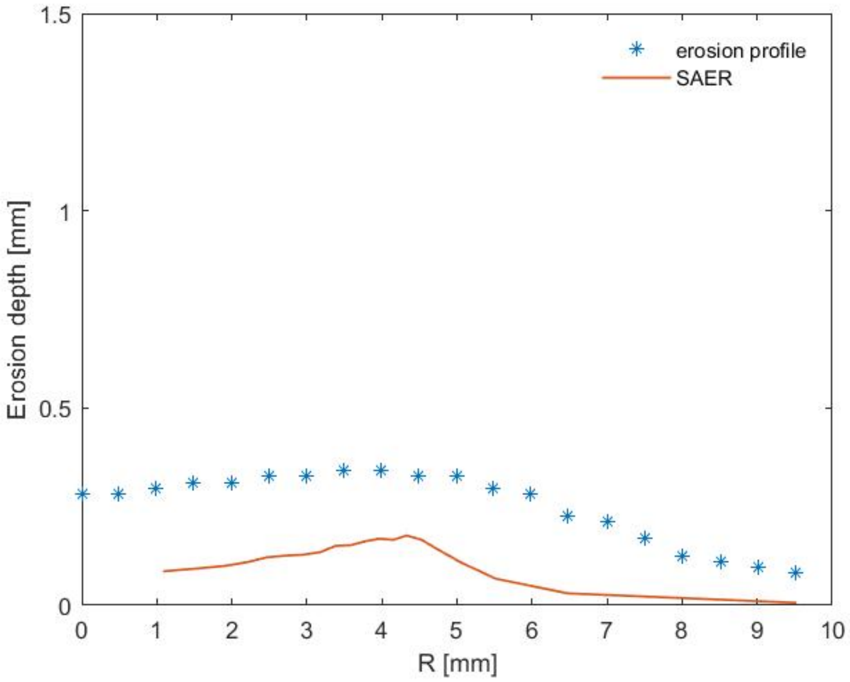

Figure 3.21: SAER performance in case 12 ($d = 250\mu m$).

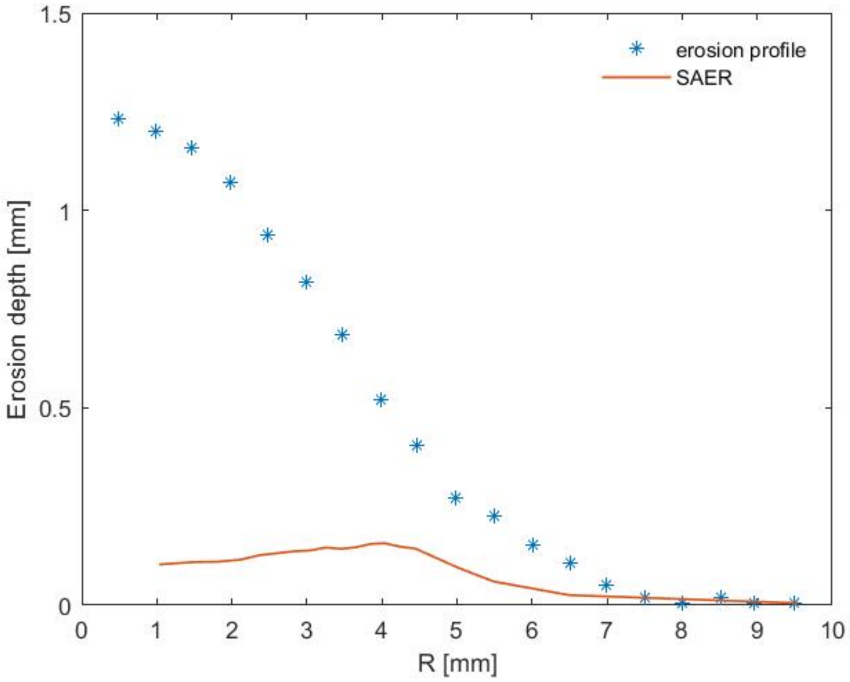

Figure 3.22: SAER performance in case 20 ($d = 350\mu m$).

As it can be seen in Figure 3.20, in case 5, where the diameter is close to that of case

1, a good prediction of the location and depth of the erosion peak can be found, while the model performs less accurately in the innermost part. The predicted profiles in cases 12, Fig. 3.21, has a comparable shape to the experimental one, but it underestimates the erosion depth. To conclude, the predictive accuracy of calibrated formula in case 20 is poor, as shown in Fig. 3.22, thus leaving room to further refinements of this procedure. A discussion on ways to improve the SAER approach can be found in the Chapter 4.

3.5. Sensitivity analyses

In CFD analysis, whenever the user makes a choice, the simulation results are affected. A sensitivity (or independence) analysis is due, in these cases, in order to assert that no significant changes stem from it.

This final section of this chapter is dedicated to the main sensitivity studies performed on the CFD simulation used so far to model the erosion phenomenon in case 1.

3.5.1. Effect of the number of parcels

First, since there is no way to calculate exactly how many particles impact on the sample in the laboratory experience, the user has to fix a number of particles/parcels to be injected. Then, each particle is associated a mass flow rate estimated as in Eq. 2.22.

Figures 3.23 - 3.25 show the resulting impact statistics in terms of ring-averaged impact velocity, impact angle and impact density for different numbers of particles N_p.

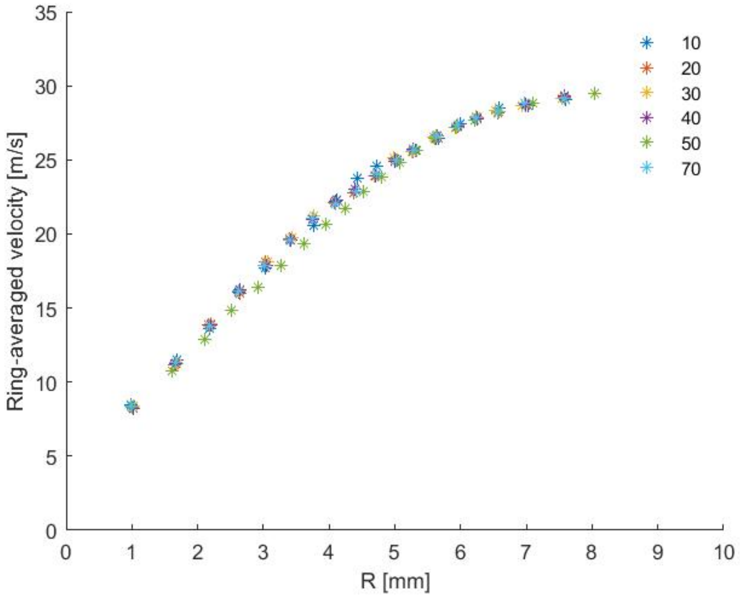

Figure 3.23: Ring-averaged impact velocity comparison for different number of injected particles.

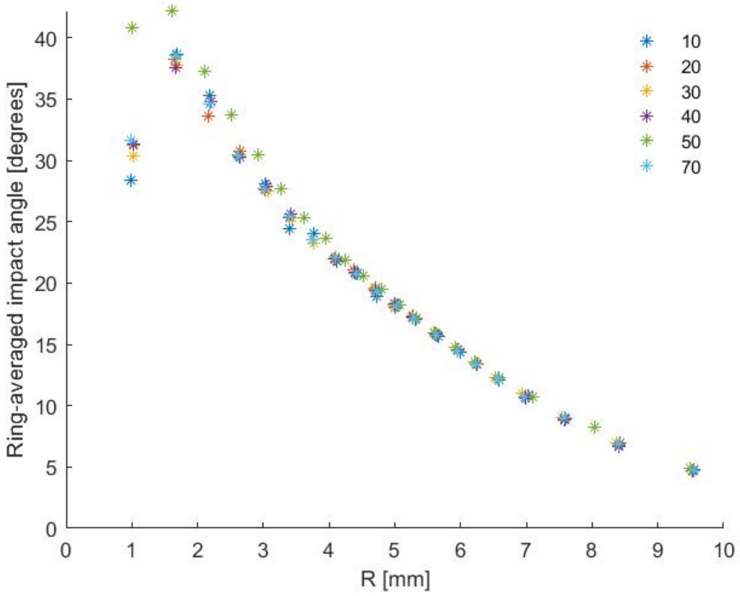

Figure 3.24: Ring-averaged impact angle comparison for different number of injected particles.

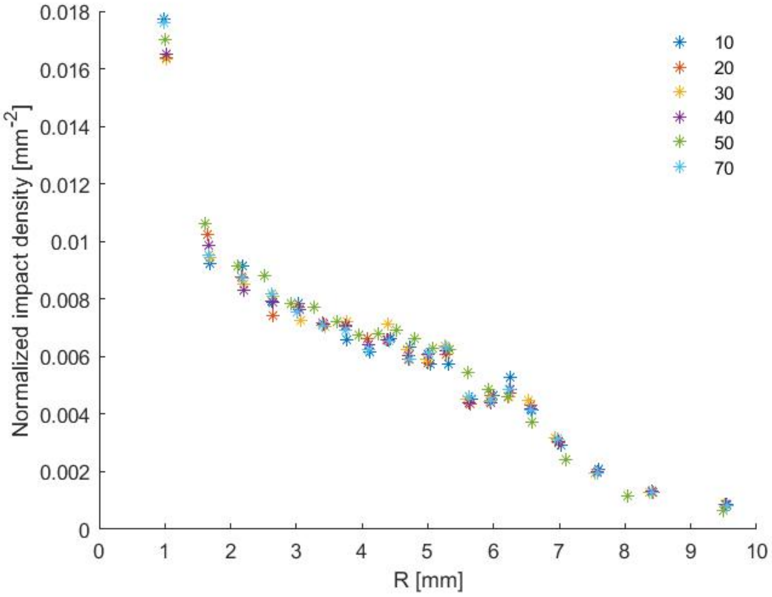

Figure 3.25: Impact density comparison for different number of injected particles (normalized with respect to the number of particles).

The number of parcels has been varied from 10000 to 70000. The impact statistics do not show significant changes. Consequently, the computation of the trajectories described in section 3.3 was carried out injecting 50000 particles to have good confidence in the averaged quantities.

3.5.2. Effect of the number of rings

As previously explained, in the case of axis-symmetrical domains, the ring-based method of the SAER procedure requires to split the sample surface into concentric rings. The choice of how many annuli to create is arbitrary and needs to be guided by common sense or physical considerations. Taking this to the extreme cases: if too few rings are used, there will be few points to calibrate the erosion model. Choosing an excessive number of rings, instead, will yield less confidence in the impact statistics, since each point will result from averaging a smaller number of impacts.
Figures 3.26, 3.27 and 3.28 report the results of the sensitivity analysis with respect to the chosen number of rings.

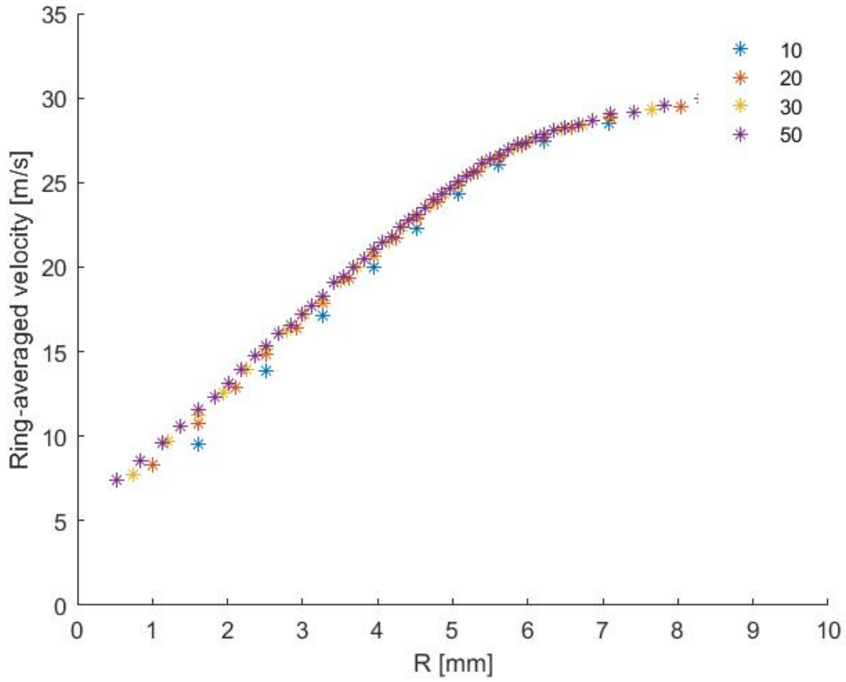

Figure 3.26: Ring-averaged impact velocity comparison for different number of rings considered.

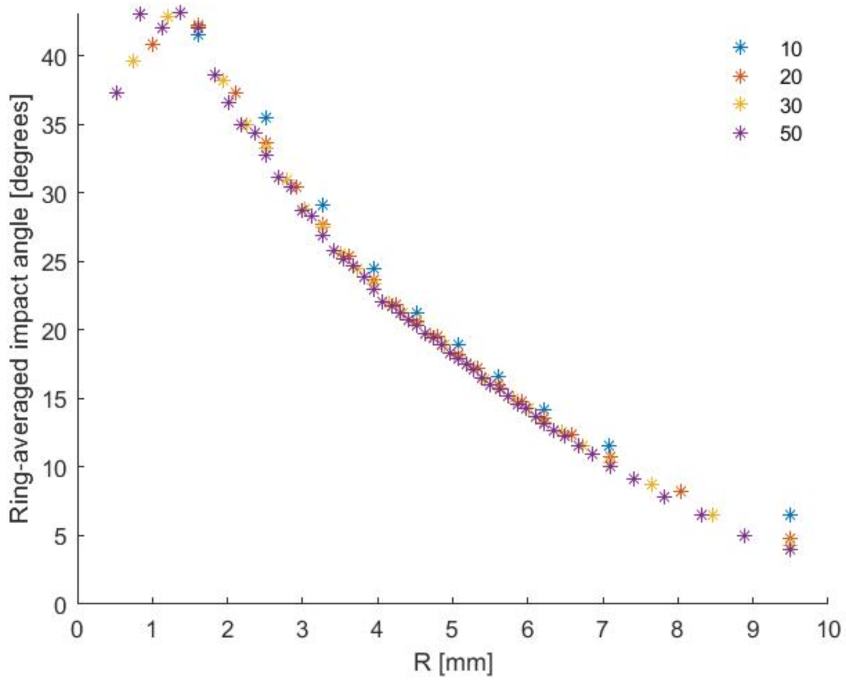

Figure 3.27: Ring-averaged impact angle comparison for different number of rings considered.

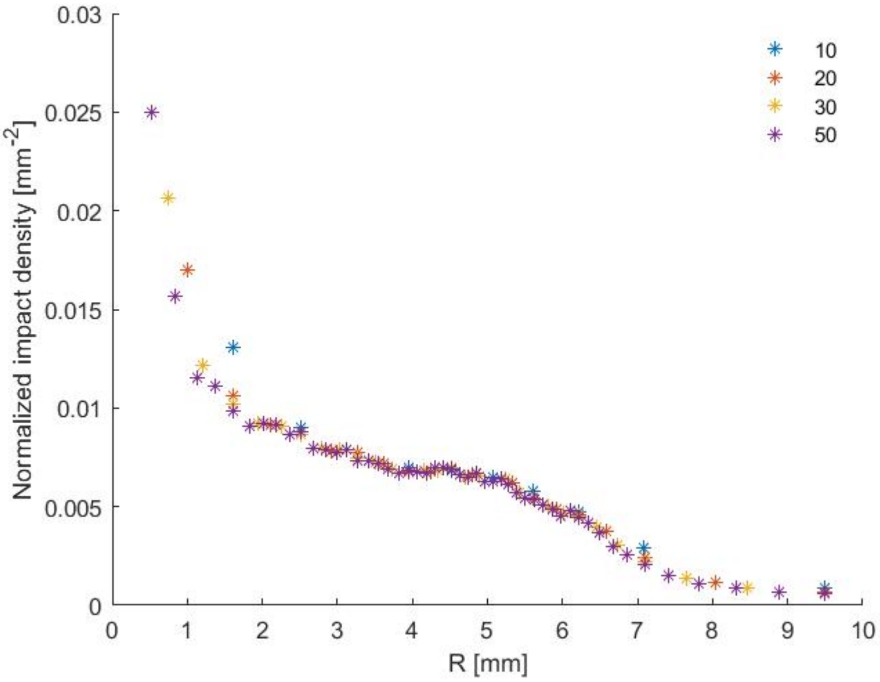

Figure 3.28: Normalized impact density comparison for different number of rings considered.

The number of rings has been varied from 10 to 50. The impact statistics resulting from calculations made on more than 20 rings seem to remain unchanged.
The computation was, therefore, carried out creating 20 rings, for consistency with the experimental data, which provided that same number of points for the erosion profile.

3.5.3. Constant versus variable ring thickness

When splitting the sample surface in concentric rings, one could choose to use a constant value for dR or to fix a number of impacts for each region and discretize accordingly.
The first approach is more direct, but blunt, as it does not account for the physics and could lead to averaging data in an inconsistent way. The second one is a little more involved. It may result in a largely dishomogeneous distribution of data, since the majority of impacts occurs up to 6 mm.
Figures 3.29, 3.30 and 3.31 show the three main impact statistics in the two cases, injecting 50000 particles as detailed in Section 3.3.

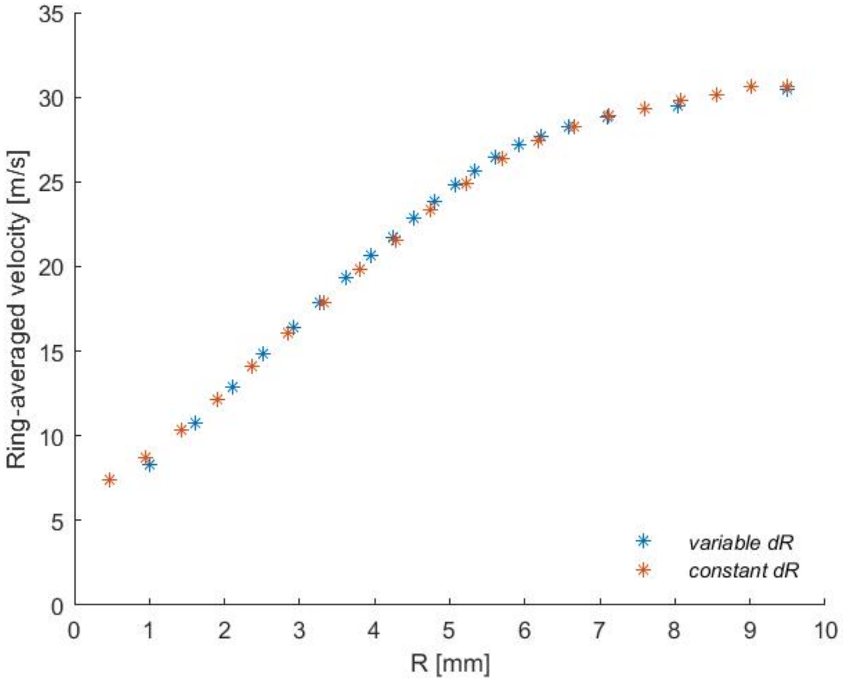

Figure 3.29: Ring-averaged impact velocity comparison for *constant* or *variable dR*.

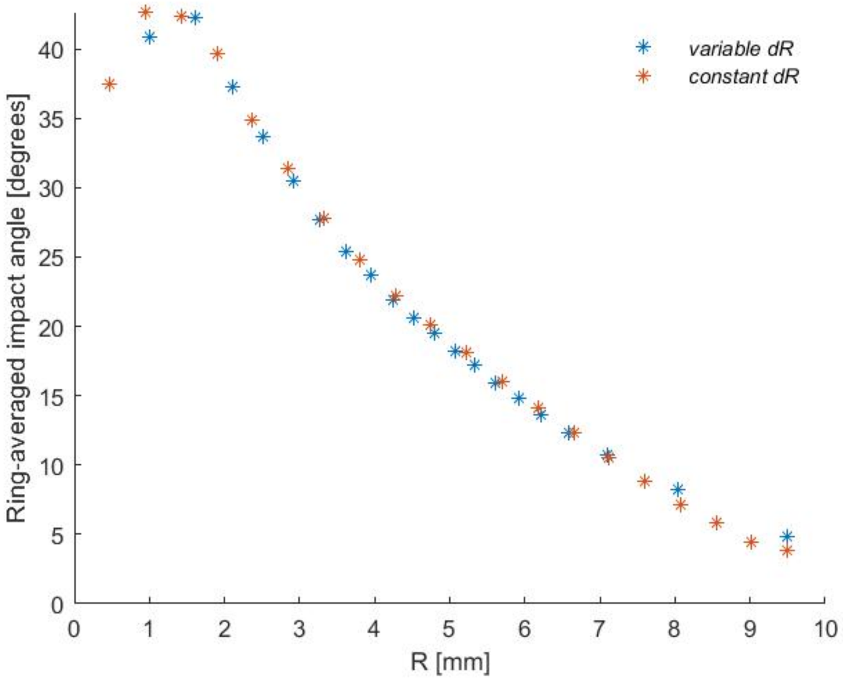

Figure 3.30: Ring-averaged impact angle comparison for *constant* or *variable dR*.

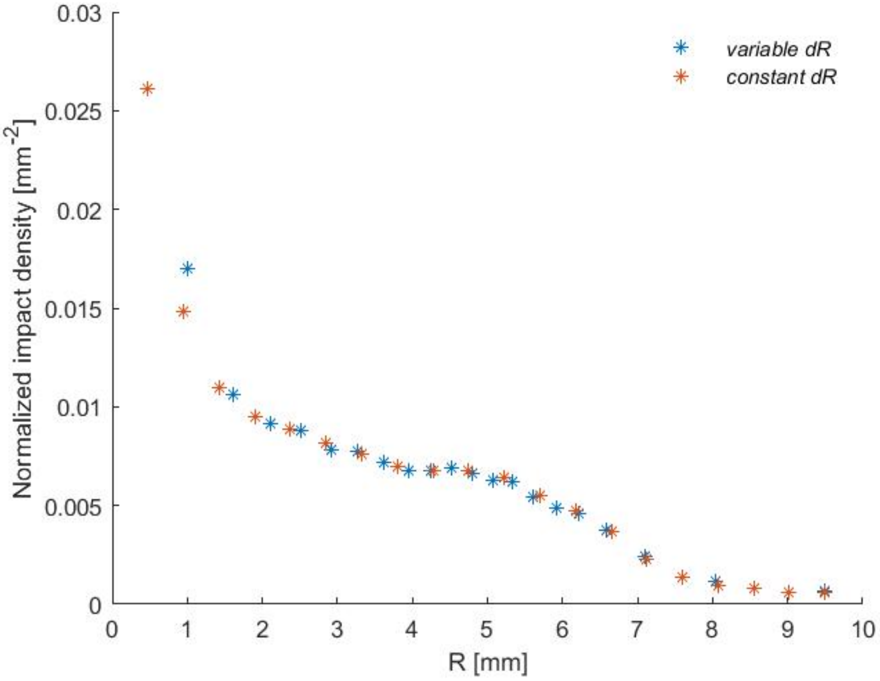

Figure 3.31: Normalized impact density comparison for *constant* or *variable dR*.

The impact statistics show little differences. The *constant dR* approach provides evenly spaced points, covering all the considered range, including the region closest to the sample center. The information provided by *variable dR* approach, instead, is clustered in the region when impacts are more frequent.

Although it would be very convenient to work on evenly spaced data, the *variable dR* approach seems much more physically sound, focusing on the part of the domain where the erosion modelling is actually more relevant. Therefore, as suggested in Wang [1], this approach was selected in this thesis.

4 | Extension of the SAER procedure

The results reported in Chapter 3 show how to apply the SAER approach in a combined experimental-numerical effort to calibrate an erosion model. Impact statistics obtained from CFD analysis and in-situ measurements of the test-case erosion profile have been used to optimize the coefficients.

The found equation, ideally, is expected to express the correlation between impact angle and erosion scar for any slurry made of glass beads and water impacting on an aluminium sample. This is not the case, as shown in Figures 3.21 and 3.22, where the erosion prediction capacity of the model drops significantly when the particle diameter is considerably different from the value of the test used for calibration. Clearly, there is room for improving the procedure.

The present chapter is aimed at detailing the study conducted on possible ways to make the calibration process more accurate. In particular, the goal is to make it possible to use this approach even in absence of D-DIT or any other clue on the velocity exponent. Actually, the exponential model for the impact velocity function is questionable and it seems reasonable to investigate on different possible ways to describe the relationship between velocity and erosion.

First, in Section 4.1, the inclusion of the velocity exponent n in the set of fitted parameters is discussed. This would imply reducing the laboratory data needed for the application of the approach described in Chapter 3, which requires some D-DIT to provide a suitable value for n.

Secondly, the velocity function model is questioned in Section 4.2. An exponential relation has been chosen in the previous chapter for its simple structure and to be consistent with the choice made in a wide range of studies ([46], [21], [58] and many more). A different function, as in Lester et al. [15], is selected and the resulting fitting process is discussed.

4.1. Inclusion of the velocity exponent among the calibration parameters

The calculations in Chapter 3 were based on the assumption that the value $n = 2.1$ for the velocity exponent could be suitable to model the exponential relation between impact velocity and erosion depth expressed in Eq 3.3. This value has been proposed by Oka et al. [70], upon analysis of various dry direct impact tests involving glass beads and an aluminium sample. D-DITs are often used to characterize functional relations in erosion modelling, but coefficients obtained via this kind of test are widely out of range if applied to W-DITs. Therefore, the question arises naturally as to how to improve the estimation of the velocity exponent n. In this section, the inclusion of the velocity exponent in the fitting process is discussed.

$$K\, f(\bar{\theta}_i) = \frac{\rho_t\, S_i\, h_i}{N_p\, \dot{m}_p\, t\, \bar{v}_{p,i}^{n}} \tag{2.28}$$

$$K\, f(\bar{\theta}_i)\, \bar{v}_{p,i}^{n} = \frac{\rho_t\, S_i\, h_i}{N_p\, \dot{m}_p\, t} \tag{4.1}$$

The implementation of this extension to the SAER procedure is quite straightforward. Eq. 2.28 was used in Chapter 3 to estimate the product $K\, f(\bar{\theta}_i)$. Here, Eq. 4.1 has been employed to include the velocity coefficient n among the calibrated parameters. The Oka model, Eq. 1.7, and a power law, like Eq. 3.3, have been selected for the impact angle and impact velocity dependence, respectively.

At least two possible sets of parameters reported in Table 4.1 have been found suitable, meaning that the associated R^2 value was high enough to deem the resulting model representative of the fitted data. Set 1 was found in a fitting session that only allowed for positive values of the four coefficients. This set shows really close values to those reported in Chapter 3, so it is not surprising that it does not noticeably improve the erosion prediction. On the other hand, obtaining a value for n similar to the one suggested by Oka et al. ([70]) for the combination glass beads/aluminium upholds the validity of that proposal.

An interesting behaviour was observed using a second set of coefficients (set 2), that was found to be optimal in a fitting session that allowed for negative coefficients. The values of the impact angle function (a, b, c) are far from those reported in the literature, in particular, coefficient c is negative, while the velocity exponent n is much larger than 2.1. This implies than the found equation shows non-physical features, which will be discussed in Section 4.1.2. Nevertheless, the erosion prediction performance seems to get much better, as shown in Section 4.1.2.

Set 3 in Table 4.1 reports the values of the coefficients found in Chapter 3, while assuming $n = 2.1$, as suggested by Oka et al. [70].

	a	b	c	n	R^2
set 1	$1.791 \cdot 10^{-10}$	0.8093	2.701	2.391	0.86
set 2	$3.184 \cdot 10^{-11}$	0.61	-1.236	3.55	0.83
set 3	$5.183 \cdot 10^{-10}$	0.7204	2.298	2.1	0.78

Table 4.1: Fitting coefficients.

4.1.1. Validation using the first set of coefficients

Fig. 4.1 shows the erosion profile of case 1, used in the calibration phase. Both the SAER method described in Chapter 3 and its extension, that includes the velocity exponent, accurately reproduce the experimental data. This is not surprising, as the coefficients were optimized to this aim.

Figs. 4.2 - 4.4 show the erosion prediction for cases 5, 12, 20 given by the extended SAER method, using the first set of coefficients (set 1 in Table 4.1

The value of n resulting from the fitting process is very close to the reference one ($n = 2.1$) proposed by Oka et al. [70]. This implies that assuming that a coefficient obtained from D-DIT studies could be suitable also for W-DITs, as in Oka et al. [70], is reasonable. Consequently, the erosion predictions are not significantly affected by the new values of the coefficients. For all particle diameters, the curves obtained with the new sets of coefficients (in red) is very close to those found with the set of coefficients determined in Chapter 3 (in yellow).

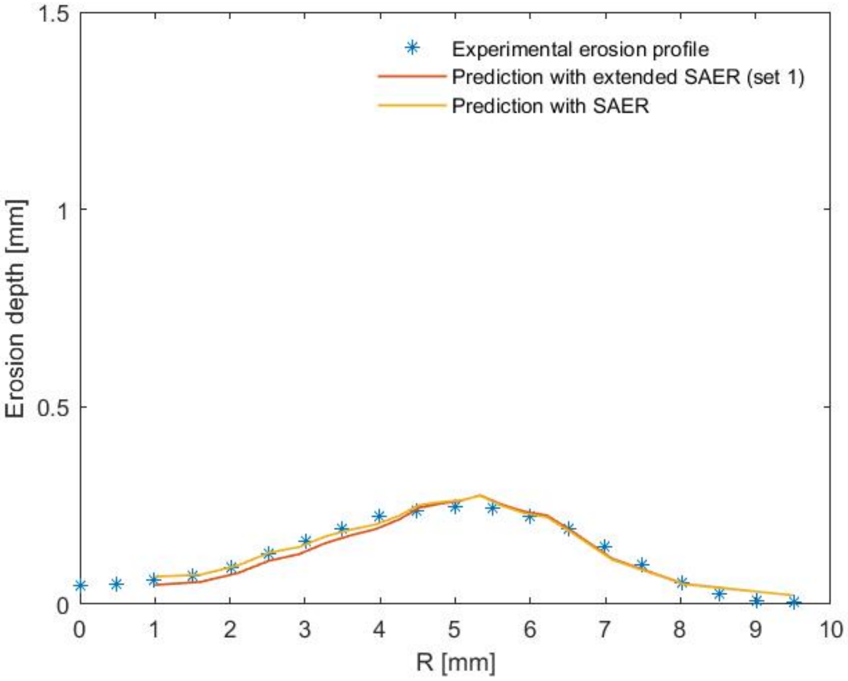

Figure 4.1: Extended SAER performance in case 1 ($d = 90\mu m$).

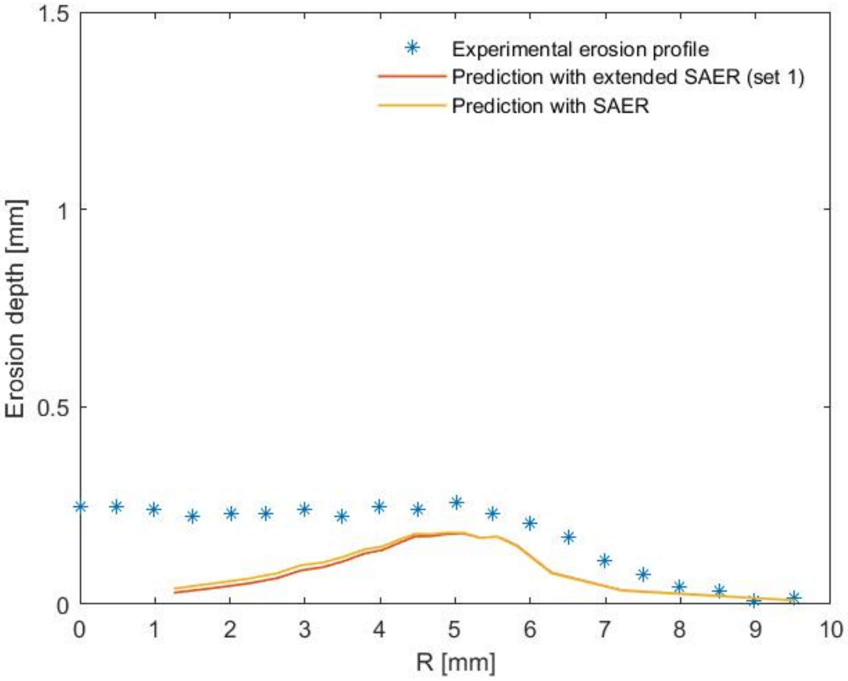

Figure 4.2: Extended SAER performance in case 5 ($d = 120\mu m$).

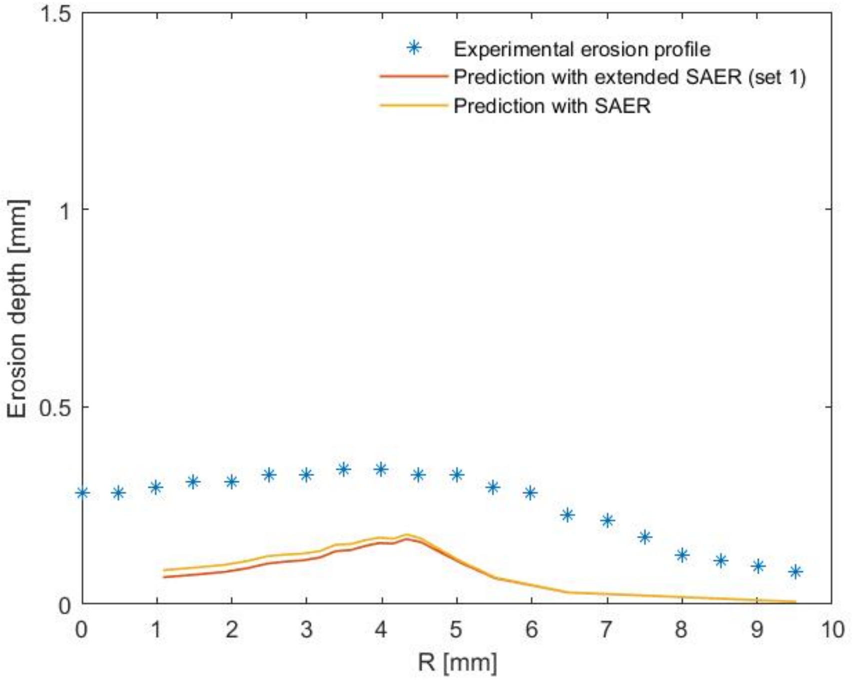

Figure 4.3: Extended SAER performance in case 12 ($d = 250\mu m$).

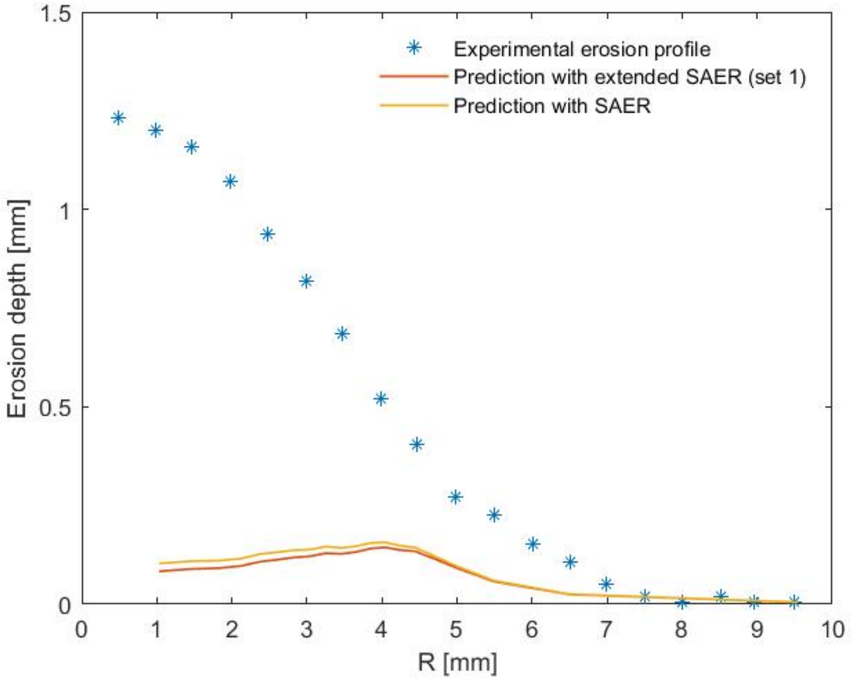

Figure 4.4: Extended SAER performance in case 20 ($d = 350\mu m$).

4.1.2. Validation using the second set of coefficients

Figures 4.5 - 4.8 show the erosion capability of the SAER method if the velocity exponent is included in the fitting session and negative values are allowed (set 2). In Fig. 4.5, the calibration case is reported, where both the extended SAER and the original SAER approach accurately reproduce the experimental profile, as could be expected.

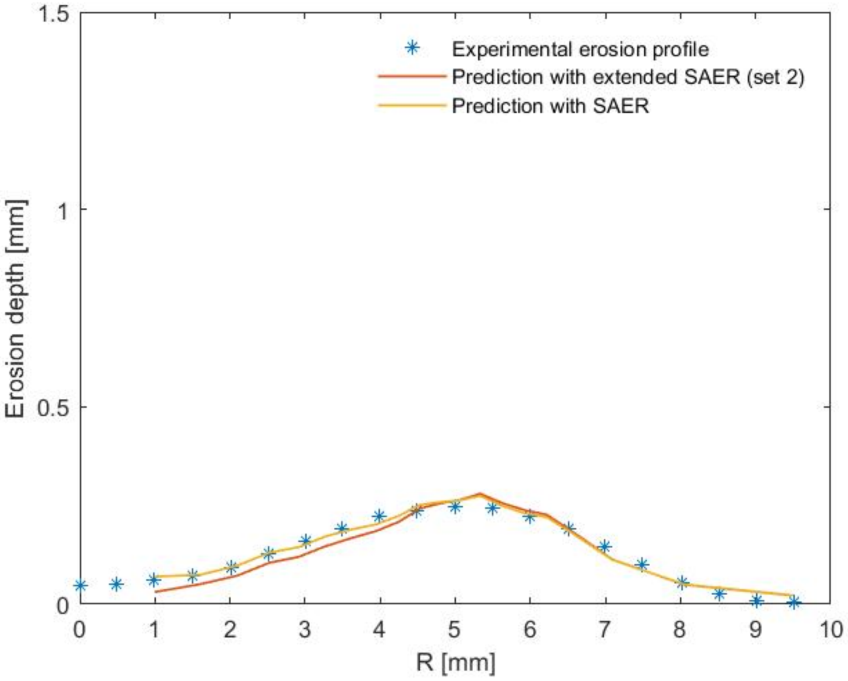

Figure 4.5: Extended SAER performance in case 1 ($d = 90\mu m$).

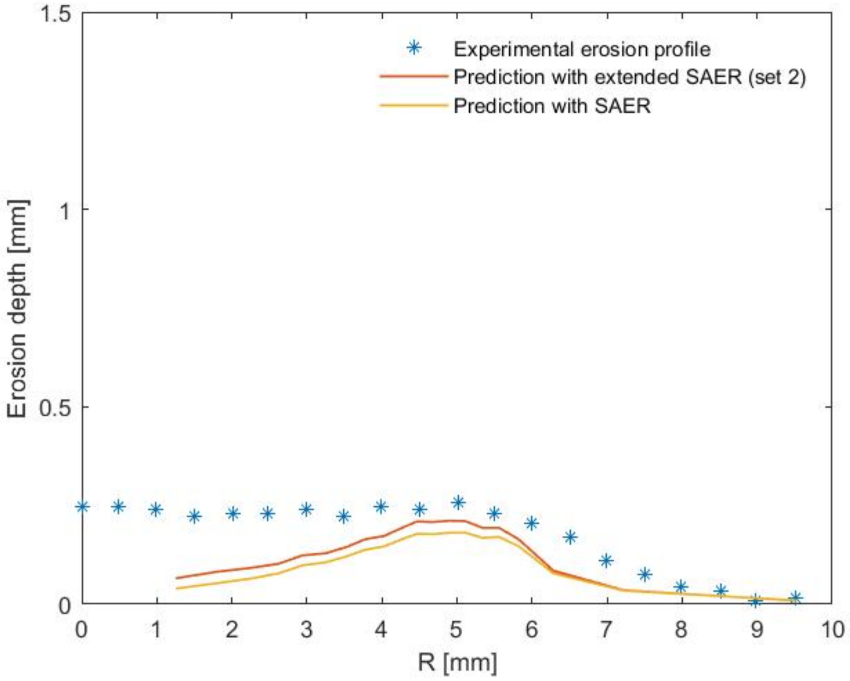

Figure 4.6: Extended SAER performance in case 5 ($d = 120\mu m$).

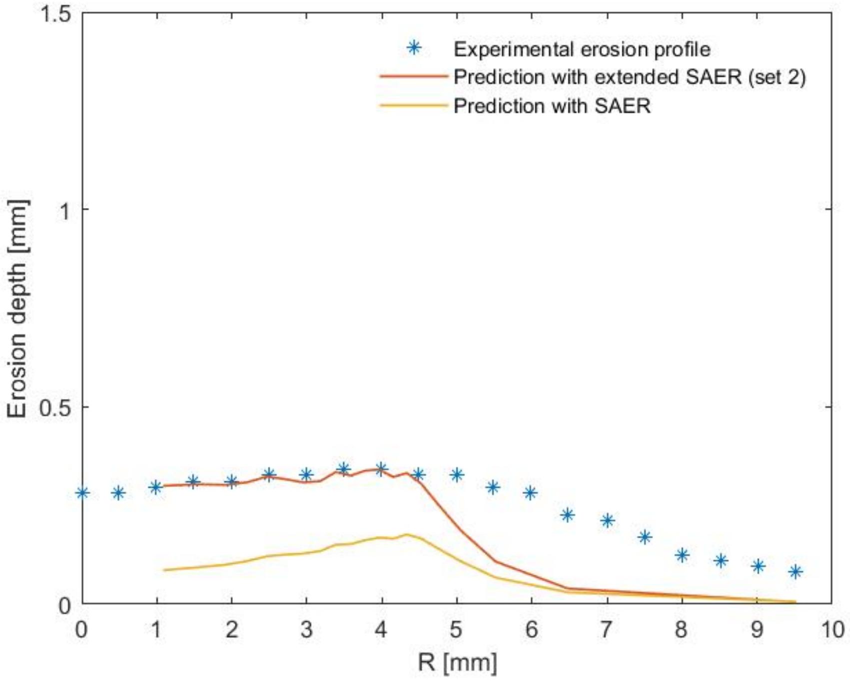

Figure 4.7: Extended SAER performance in case 12 ($d = 250\mu m$).

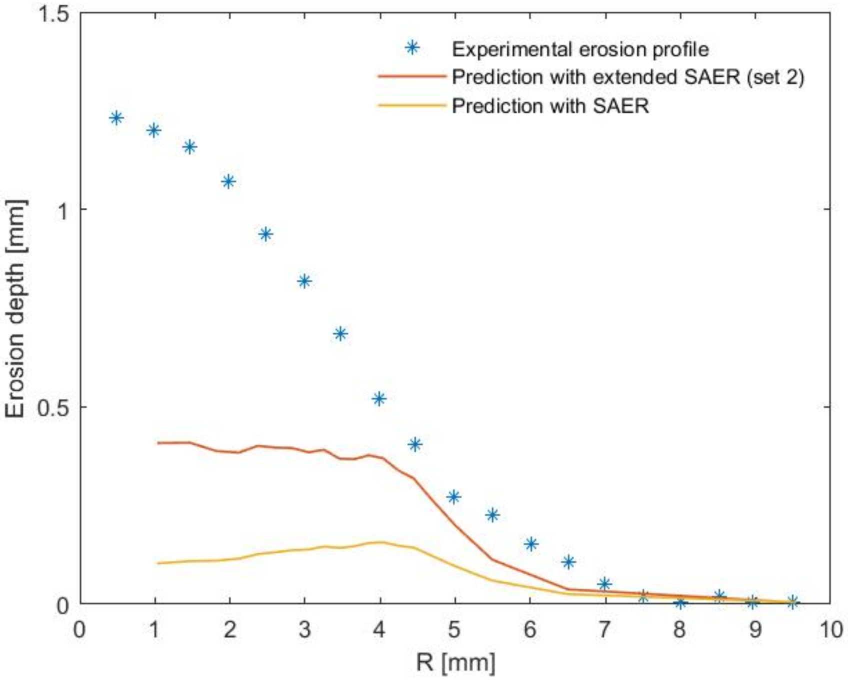

Figure 4.8: Extended SAER performance in case 20 ($d = 350\mu m$).

The results are much more accurate than those obtained in Chapter 3. In particular, Figs. 4.7 and 4.8 show a great improvement in the erosion prediction for tests involving particle diameters (250 μm and 350 μm) significantly different than the one used in the calibration case (90 μm). In case 12, the extended procedure captures the experimental profile much better than the original SAER, describing even the innermost part with good accuracy. This is a major improvement, as Wang showed in [1] how the poor predictive performance in the central part of the sample was one of the weaknesses of the SAER method. In case 20, the extended SAER reproduces the experimental profile in a wider R range, while underestimating the scar depth in the central region of the specimen. Still, this represents a significant increase of the predictive ability of the method.

Nevertheless, accepting set 2 as a meaningful choice of parameters has deep consequences on how the erosion phenomenon is intended and modelled.

A combination of plastic deformation and cutting action, see Section 1.3.1, of the particles impinging on the sample wall is the physical feature that has led to the most widely used impact angle function models. Allowing one of the coefficients to be negative means reverting the qualitative trend of cutting, as a function of the particle's impact angle.

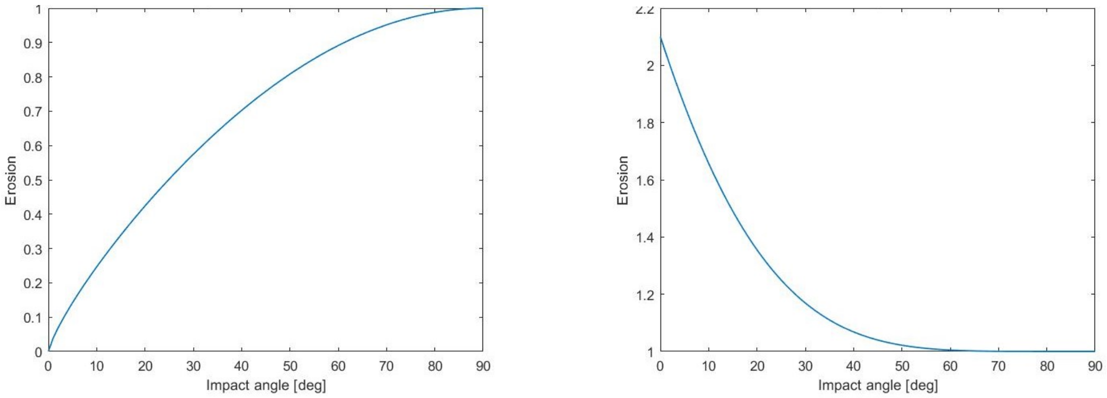

(a) Repeated deformation.

(b) Cutting action.

Figure 4.9: Basic erosion mechanisms.

Figure 4.9 shows the plots of the two basic erosion mechanisms, contributing to the erosion model of Eq.3.4, namely, repeated deformation and cutting action [46]. Repeated deformations are related to the plastic behaviour of the sample material and are more relevant at higher impact angles. Cutting, instead, is the physical process that characterizes impacts at small angles, where a particle impinges on a wall and takes away a small part of material.

The plastic behaviour is modelled via Eq.4.2

$$f_1(\theta_{P,imp}) = (sin(\theta_{P,imp}))^b \tag{4.2}$$

while the cutting action is represented by Eq.4.3

$$f_2(\theta_{P,imp}) = (1 + H_v\,(1 - sin(\theta_{P,imp})))^c \tag{4.3}$$

The two plots of figure 4.9 have been obtained by setting $b = 0.8091$ and $c = 2.7$ as in set 1 (see Table 4.1). Clearly, to retain the qualitative behaviour that stems from this erosion conceptualization, only positive values can be attained by the coefficients. Conversely, the negative value $c = -1.236$ as in set 2 of Table 4.1 leads to the plot in Fig. 4.10, which shows a non-physical behaviour.

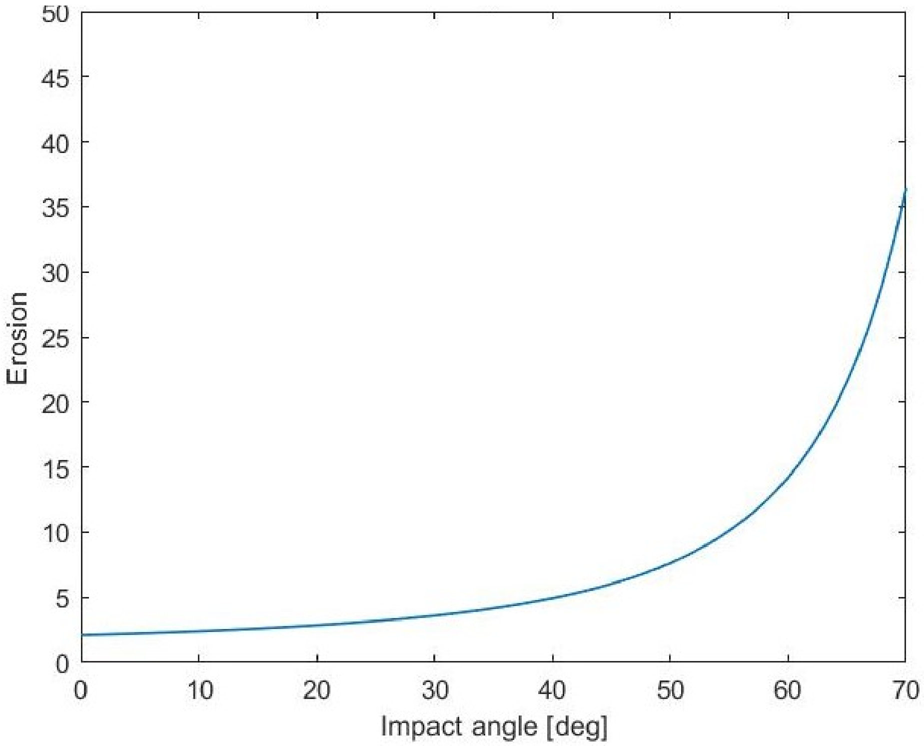

Figure 4.10: Cutting action plot as in set 2.

Finding an explanation for the accuracy improvement that a negative coefficient has brought is not straightforward. The goal of this section, therefore, is not to provide a different perspective on the concept of erosion, but to draw the right conclusions from the obtained results. To this aim, the physical consistency of the chosen model cannot be set aside, but hints to its limitations have to be kept into consideration, as well. Further study on the performance of the coefficients in set 2 appears necessary, in light of the great predictive ability improvement.

4.2. An alternative model for the impact velocity function

Another way of improving the SAER procedure described in Chapter 3 could be to select a different model for the impact velocity function. The simple exponential model of Eq. 3.3 has been widely used for its simplicity. The basic idea is that the relevant physical quantity should be the impact kinetic energy. Therefore, modelling erosion as a quadratic function of velocity (the exponent n is close to 2 in most models) appears to be a fair assumption.

Lester et al. [15] have investigated the inclusion of the velocity exponent n in the fitting

process and found some drawbacks in the results that made the exponential model appear unsuitable, or not really general. They applied an analogous approach to the one described in Section 4.1 to two different W-DITs and calibrated both the coefficients for an impact angle function, as proposed by Finnie [21] (Eq.1.4), and the velocity exponent n.
The found sets of coefficients yielded two impact velocity functions that were too far apart. Therefore, the authors concluded that there must be some inconsistency in the chosen erosion model, since the functional relation between erosion depth and impact angle should be unique, for a given combination of erodent/sample materials.
The model they found most suitable for the erosion dependence on impact velocity was that in Eq.4.4. This choice allowed to find a unique impact velocity function, but it showed non-physical features (the velocity function has a decreasing trend, past a critical value).

	a	b	c	d_1	d_2	d_3	d_4	R^2
set 4	$9.2 \cdot 10^{-10}$	0.33	0.87	2.03	0.97	1.7	0.016	0.84

Table 4.2: Fitting coefficients using an alternative velocity model, Eq. 4.4.

$$g(v) = g_0\, v + g_1\, v^2 + g_2\, (e^{g_3\, v} - 1) \tag{4.4}$$

Figures 4.11 - 4.14 show the SAER performance on erosion prediction using the impact velocity model of Eq. 4.4, in combination with the Oka model, Eq. 1.7 for impact angle dependency (in red), compared with the curves found with the set of coefficients determined in Chapter 3 (in yellow).

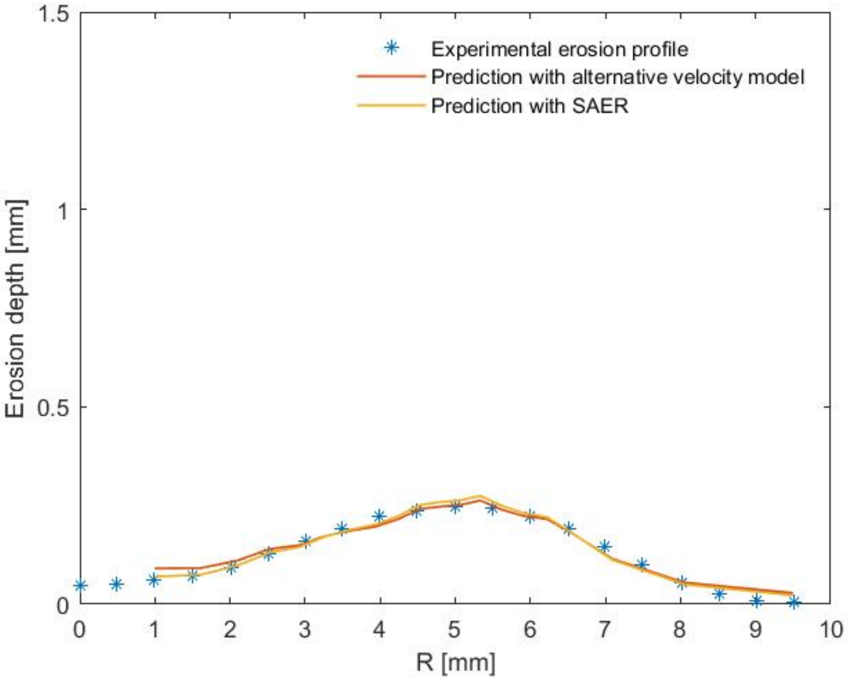

Figure 4.11: Case 1 ($d = 90\ \mu m$): comparison between the SAER approach and the extended SAER, adopting a velocity function model as in Eq. 4.4.

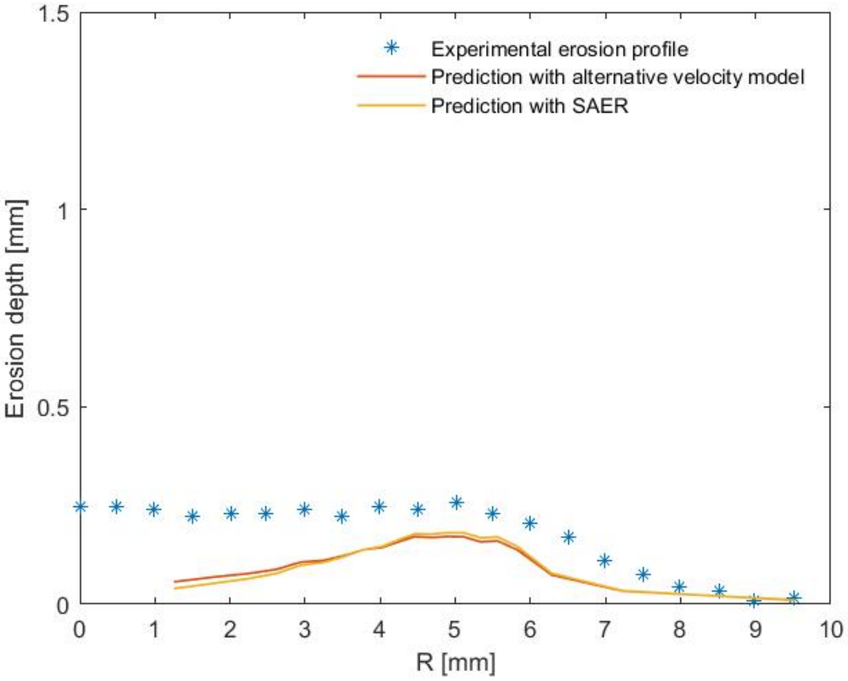

Figure 4.12: Case 5 ($d = 120\ \mu m$): comparison between the SAER approach and the extended SAER, adopting a velocity function model as in Eq. 4.4.

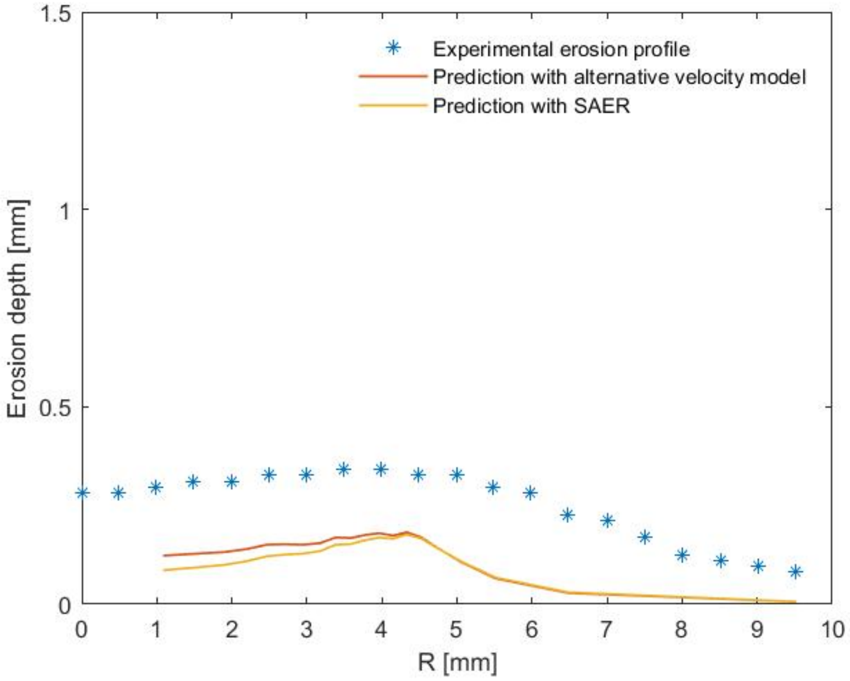

Figure 4.13: Case 12 ($d = 250\ \mu m$): comparison between the SAER approach and the extended SAER, adopting a velocity function model as in Eq. 4.4.

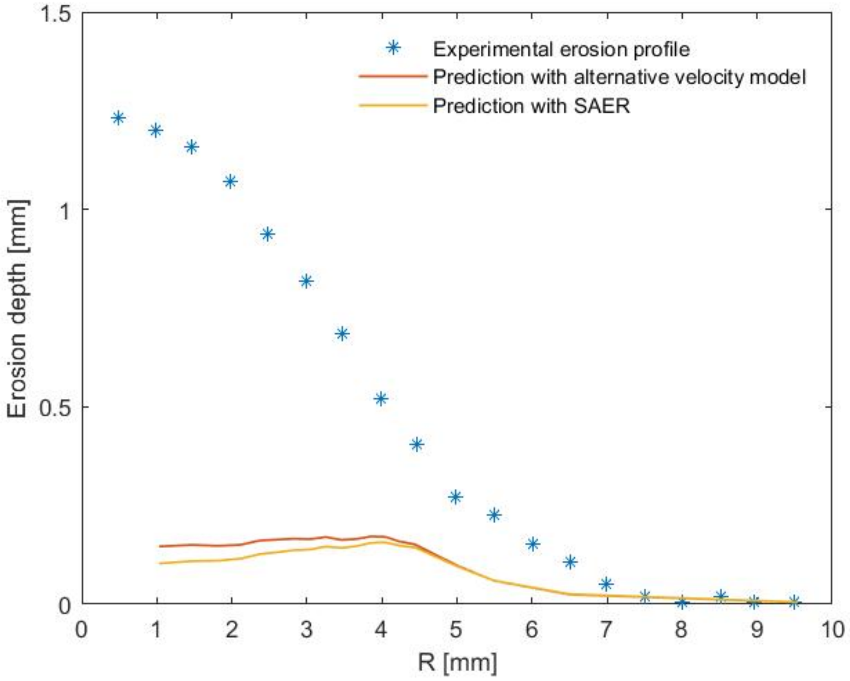

Figure 4.14: Case 20 ($d = 350\ \mu m$): comparison between the SAER approach and the extended SAER, adopting a velocity function model as in Eq. 4.4.

Fig. 4.11 shows the model ability to reproduce the experimental profile used in the calibration phase. Both approaches accurately describe the laboratory data, as could be expected.

A slight improvement of the erosion prediction capacity of the method can be observed in the range R<5 mm for all particle diameters, but the overall performance in cases 5, 12 and 20 does not show significant improvement. Anyway, a different, more involved, impact velocity function may be able to better capture the physical relation with erosion scar depth.

In this coefficient-calibration framework, using a simple exponential model still seems more reasonable, since it only requires one parameter to be calibrated. The alternative velocity function model introduces three more parameters in the fitting session, which will be more time-consuming, while not improving the predictive accuracy in a substantial way.

5 | Towards the application of the proposed method to Abrasive Slurry Jet Machining

The combined numerical-experimental procedure has been used to model a slurry jet test in which the geometric scale and the flow conditions are comparable with those of Abrasive Slurry Jet Machining. Note that, however, the movement of the nozzle has not been considered yet.

The experimental data were provided by the research lab of prof. Marcello Papini from the Ryerson University in Toronto. A slurry jet test with fixed nozzle was performed, using abrasive garnet grains with mean diameter of 34 μm impinging on a stainless steel (SS304) sample. The relevant material properties of the abrasives and of the target material are reported in Table 5.1. Note that a significant difference compared to the tests considered so far is that, in the present case, the slurry jet is free, in the sense that it discharges in air. This creates a three-phase flow (water-abrasives-air), which demands for more advanced fluid dynamic models. Particularly, use was made of the Volume of Fluid model (VOF), previously described in Section 2.2.1, combined with the DPM for the tracking of the trajectories of the abrasives.
In the Section 5.1, the geometry and numerical setup are described. Then, the simulation results and the calibrated set of coefficient are discussed in Sec5.2. Table 5.1 summarizes the main settings of the test case.
Since the presented modelling technique is based on a steadiness assumption, the modification to the sample surface due to erosion are implicitly neglected. Therefore, only shallow profiles can be accurately modeled, as deeper holes would require accounting for geometry changes, that directly affect the flow evolution.

Abrasive material	Garnet
Particle density	4000 kg/m^3
Particle mean diameter	34 μm
Target material	SS304
Sample density	8000 kg/m^3
Vicker's hardness of the sample	0.847 GPa
Stand-off distance	1 mm
Sample diameter	1.5 mm
Nozzle diameter	254 μm
Operating pressure	137 MPa

Table 5.1: Description of the test case.

The experiments were carried out using an OMAX 2626 Jet Machining Center, Fig 5.1. The OMAX machine could perform both AWJM and High-pressure ASJM tests, being switched between the two via a 3.2 mm diameter tube, Fig. 5.2, that connected the nozzle to either a dry abrasive hopper or an abrasive slurry tank.
The experimental setup and details about the OMAX machine have been described in [71].

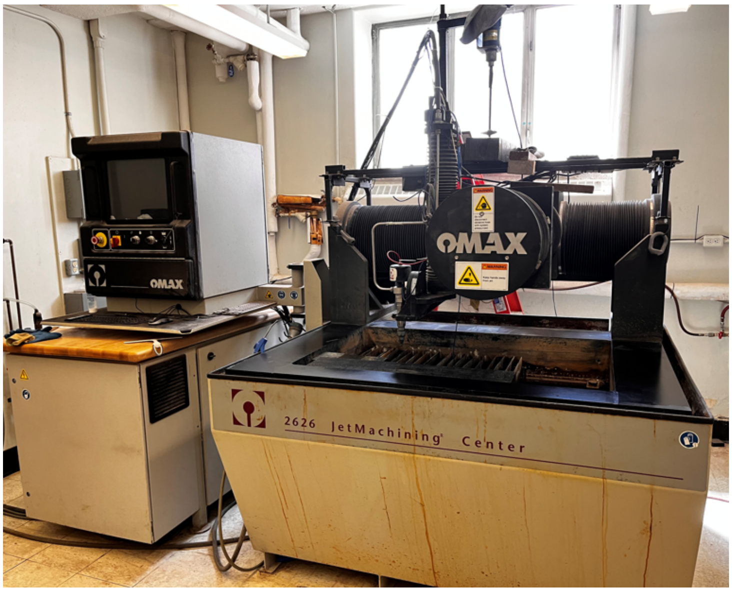

Figure 5.1: OMAX 2626 Jet Machining Center used for the experimental tests.

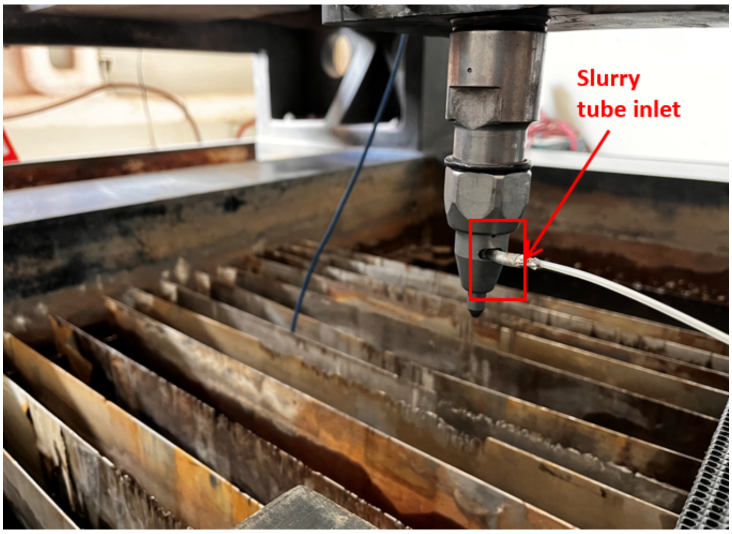

Figure 5.2: Nozzle and connection tube in the OMAX machine.

The available operating pressures for the OMAX machine used in the testing phase were 137 MPa and 193 MPa, corresponding to a water speed at the nozzle outlet of approximately 192 m/s and 230 m/s, respectively. The estimates of the outlet speed were computed using a Matlab code discussed in Hagbin et al. [71].

The high velocity and abrasiveness of garnet grains made creating shallow profiles a non-trivial task. The experimental test carried out with 137 MPa for the operating pressure and a dwell time of 100 ms produced a shallow profile. Thus, for this case the erosion equation could be calibrated following the present modelling procedure. In addition, a different test with the same operating pressure but dwell time equal to 250 ms provided useful data to assess the time evolution of the erosion scar, as it will be explained in Section 5.3). Unfortunately, testing with different operating conditions yielded unsuitable depths and thus a complete validation of the calibrated formula could not be reached in the context of the present thesis.

5.1. Geometry and numerical setup

The computational domain is reported in Fig. 5.3a and its dimensions in Fig. 5.3b. The stand-off distance is 1 mm, while the sample diameter is 3 mm. The nozzle has a 254 μm diameter.

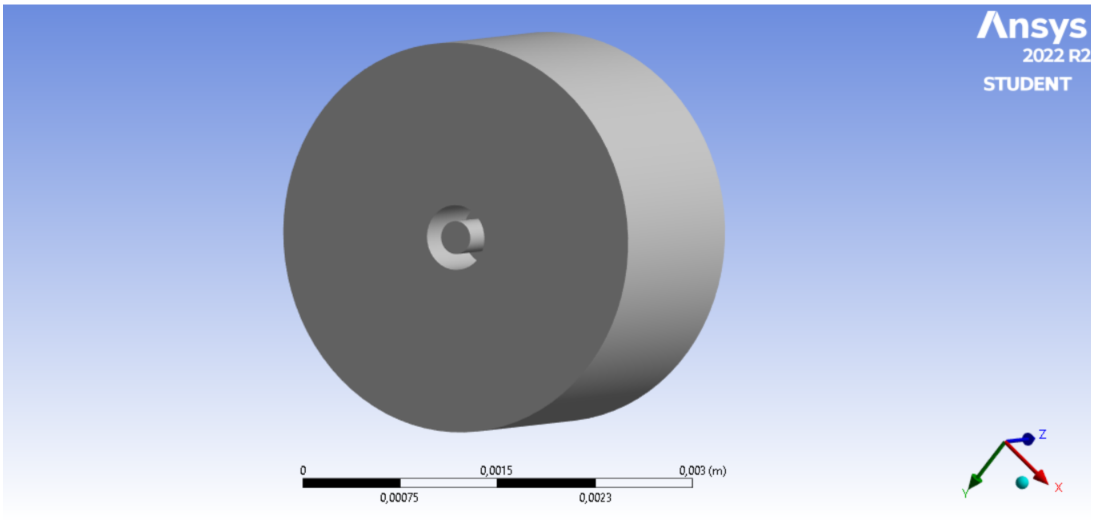

(a) Computational domain.

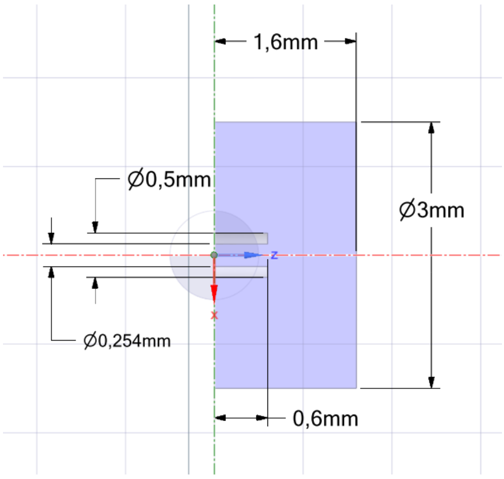

(b) Test case geometry.

Figure 5.3: Computational domain (a) and geometrical dimensions (b).

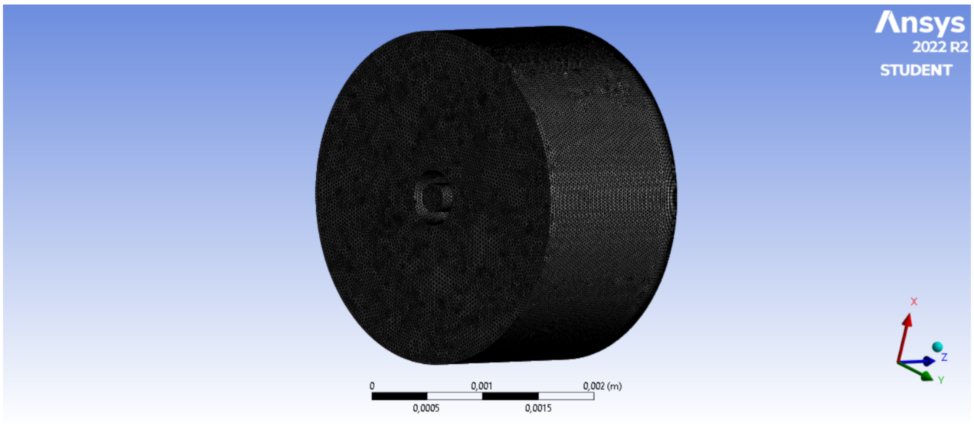

Figure 5.4: Test case mesh 3.

An inflation layer was created to get a more accurate description of the flow close to the physical walls, namely the nozzle and the sample surface, with a first layer thickness of 5 μm and a growth rate equal to 1.05 for 5 and 10 layers, respectively. A grid-sensitivity analysis was performed, comparing three different meshes. The number of elements of each mesh are reported in Table 5.2. A view of the domain discretized using mesh 3 is shown in Figure 5.4. Similarly to what has been done in Section 3.2.4, the target parameter of the grid independence study was the area-averaged static pressure on a plane parallel to the sample surface, 0.2 mm above it. The results are shown in Table 5.2. The pressure change from mesh 2 to mesh 3 was minimal, below 1%, so mesh 3 was selected, Fig. 5.4.

	Number of elements [thousands]	**Mean static pressure [kPa]**
mesh 1	300	39.64
mesh 2	375	40.94
mesh 3	470	41.22

Table 5.2: Tested meshes.

The mean features of the numerical setup are summarized in Table 5.3. The two-phase flow (water-air) was solved using the VOF model, described in Section 2.2.1. Air and water were set as primary and secondary phase, respectively, including a surface tension coefficient of 0.072 N/m. The SIMPLE method was used to handle the pressure-velocity coupling.

Multiphase model	Volume of Fluid
Turbulence model	k-epsilon realizable
Near-wall treatment	Scalable wall function
Solver	Pressure-based, steady
Pressure-velocity coupling	SIMPLE
Discretization accuracy	second order

Table 5.3: Main numerical settings of the CFD simulation.

Then, the particles' trajectories were tracked through the Discrete Phase Model, presented in Chapter 3. The dispersed phase concentration used in the experiments was 10% in weight, that corresponds to a volumetric concentration of about 2.7%, low enough to ignore, at least as a first approximation, the effect of the particles on the fluid flow field

[14]. The particles' shape factor was set to 0.38. All other settings are similar to the test case analysed in Chapter 3. The flow boundary conditions were set to a fully-developed turbulent flow, with mean velocity equal to 192 m/s and a no-slip, smooth-wall condition was applied to physical walls.

A steady-state simulation was performed. Fig. 5.5 shows the water fraction at initialization. The whole domain was filled with air, by patching a null volume fraction for water (blue in Fig. 5.5). As for water, a volume fraction equal to 1 at the inlet boundary was set (red in Fig. 5.5), while a null backflow volume fraction was imposed at the outlet boundary.

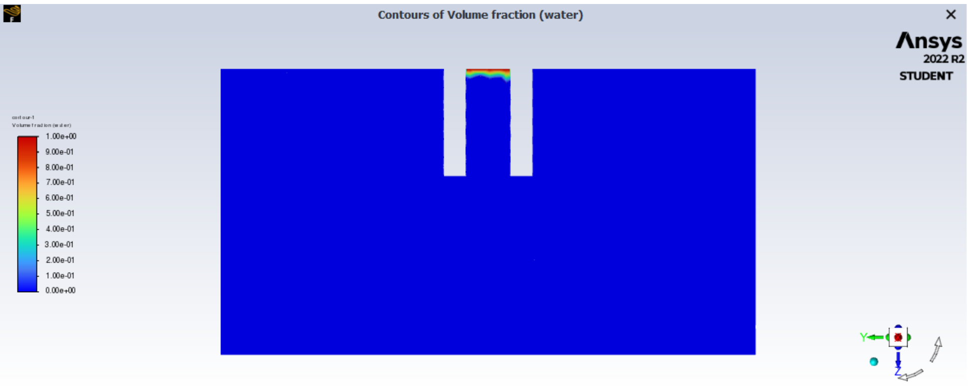

Figure 5.5: Water fraction after initialization.

At convergence of the steady-state simulation (that is, after about 1000 iterations), the pattern of the volume fraction was as shown in Fig. 5.6. The water flow, in red in Fig. 5.6 is in an air environment. At the flow periphery, where the figure shows yellow and green patches, the computational cells contain both water and air. Some air particles have been entrained in the flow, as typically happens in free water jets.

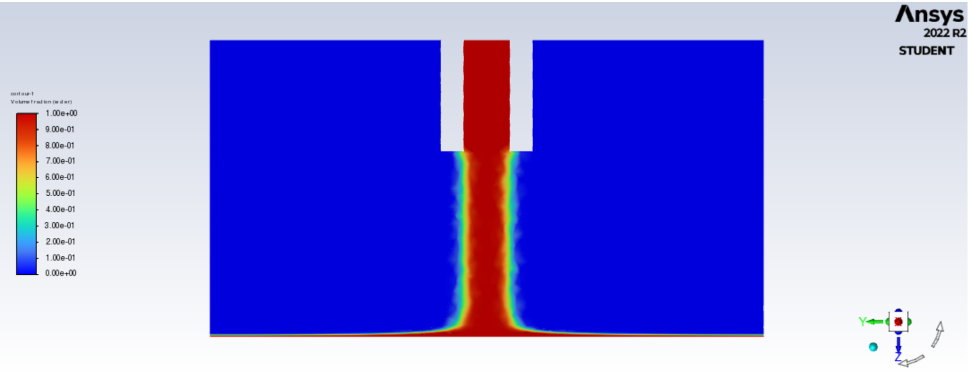

Figure 5.6: Water fraction after 1000 iterations.

The impact statistics, namely, ring-averaged impact velocity, ring-averaged impact angle and impact density, are shown in Figs. 5.7 - 5.9. In the sensitivity study detailed in Chapter 3, it was proven that injecting 50000 particles and creating 20 rings did not affect the results. Accordingly, in this test case, the number of particles was 50000, while the number of rings was doubled, equal to 40000, to increase the number of points available for the fitting session and, thus, the accuracy of the found model. The analysis focused on the impacts within a 0.5 mm distance from the nozzle axis, since the vast majority of the impacts occurred in this region. The plot of the impact number density at varying radial distance from the nozzle axis (Fig. 5.9) shows this trend.

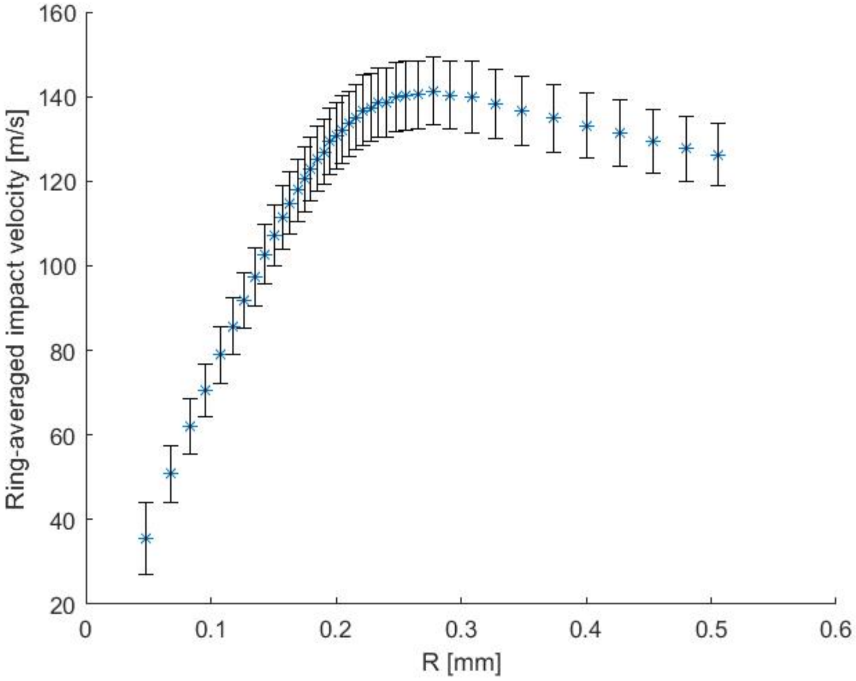

Figure 5.7: Ring-averaged impact velocity and associated standard deviation error bars.

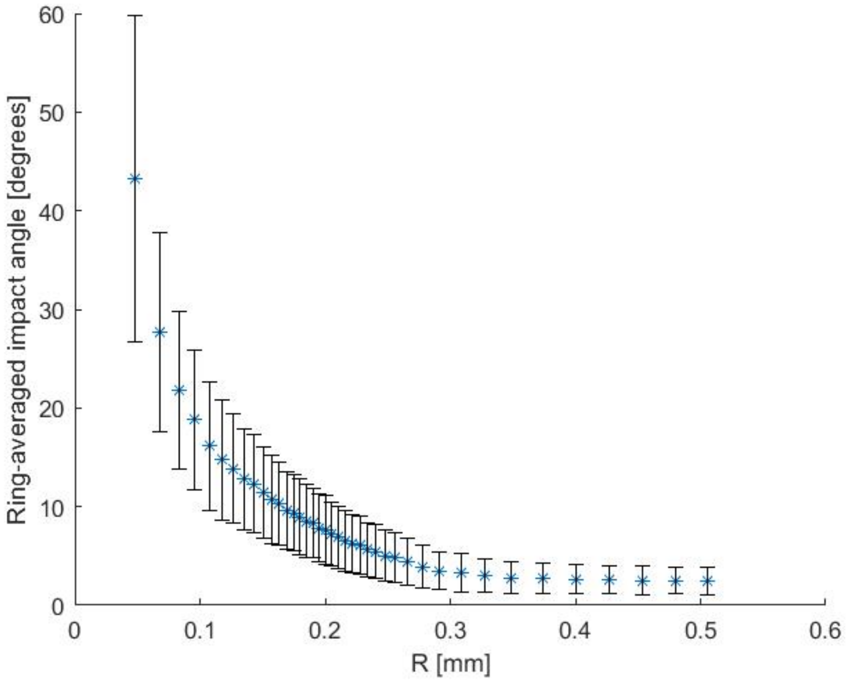

Figure 5.8: Ring-averaged impact angle and associated standard deviation error bars.

The impact velocity, Fig. 5.7, has a steeper trend than that observed in Ch. 3. This could be due to the much higher jet velocity, that increases the drag force exerted by the fluid phase on the particles, and to the smaller stand-off distance. The impact angle trend, Fig. 5.8, shows higher values in the innermost region, that quickly decrease, moving towards the periphery. The vast majority of impacts happened at a low angle, $\bar{\theta}_{p,imp} < 20\circ$, thus reducing the range of calibration available for the SAER procedure.

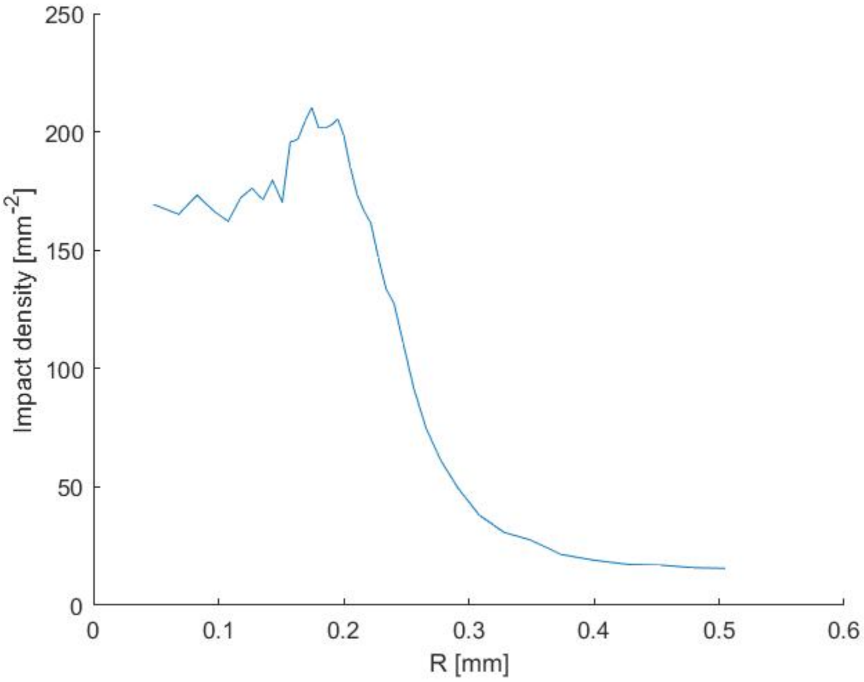

Figure 5.9: Impact density.

5.2. Calibration results

The calibration was carried out using the Oka model, Eq. 1.7, for the impact angle function and a power law with exponent n for the impact velocity function. Since no suitable value for n could be inferred from the literature, the extension of the SAER procedure presented in Sec. 4.1 was adopted (see Eq. 4.1).
The results of the fitting session are reported in Table 5.4.

a	b	c	n	R^2
$5.5 \cdot 10^{-08}$	4.496	4.421	3.007	0.83

Table 5.4: Fitting coefficients.

The calibrated coefficients allowed to reproduce the experimental erosion profile quite accurately, as it can be seen in Fig. 5.10.

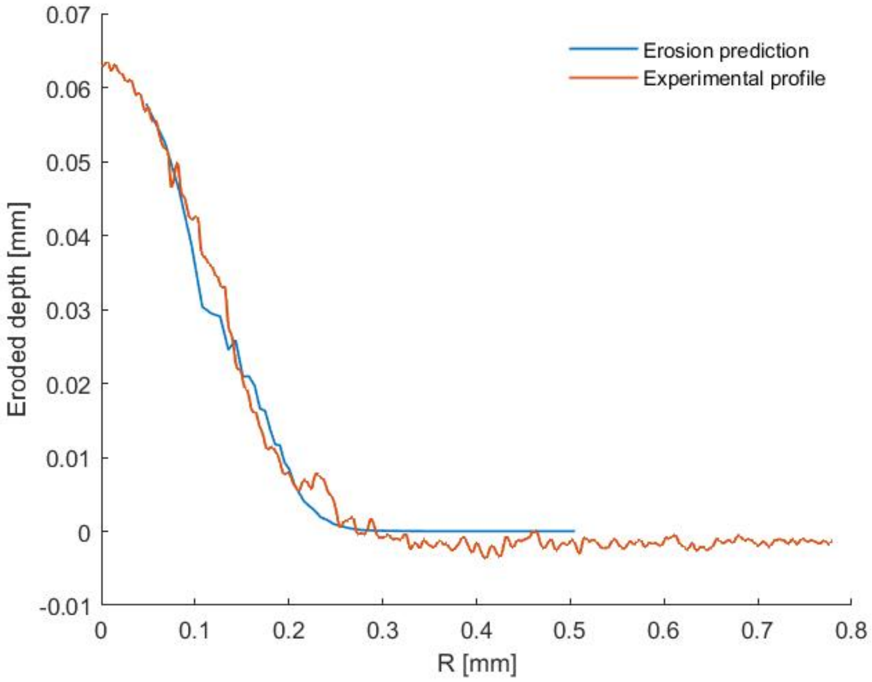

Figure 5.10: Erosion prediction and experimental profile.

The found value for n is in the range that is usually associated to ductile materials, namely between 2 and 4.

Nevertheless, the calibrated impact angle function, Fig. 5.11 does not follow the typical qualitative behaviour, with an early peak at low angles and then a decreasing trend. This could be a consequence of the really limited impact angle range obtained, which only allows for a partial description of the angle influence, but it could also be an indication of the inaccuracy of the chosen mathematical model, similarly to what was discussed in Section 4.1.2.

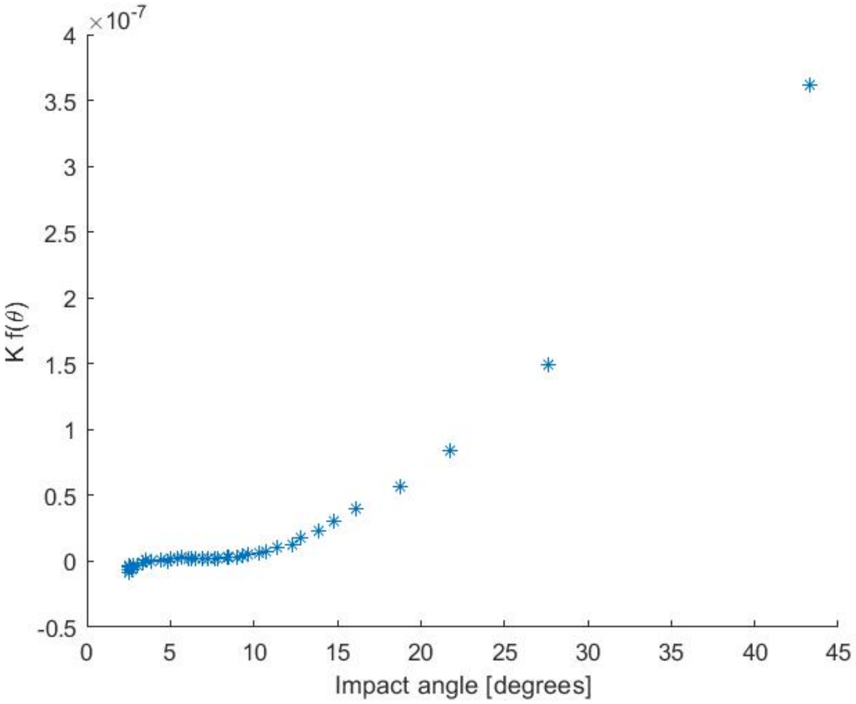

Figure 5.11: Impact angle function.

5.3. Prediction for a different exposure time

The slurry jet test has been repeated in the lab of prof. Marcello Papini by increasing the dwell time from 100 ms to 250 ms. The experimental erosion profiles obtained with the two dwell times are reported in Fig. 5.12. As expected, increasing the dwell time leads to an increase of the erosion depth. Anyway, in the inner part the erosion is less than linear with time. This may be due to the geometry changes [72], that have been neglected in this study, owing to the steady-state nature of the SAER approach.

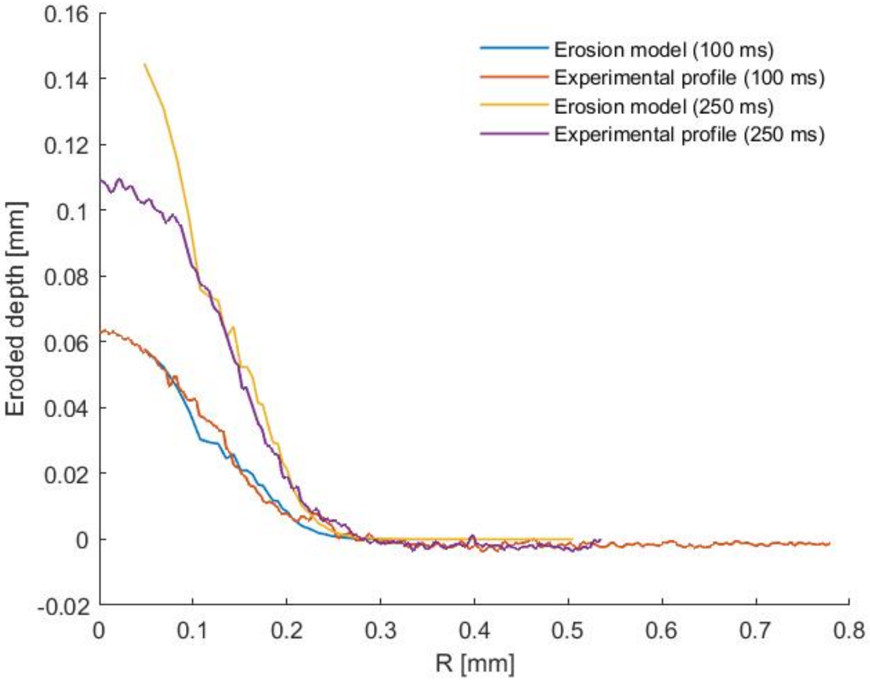

Figure 5.12: Erosion profiles resulting from different dwell time.

The erosion profile has been predicted also in the case of 250 ms dwell time. The comparison between model prediction and experimental profiles is shown, for both cases, in Fig. 5.12. The equation was calibrated on the 100 ms long test, so it describes it accurately. Since the calibration procedure is steady, it is not surprising that the predicted profiles are linearly dependent on the elapsed time (see Eq.3.1). Consequently, the predicted curve overestimates the erosion depth in the inner part (R smaller than 0.1 mm). Conversely, the numerical prediction is in good agreement with the experimental findings in the outer part of the sample.

6 | Conclusions and future developments

The presented thesis describes possible improvements to a numerical-experimental methodology for the calibration of erosion model specifically developed for slurry conditions. The methodology, initially proposed by researches from the Erosion/Corrosion Research Centre at the University of Tulsa [64] and further modified by Messa et al. [69] and Wang [1], yielded more accurate erosion prediction results compared to traditionally used models. The basic idea of the methodology is: (1) to perform a certain slurry erosion experiment and measure the erosion depth distribution; (2) to simulate numerically the slurry flow in the same experimental test and obtained information on the particle-wall impacts; (3) to combine the information obtained experimentally and numerically to determine the coefficients of an erosion model using regression techniques. In the formulation reported in Messa et al. [69], the number of coefficients to be calibrated were three, and the calibration case was a wet direct impact test, that is a laboratory experiment where a water-sand jet impacted on a flat aluminium sample.
Two test cases have been studied, that differ in both geometrical features, operating flow conditions and involved materials.

Particularly, the first test case, reported in Wang [1], involved a slurry flow made of water and glass beads and a flat aluminium sample. The jet velocity was about 36 m/s and the test was repeated using different glass beads, with $90\mu m$, $120\mu m$, $250\mu m$, $350\mu m$ diameter, respectively. The smallest particles were employed in the calibration case, to optimize the coefficient of the erosion model. Then, the resulting formula was applied to describe the erosion profiles stemming from the other three tests. The calibrated model could reproduce the laboratory data for $120\mu m$ and $250\mu m$ diameter glass beads quite accurately, while its predictive performance for the $350\mu m$ diameter was poor.

In order to further improve the performance of the calibration methodology compared to the formulation proposed by Messa et al. [69], the first attempt made was to use a different model to account for the effect of the particle impact velocity. Specifically, whereas the original formulation considered a power law dependence of erosion on impact velocity, with the power exponent being fixed equal to 2.1, a different impact velocity function, proposed by Lester et al. [15] has been explored. However, this led to a slight improvement of the predictive ability of the model, although increasing the number of fitting parameters from four to seven.

The second attempt was to use the original power law impact velocity function but including the power exponent among the calibration coefficients. This choice led to significant improvement in terms of accuracy of the calibrated model. The resulting equation reproduced the experimental erosion profiles more precisely and over a wider region of the sample surface, even though the impact angle function showed non-physical features.

Finally, the second test case was addressed. This case was characterized by a high-pressure abrasive slurry jet, made of water and $38\mu m$ diameter garnet grains, with a jet velocity of about 192 m/s. The experimental profiles were measured by Marcello Papini and Majid Moghaddam, at the Ryerson University, Toronto, Canada. The fitting process of the impact angle and impact velocity function parameters applied to the second presented test case yielded remarkable results. The calibrated erosion model accurately reproduced the experimental profile, proving that the numerical-experimental methodology is applicable to different geometrical scales and operating conditions, with respect to the tests analysed in [1]. A further development of this modelling approach should aim at linking it more closely to the physical phenomenon, making it a phenomenological model, thus accounting for the main features of erosion dynamics.

The modifications made to the methodology appear promising improvements. In addition, the good results obtained in the second test case show that, in principle, the combined numerical-experimental calibration strategy might be applicable also to the typical conditions of ASJM. At the same time, further study on the fitting process and on the physical meaning of the coefficients is necessary. This would allow more confidence in the resulting model predictive ability, which is remarkably higher than its previous version. Then, further steps towards the modelling of the actual ASJM processes could be made, for instance by accounting for the flow modifications produced by geometry changes or by including the movement of the nozzle in the CFD set up.

Bibliography

[1] Yongbo Wang. *A modelling framework for slurry erosion prediction through Computational Fluid Dynamics simulations*. PhD thesis, Politecnico di Milano, 2021.

[2] Hiroki Endo and Etsuo Marui. Small-hole drilling in engineering plastics sheet and its accuracy estimation. *International Journal of Machine Tools and Manufacture*, 46(6):575–579, 2006. ISSN 0890-6955. doi: https://doi.org/10.1016/j.ijmachtools.2005.07.026. URL `https://www.sciencedirect.com/science/article/pii/S0890695505001653`.

[3] Y. Altintas, G. Stepan, D. Merdol, and Z. Dombovari. Chatter stability of milling in frequency and discrete time domain. *CIRP Journal of Manufacturing Science and Technology*, 1(1):35–44, 2008. ISSN 1755-5817. doi: https://doi.org/10.1016/j.cirpj.2008.06.003. URL `https://www.sciencedirect.com/science/article/pii/S1755581708000072`.

[4] Omer Ozkirimli, Lutfi Taner Tunc, and Erhan Budak. Generalized model for dynamics and stability of multi-axis milling with complex tool geometries. *Journal of Materials Processing Technology*, 238:446–458, 2016. ISSN 0924-0136. doi: https://doi.org/10.1016/j.jmatprotec.2016.07.020. URL `https://www.sciencedirect.com/science/article/pii/S0924013616302370`.

[5] Y. Altintas and A. Woronko. A piezo tool actuator for precision turning of hardened shafts. *CIRP Annals*, 51(1):303–306, 2002. ISSN 0007-8506. doi: https://doi.org/10.1016/S0007-8506(07)61522-4. URL `https://www.sciencedirect.com/science/article/pii/S0007850607615224`.

[6] Kulecki. Process and apparatus developments in industrial waterjet applications. *International Journal of Machine Tools and Manufacture*, pages 667–673, 2002.

[7] Janet Folkes. Waterjet—an innovative tool for manufacturing. *Journal of Materials Processing Technology*, 209(20):6181–6189, 2009. ISSN 0924-0136. doi: https://doi.org/10.1016/j.jmatprotec.2009.05.025. URL `https://www.sciencedirect.`

`com/science/article/pii/S0924013609002179`. Special Issue: 1st International Conference on Abrasive Processes.

[8] H. Syazwani, G. Mebrahitom, and A. Azmir. A review on nozzle wear in abrasive water jet machining application. *IOP Conference Series: Materials Science and Engineering*, 114(1):012020, feb 2016. doi: 10.1088/1757-899X/114/1/012020. URL `https://dx.doi.org/10.1088/1757-899X/114/1/012020`.

[9] E Belloy, S Thurre, E Walckiers, Abdeljalil Sayah, and M.A.M Gijs. Introduction of powder blasting for sensor and microsystem applications. *Sensors and Actuators A: Physical*, 84:330–337, 09 2000. doi: 10.1016/S0924-4247(00)00390-3.

[10] Stefan Schlautmann, Henk Wensink, Richard Schasfoort, Miko Elwenspoek, and Albert van den Berg. Powder-blasting technology as an alternative tool for microfabrication of capillary electrophoresis chips with integrated conductivity sensors. *Journal of Micromechanics and Microengineering*, 11(4):386, jul 2001. doi: 10.1088/0960-1317/11/4/318. URL `https://dx.doi.org/10.1088/0960-1317/11/4/318`.

[11] H. Nouraei, K. Kowsari, J.K. Spelt, and M. Papini. Surface evolution models for abrasive slurry jet micro-machining of channels and holes in glass. *Wear*, 309(1): 65–73, 2014. ISSN 0043-1648. doi: https://doi.org/10.1016/j.wear.2013.11.003. URL `https://www.sciencedirect.com/science/article/pii/S0043164813005383`.

[12] Henk Wensink, Stefan Schlautmann, Martijn H Goedbloed, and Miko C Elwenspoek. Fine tuning the roughness of powder blasted surfaces. *Journal of Micromechanics and Microengineering*, 12(5):616, jun 2002. doi: 10.1088/0960-1317/12/5/316. URL `https://dx.doi.org/10.1088/0960-1317/12/5/316`.

[13] Said Elghobashi. An updated classification map of particle-laden turbulent flows. 81: 3–10, 01 2006.

[14] Gianandrea Messa and Stefano Malavasi. The effect of sub-models and parameterizations in the simulation of abrasive jet impingement tests. *Wear*, 370, 11 2016. doi: 10.1016/j.wear.2016.10.022.

[15] D.R. Lester, L.A. Graham, and J. Wu. High precision suspension erosion modeling. *Wear*, 269(5):449–457, 2010. ISSN 0043-1648. doi: https://doi.org/10.1016/j.wear.2010.04.032. URL `https://www.sciencedirect.com/science/article/pii/S0043164810001912`.

[16] Muhammad Sukry Azizi Wardi. The impact of sand erosion in gas export pipelines. 2015.

[17] *Evaluation of API RP 14E Erosional Velocity Limitations for Offshore Gas Wells*, volume All Days of *OTC Offshore Technology Conference*, 05 1983. doi: 10.4043/4485-MS. URL `https://doi.org/10.4043/4485-MS`. OTC-4485-MS.

[18] Mamdouh M. Salama. An Alternative to API 14E Erosional Velocity Limits for Sand-Laden Fluids . *Journal of Energy Resources Technology*, 122(2):71–77, 03 2000. ISSN 0195-0738. doi: 10.1115/1.483167. URL `https://doi.org/10.1115/1.483167`.

[19] Brenton McLaury and Siamack Shirazi. An alternate method to api rp 14e for predicting solids erosion in multiphase flow. *Journal of Energy Resources Technology-transactions of The Asme - J ENERG RESOUR TECHNOL*, 122, 09 2000. doi: 10.1115/1.1288209.

[20] Quamrul H. Mazumder, Siamack A. Shirazi, Brenton S. McLaury, John R. Shadley, and Edmund F. Rybicki. Development and validation of a mechanistic model to predict solid particle erosion in multiphase flow. *Wear*, 259(1):203–207, 2005. ISSN 0043-1648. doi: https://doi.org/10.1016/j.wear.2005.02.109. URL `https://www.sciencedirect.com/science/article/pii/S0043164805001882`. 15th International Conference on Wear of Materials.

[21] D.H. McFadden I. Finnie, S.A. Levy. Fundamental mechanism of erosive wear of ductile materials by solid particles. *WEAR 370-371*, pages 36–58, 1979.

[22] Vahid Javaheri, David Porter, and Veli-Tapani Kuokkala. Slurry erosion of steel – review of tests, mechanisms and materials. *Wear*, 408-409:248–273, 2018. ISSN 0043-1648. doi: https://doi.org/10.1016/j.wear.2018.05.010. URL `https://www.sciencedirect.com/science/article/pii/S0043164817311262`.

[23] G.P. Tilly. A two stage mechanism of ductile erosion. *Wear*, 23(1):87–96, 1973. ISSN 0043-1648. doi: https://doi.org/10.1016/0043-1648(73)90044-6. URL `https://www.sciencedirect.com/science/article/pii/0043164873900446`.

[24] IM Hutchings. *Mechanisms of the erosion of metals by solid particles.* ASTM International, 1979.

[25] Amir Mansouri, Siamack Shirazi, and Brenton McLaury. Experimental and numerical investigation of the effect of viscosity and particle size on the erosion damage caused by solid particles. volume 1, 08 2014. doi: 10.1115/FEDSM2014-21613.

[26] K. Kowsari, D.F. James, M. Papini, and J.K. Spelt. The effects of dilute polymer solution elasticity and viscosity on abrasive slurry jet micro-machining of glass. *Wear*, 309(1):112–119, 2014. ISSN 0043-1648. doi: https://doi.org/10.1016/j.

wear.2013.11.011. URL `https://www.sciencedirect.com/science/article/pii/S0043164813005462`.

[27] Mazdak Parsi, Kamyar Najmi, Fardis Najafifard, Shokrollah Hassani, Brenton McLaury, and Siamack Shirazi. A comprehensive review of solid particle erosion modeling for oil and gas wells and pipelines applications. *Journal of Natural Gas Science and Engineering*, 21:850–873, 11 2014. doi: 10.1016/j.jngse.2014.10.001.

[28] Randall S. Lynn, Kien K. Wong, and Hector McI. Clark. On the particle size effect in slurry erosion. *Wear*, 149(1):55–71, 1991. ISSN 0043-1648. doi: https://doi.org/10.1016/0043-1648(91)90364-Z. URL `https://www.sciencedirect.com/science/article/pii/004316489190364Z`.

[29] H.McI Clark and Ryan Hartwich. A re-examination of the 'particle size effect' in slurry erosion. *Wear*, 248:147–161, 03 2001. doi: 10.1016/S0043-1648(00)00556-1.

[30] Girish Desale, Bhupendra Gandhi, and S. Jain. Particle size effects on the slurry erosion of aluminium alloy (aa 6063). *Wear*, 266:1066–1071, 05 2009. doi: 10.1016/j.wear.2009.01.002.

[31] A. Abouel-Kasem. Particle Size Effects on Slurry Erosion of 5117 steels. *Journal of Tribology*, 133(1), 12 2010. ISSN 0742-4787. doi: 10.1115/1.4002605. URL `https://doi.org/10.1115/1.4002605`. 014502.

[32] V.B. Nguyen, Q.B. Nguyen, Y.W. Zhang, C.Y.H. Lim, and B.C. Khoo. Effect of particle size on erosion characteristics. *Wear*, 348-349:126–137, 2016. ISSN 0043-1648. doi: https://doi.org/10.1016/j.wear.2015.12.003. URL `https://www.sciencedirect.com/science/article/pii/S0043164815005098`.

[33] Hakon Wadell. Sphericity and roundness of rock particles. *The Journal of Geology*, 41(3):310–331, 1933. doi: 10.1086/624040. URL `https://doi.org/10.1086/624040`.

[34] Harold Heywood. The evaluation of powders. *Journal of Pharmacy and Pharmacology*, 15(S1):56T–74T, 1963. doi: https://doi.org/10.1111/j.2042-7158.1963.tb11190.x. URL `https://onlinelibrary.wiley.com/doi/abs/10.1111/j.2042-7158.1963.tb11190.x`.

[35] S. Bahadur and R. Badruddin. Erodent particle characterization and the effect of particle size and shape on erosion. *Wear*, 138(1):189–208, 1990. ISSN 0043-1648. doi: https://doi.org/10.1016/0043-1648(90)90176-B. URL `https://www.sciencedirect.com/science/article/pii/004316489090176B`.

[36] Alan V. Levy and Pauline Chik. The effects of erodent composition and shape

on the erosion of steel. *Wear*, 89(2):151–162, 1983. ISSN 0043-1648. doi: https://doi.org/10.1016/0043-1648(83)90240-5. URL `https://www.sciencedirect.com/science/article/pii/0043164883902405`.

[37] Y. Zhang, E.P. Reuterfors, B.S. McLaury, S.A. Shirazi, and E.F. Rybicki. Comparison of computed and measured particle velocities and erosion in water and air flows. *Wear*, 263(1):330–338, 2007. ISSN 0043-1648. doi: https://doi.org/10.1016/j.wear.2006.12.048. URL `https://www.sciencedirect.com/science/article/pii/S0043164807003407`. 16th International Conference on Wear of Materials.

[38] N. Watanabe S. Wada. Solid particle erosion in brittle materials (part 3). *Yogyo-Kyokai-Shi*, 95(6):573–578, 1987.

[39] G.P. Tilly. Erosion caused by airborne particles. *Wear*, 14(1):63–79, 1969. ISSN 0043-1648. doi: https://doi.org/10.1016/0043-1648(69)90035-0. URL `https://www.sciencedirect.com/science/article/pii/0043164869900350`.

[40] Alan V. Levy and Paul Yau. Erosion of steels in liquid slurries. *Wear*, 98:163–182, 1984. ISSN 0043-1648. doi: https://doi.org/10.1016/0043-1648(84)90225-4. URL `https://www.sciencedirect.com/science/article/pii/0043164884902254`.

[41] Alan V. Levy. The solid particle erosion behavior of steel as a function of microstructure. *Wear*, 68:269–287, 1981.

[42] G. L. Sheldon. Effects of Surface Hardness and Other Material Properties on Erosive Wear of Metals by Solid Particles. *Journal of Engineering Materials and Technology*, 99(2):133–137, 04 1977.

[43] Iain Finnie. Erosion of surfaces by solid particles. *Wear*, 3(2):87–103, 1960. ISSN 0043-1648. doi: https://doi.org/10.1016/0043-1648(60)90055-7. URL `https://www.sciencedirect.com/science/article/pii/0043164860900557`.

[44] Gianandrea Messa and Stefano Malavasi. A cfd-based method for slurry erosion prediction. *Wear*, 398, 03 2018. doi: 10.1016/j.wear.2017.11.025.

[45] Mazdak Parsi, Anchal Jatale, Madhusuden Agrawal, and Partha Sharma. Effect of surface deformation on erosion prediction. *Wear*, 430-431, 04 2019. doi: 10.1016/j.wear.2019.04.019.

[46] Y.I. Oka, H. Ohnogi, T. Hosokawa, and M. Matsumura. The impact angle dependence of erosion damage caused by solid particle impact. *Wear*, 203-204:573–579, 1997. ISSN 0043-1648. doi: https://doi.org/10.1016/S0043-1648(96)07430-3. URL `https:`

//www.sciencedirect.com/science/article/pii/S0043164896074303. 11th International Conference on Wear of Materials.

[47] Amir Mansouri. *A combined CFD-experimental method for developing and erosion equation for both gas-sand and liquid-sand flows*. PhD thesis, University of tulsa, 2016.

[48] A.W. Ruff and L.K. Ives. Measurement of solid particle velocity in erosive wear. *Wear*, 35(1):195–199, 1975. ISSN 0043-1648. doi: https://doi.org/10.1016/0043-1648(75)90154-4. URL `https://www.sciencedirect.com/science/article/pii/0043164875901544`.

[49] B.A. Lindsley and A.R. Marder. The effect of velocity on the solid particle erosion rate of alloys. *Wear*, 225-229:510–516, 1999. ISSN 0043-1648. doi: https://doi.org/10.1016/S0043-1648(99)00085-X. URL `https://www.sciencedirect.com/science/article/pii/S004316489900085X`.

[50] J.B. Zu, I.M. Hutchings, and G.T. Burstein. Design of a slurry erosion test rig. *Wear*, 140(2):331–344, 1990. ISSN 0043-1648. doi: https://doi.org/10.1016/0043-1648(90)90093-P. URL `https://www.sciencedirect.com/science/article/pii/004316489090093P`.

[51] S. Turenne, M. Fiset, and J. Masounave. The effect of sand concentration on the erosion of materials by a slurry jet. *Wear*, 133(1):95–106, 1989. ISSN 0043-1648. doi: https://doi.org/10.1016/0043-1648(89)90116-6. URL `https://www.sciencedirect.com/science/article/pii/0043164889901166`.

[52] Hector McI. Clark. On the impact rate and impact energy of particles in a slurry pot erosion tester. *Wear*, 147(1):165–183, 1991. ISSN 0043-1648. doi: https://doi.org/10.1016/0043-1648(91)90127-G. URL `https://www.sciencedirect.com/science/article/pii/004316489190127G`.

[53] J. Tuzson, J. Lee, and K. Scheibe-Powell. Slurry erosion tests with centrifugal erosion tester. *Wear*, 23(1):84–87, 1984.

[54] Chong Yau Wong, Christopher Solnordal, Lachlan Graham, Gregory Short, and Jie Wu. Slurry erosion of surface imperfections in pipeline systems. *Wear*, 336-337:72–85, 2015. ISSN 0043-1648. doi: https://doi.org/10.1016/j.wear.2015.04.020. URL `https://www.sciencedirect.com/science/article/pii/S0043164815002355`.

[55] J.G.A. Bitter. A study of erosion phenomena part i. *Wear*, 6(1):5–21, 1963. ISSN

0043-1648. doi: https://doi.org/10.1016/0043-1648(63)90003-6. URL `https://www.sciencedirect.com/science/article/pii/0043164863900036`.

[56] Erosion by a stream of solid particles. *Wear*, 11(2):111–122, 1968. doi: 10.1016/0043-1648(68)90591-7.

[57] Cunkui Huang, S. Chiovelli, Peter Minev, Jing-Li Luo, and Krishnaswamy Nandakumar. A comprehensive phenomenological model for erosion of materials in jet flow. *Powder Technology - POWDER TECHNOL*, 187:273–279, 11 2008. doi: 10.1016/j.powtec.2008.03.003.

[58] S.A. Shirazi J. Zhang, B.S. McLaury. Effect of near wall modeling approaches on solid particle erosion prediction. *WEAR 370-371*, pages 36–58, 1979.

[59] M. T. Benchaita, P. Griffith, and E. Rabinowicz. Erosion of Metallic Plate by Solid Particles Entrained in a Liquid Jet. *Journal of Engineering for Industry*, 105(3):215–222, 08 1983.

[60] R. Okita. *Effects of Viscosity and Particle Size on Erosion Measurements and Predictions*. University of Tulsa, 2010. URL `https://books.google.it/books?id=Bg3fYgEACAAJ`.

[61] V.B. Nguyen, Q.B. Nguyen, C.Y.H. Lim, Y.W. Zhang, and B.C. Khoo. Effect of air-borne particle–particle interaction on materials erosion. *Wear*, 322-323:17–31, 2015. ISSN 0043-1648. doi: https://doi.org/10.1016/j.wear.2014.10.014. URL `https://www.sciencedirect.com/science/article/pii/S0043164814003196`.

[62] H.C. Meng and K.C. Ludema. Wear models and predictive equations: their form and content. *Wear*, 181-183:443–457, 1995. ISSN 0043-1648. doi: https://doi.org/10.1016/0043-1648(95)90158-2. URL `https://www.sciencedirect.com/science/article/pii/0043164895901582`. 10th International Conference on Wear of Materials.

[63] Kenichi Sugiyama, Kenji Harada, and Shuji Hattori. Influence of impact angle of solid particles on erosion by slurry jet. *Wear*, 265:713–720, 08 2008. doi: 10.1016/j.wear.2008.01.020.

[64] Amir Mansouri, Hadi Arabnejad, Siamack Shirazi, and Brenton McLaury. A combined cfd/experimental methodology for erosion prediction. *Wear*, pages –, 12 2014. doi: 10.1016/j.wear.2014.11.025.

[65] R. Mei. An approximate expression for the shear lift force on a spherical particle at finite reynolds number. *International Journal of Multiphase Flow*, 18(1):145–147,

1992. ISSN 0301-9322. doi: https://doi.org/10.1016/0301-9322(92)90012-6. URL `https://www.sciencedirect.com/science/article/pii/0301932292900126`.

[66] P. G. Saffman. The lift on a small sphere in a slow shear flow. *Journal of Fluid Mechanics*, 22(2):385–400, 1965. doi: 10.1017/S0022112065000824.

[67] A. Haider and O. Levenspiel. Drag coefficient and terminal velocity of spherical and nonspherical particles. *Powder Technology*, 58(1):63–70, 1989. ISSN 0032-5910. doi: https://doi.org/10.1016/0032-5910(89)80008-7. URL `https://www.sciencedirect.com/science/article/pii/0032591089800087`.

[68] Alister Forder, Martin Thew, and David Harrison. A numerical investigation of solid particle erosion experienced within oilfield control valves. *Wear*, 216(2):184–193, 1998. ISSN 0043-1648. doi: https://doi.org/10.1016/S0043-1648(97)00217-2. URL `https://www.sciencedirect.com/science/article/pii/S0043164897002172`.

[69] Gianandrea Vittorio Messa, Yongbo Wang, Marco Negri, and Stefano Malavasi. An improved cfd/experimental combined methodology for the calibration of empirical erosion models. *Wear*, 476:203734, 2021. ISSN 0043-1648. doi: https://doi.org/10.1016/j.wear.2021.203734. URL `https://www.sciencedirect.com/science/article/pii/S004316482100123X`. 23rd International Conference on Wear of Materials.

[70] Y.I. Oka, K. Okamura, and T. Yoshida. Practical estimation of erosion damage caused by solid particle impact: Part 1: Effects of impact parameters on a predictive equation. *Wear*, 259(1):95–101, 2005. ISSN 0043-1648. doi: https://doi.org/10.1016/j.wear.2005.01.039. URL `https://www.sciencedirect.com/science/article/pii/S0043164805000979`. 15th International Conference on Wear of Materials.

[71] Naser Haghbin, Farbod Ahmadzadeh, Jan K. Spelt, and Marcello Papini. Effect of entrained air in abrasive water jet micro-machining: Reduction of channel width and waviness using slurry entrainment. *Wear*, 344-345:99–109, 2015. ISSN 0043-1648. doi: https://doi.org/10.1016/j.wear.2015.10.008. URL `https://www.sciencedirect.com/science/article/pii/S0043164815004494`.

[72] V.B. Nguyen, Q.B. Nguyen, Z.G. Liu, S. Wan, C.Y.H. Lim, and Y.W. Zhang. A combined numerical–experimental study on the effect of surface evolution on the water–sand multiphase flow characteristics and the material erosion behavior. *Wear*, 319(1):96–109, 2014. ISSN 0043-1648. doi: https://doi.org/10.1016/j.wear.2014.07.017. URL `https://www.sciencedirect.com/science/article/pii/S0043164814002439`.

List of Figures

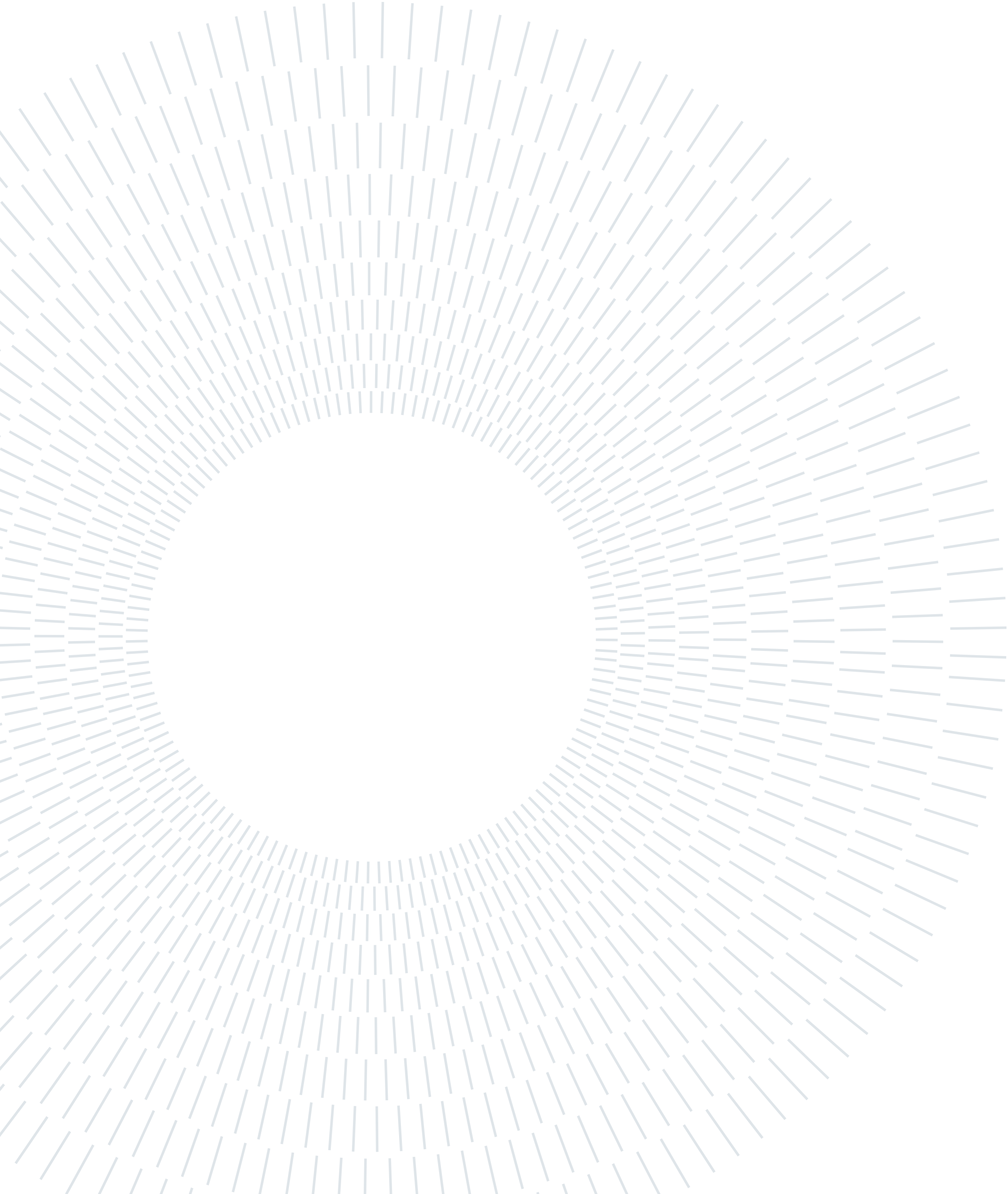

List of Tables

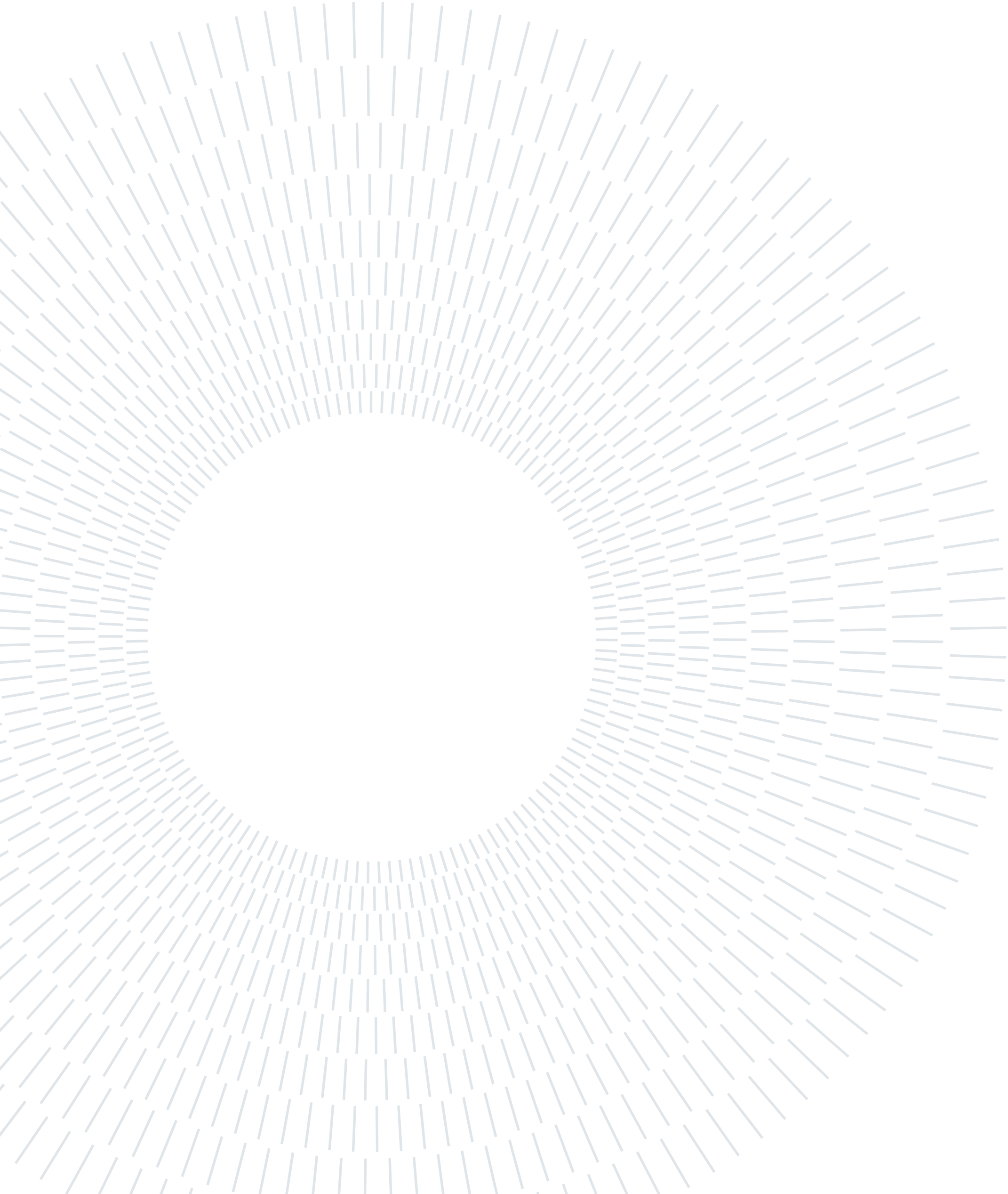

List of Symbols

Variable	Description	SI unit
$\dot{E}_p$	erosion volume rate by single particle impingeent	kg/s
$\dot{m}_p$	local particle mass flow rate	kg/s
$\mathbf{v}_p$	particle impact velocity	m/s
v_p	particle impact velocity magnitude	m/s
$f(\theta)$	impact angle function	-
$g(v)$	impact velocity function	-
BH	Brinnel hardness	MPa
F_s	particle shape factor	-
ER	erosion rate	-
H_v	Vicker's hardness	MPa
St_p	particle's Stokes number	-
τ_p	particle response time	s
τ_f	fluid time scale	s
α_p	particle volume fraction	-
$\mathbf{u}_f$	instantaneous fluid velocity	m/s
p	fluid pressure	Pa
ρ_f	fluid density	kg/m^3
μ	fluid dynamic viscosity	Pa s
$\mathbf{U}_f$	average fluid velocity	m/s
P_f	average fluid pressure	Pa
τ_{Re}	Reynolds stresses tensor	Pa
u'	turbulent velocity flactuation	m/s
m_p	particle's mass	Kg
$\mathbf{v}_p$	particle's velocity	m/s
α_w	water volume fraction	-
α_a	air volume fraction	-
$\mathbf{F}_{st}$	surface tension force	N
σ	surface tension coefficient	N/m^2

Variable	Description	SI unit
F_m	mass force	N
F_{fp}	fluid-to-particle force	N
F_{pp}	particle-particle force	N
F_{drag}	drag force	N
F_{lift}	lift force	N
$F_{buoyancy}$	buoyancy force	N
$F_{pressure}$	pressure force	N
$F_{virtual\,mass}$	virtual mass force	N
ρ_p	particle's density	kg/m^3
$u_{@p}$	unhindered fluid velocity at particle location	m/s
d_p	particle diameter	m
Re_p	particle Reynolds number	-
v^{after}	particle velocity after impact	m/s
v^{before}	particle velocity before impact	m/s
$e_{\mathbf{t}}$	tangential restitution coefficient	-
$e_{\mathbf{n}}$	normal restitution coefficient	-
$\bar{v}_{p,i}$	average particle impact velocity in cell i	m/s
$\bar{\theta}_{p,i}$	average particle impact angle in cell i	deg
ER_i	erosion rate in cell i	-
h_i	mean erosion depth in cell i	m
S_i	surface area of cell i	m^2
ρ_t	target material density	kg/m^3
N_p	number of impacts	-
d	mean particle diameter	m
$\mathbf{V}_{jet}$	jet velocity	m/s
θ_{jet}	jet angle	deg
$\hat{c}$	particle concentration	-
D	nozzle diameter	m
R_i	radius of cell i	m
dR_i	radial increment	m
N_{rings}	number of rings created	-
R	radial distance from sample center	m
n	impact velocity coefficient	-

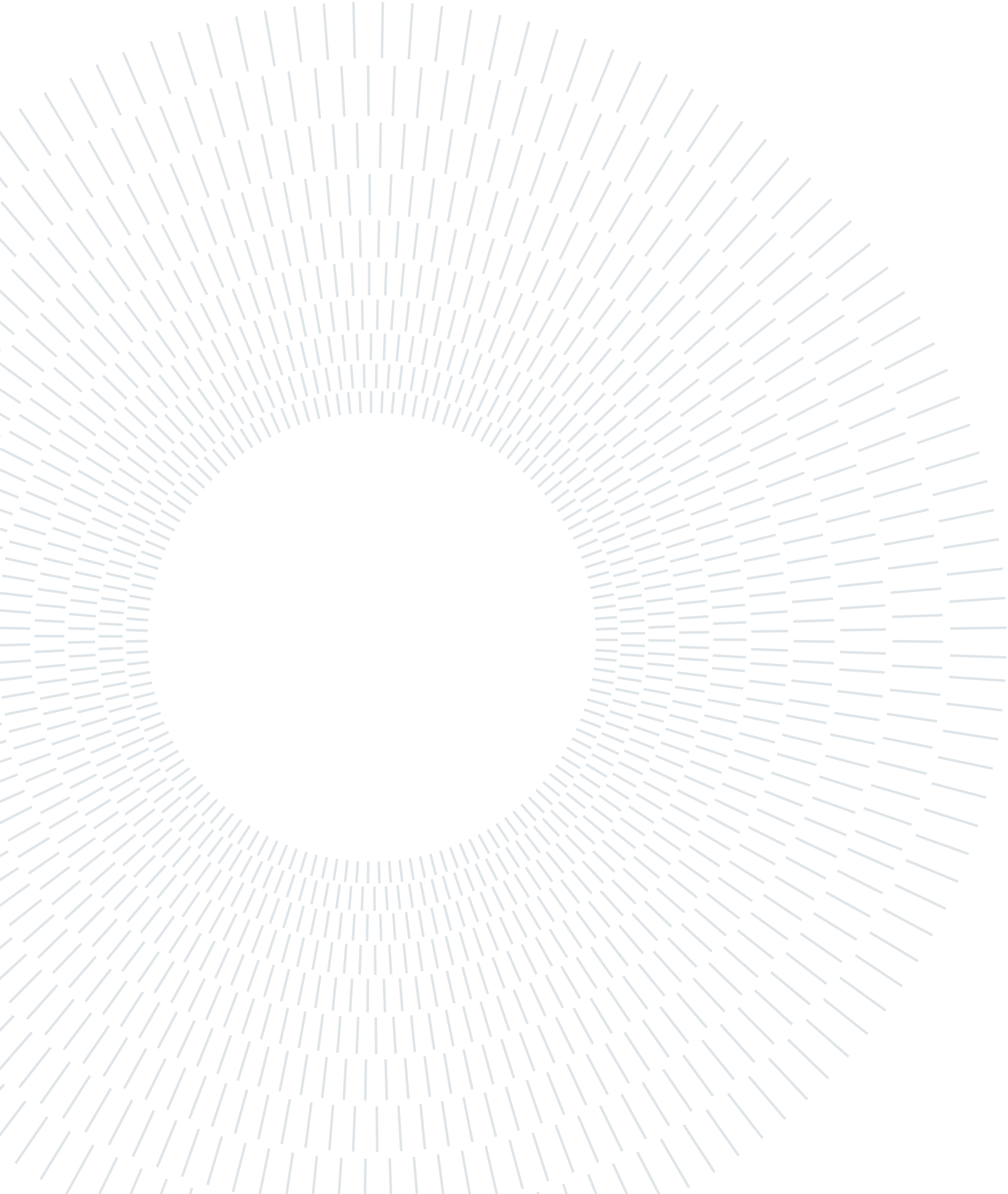

Acknowledgements

The presented work could not have been possible without the theoretical and experimental contribution of professor Gianandrea Vittorio Messa and Yongbo Wang. In addition, a heartfelt mention to professor Marcello Papini, Majid Moghaddam and Mohammad Ali, who performed meticulous experiments and provided useful laboratory data for the continuation of the study.